NOTICE

AVIS

The quality of this microform is heavily dependent upon the quality of the original thesis submitted for microfilming. Every effort has been made to ensure the highest quality of reproduction possible.

La qualité de cette microforme dépend grandement de la qualité de la thèse soumise au microfilmage. Nous avons tout fait pour assurer une qualité supérieure de reproduction.

If pages are missing, contact the university which granted the degree.

S'il manque des pages, veuillez communiquer avec l'université qui a conféré le grade.

Some pages may have indistinct print especially if the original pages were typed with a poor typewriter ribbon or if the university sent us an inferior photocopy.

La qualité d'impression de certaines pages peut laisser à désirer, surtout si les pages originales ont été dactylographiées à l'aide d'un ruban usé ou si l'université nous a fait parvenir une photocopie de qualité inférieure.

Canada

UNIVERSITY OF ALBERTA

MODELING RAPIDLY VARIED OPEN CHANNEL FLOWS

by

ABDUL AZIZ KHAN ⓒ

A thesis

submitted to the Faculty of Graduate Studies and Research

in partial fulfillment of the requirements for the degree of

Doctor of Philosophy

in

WATER RESOURCES ENGINEERING

DEPARTMENT OF CIVIL ENGINEERING

Edmonton, Alberta

Fall, 1995

Your file   Votre référence

Our file   Notre référence

ISBN 0-612-06234-1

Canada

UNIVERSITY OF ALBERTA

Library Release Form

Name of Author: Abdul Aziz Khan

Title of Thesis: Modeling Rapidly Varied Open Channel Flows

Degree: Doctor of Philosophy

Year this Degree Granted: 1995

Permission is hereby granted to the University of Alberta Library to reproduce single copies of this thesis and to lend or sell such copies for private, scholarly, or scientific research purposes only.

The author reserves all other publication and other rights in association with the copyright in the thesis, and except as hereinbefore provided, neither the thesis nor any substantial portion thereof may be printed or otherwise reproduced in any material form whatever without the author's prior written permission.
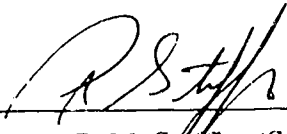
Abdul Aziz Khan

41-A Zaryab Colony

Peshawar City, Peshawar

N-W.F.P., Pakistan.
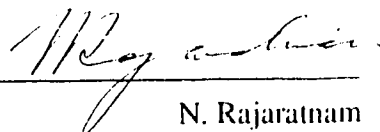
Dated: _June 30, 1995_
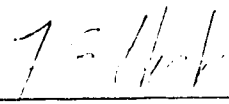
UNIVERSITY OF ALBERTA
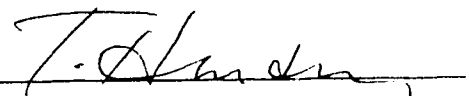
Faculty of Graduate Studies and Research

The undersigned certify that they have read, and recommend to the Faculty of Graduate Studies and Research for acceptance, a thesis entitled MODELING RAPIDLY VARIED OPEN CHANNEL FLOWS submitted by ABDUL AZIZ KHAN in Partial fulfillment of the requirements for the degree of DOCTOR OF PHILOSOPHY in WATER RESOURCES ENGINEERING.
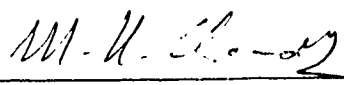
P. M. Steffler (Supervisor)

N. Rajaratnam

F. E. Hicks

T. M. Hrudey

L. W. Sigurdson

M. H. Chaudhry (External Examiner)

Date: June 30, 1995

Abstract

Rapidly varied transitions, such as rapid expansion or contraction of the flow in a vertical or horizontal plane, in open channels typically involve flows with high curvatures and/or slopes. The length of such transitions is usually short, the pressure distributions are significantly non-hydrostatic and the velocity distributions are highly non-uniform. A two-dimensional (in a vertical plane) model or a three-dimensional model would be able to model these situations satisfactorily. However, the computational effort involved in modeling long river reaches and the complexity of the equations are often the limiting factors. On the other hand, one and two-dimensional depth averaged modeling of gradually varied open channel flow, on account of their simplicity and computational ease, are common.

The depth averaged St. Venant equations, which are used for most of the computational models in open channels, assume uniform longitudinal velocity and hydrostatic pressure distributions and are inapplicable for modeling rapidly varied flow phenomena. The Boussinesq equations, which represent a next level of approximation, assume non-hydrostatic linear pressure and vertical velocity distributions and are applicable to moderately shallow flows only.

The vertically averaged and moment (VAM) equations, which assume a linear longitudinal velocity distribution and quadratic pressure and vertical velocity distributions, provide an even higher degree of approximation for depth averaged models and are applicable for a wavelength to depth ratio as small as one. The longitudinal velocity distribution allows for better representation of bed shear stress in non-uniform flow and yields to easy incorporation of turbulent closure models. Thus, these equations are capable of a better representation of flow situations with the

advantages of depth averaged models. Also, these equations can easily be extended to include lateral variations in open channel flows. The VAM equations, because of their advantages are investigated for developing a general purpose open channel flow model.

In this study, the VAM and VA (similar to the Boussinesq equations) equations are solved numerically using a hybrid Petrov-Galerkin and Bubnov-Galerkin finite element scheme, while the modified St. Venant equations are modeled using the Petrov-Galerkin finite element scheme.

As a first test, the VAM equations are applied to three cases of flow over curved beds. Three tests consisting of flow from a horizontal to a steep channel with a circular transition, flow over symmetric and asymmetric bed profiles and flow over an idealized flip-bucket were conducted. The results show that the VAM equations are more suitable, for predicting bed pressure and water surface profiles, for curved beds with large flows and large bed and water surface curvatures than the VA equations.

Next, the VAM equations are used to model flow over free overfalls with smooth and rough beds and sharp crested weirs with sloping upstream faces. The results from the VAM equations compare well with the measured data, both for the upper and lower nappe profiles of the free jet and the upstream surface profiles. Also, the computed longitudinal velocity distributions, and vertical velocity and pressure distributions upstream of the overfall have satisfactory agreement with a potential flow model and measured data respectively. The results for weirs with 4:1 (4 horizontal to 1 vertical) and 2:1 upstream slopes are in good agreement with the measured data, while for 45 degree upstream slope and large weir heights the modeled upstream water surface shows numerical instabilities.

Both the Boussinesq and St. Venant equations are unable to model the surface profile of the hydraulic jump accurately. Using the moment of longitudinal momentum equation and a simplified algebraic stress model, a single new term in the St. Venant

equations is proposed. This new term, called the jump momentum flux, combines the turbulent stress and velocity distribution effects in terms of depth and depth averaged velocity. With an appropriate calibration of a single coefficient, the model gives good results for the location, length and profile of hydraulic jumps ranging in Froude number from 2 to 7. Furthermore, the location and length of the jump are found to be independent of the spatial discretization.

In this study, the VAM equations are successfully modeled for rapidly varied flow phenomena. These equations can further be used for modeling moving surges by incorporating a turbulent closure model. Also, the present one-dimensional equations can further be developed into two-dimensional equations.

Acknowledgements

Table of Contents

List of Figures

List of Symbols

$\mathbf{A}$ =   advection matrix;

A =   turbulence model constant;

a =   turbulence model constant;

b =   turbulence model constant;

c_D =   turbulence model constant;

$\mathbf{F}$ =   Froude number;

F =   total specific force per unit width;

f =   sequent depth ratio;

f_i =   a part of test function;

f_j =   basis functions;

g =   acceleration due to gravity;

h =   depth of flow measured vertically;

h_0 =   depth at the upstream boundary;

h_c =   depth of flow at the critical section;

i, j =   tensor indices;

$\mathbf{J}_e$ =   element Jacobian matrix;

J =   jump momentum flux;

K_1 =   jump flux model constant;

K_2 =   jump flux model constant;

k =   turbulent kinetic energy;

k_s =   bed roughness;

L =   turbulent length scale;

l =   tensor index;

ℓ_m = turbulent mixing length;

$\mathbf{M}$ = eigen vectors in columns;

M = momentum flux integral;

P = pressure force per unit width;

p = pressure;

p_1 = bed pressure in excess of hydrostatic pressure;

p_2 = mid-depth pressure in excess of the average of pressure at the bed and

surface;

$\wp_{ij}$ = turbulence production components;

q = discharge per unit width of the channel;

$\mathbf{R}_l$ = vector of residuals;

r,s = tensor indices;

S = normal force per unit width;

S_0 = bed slope;

S_f = friction slope;

t = time;

U' = depth averaged mean square longitudinal velocity fluctuation;

u = horizontal velocity;

u' = longitudinal velocity fluctuation;

u_0 = vertically averaged horizontal velocity;

u_1 = horizontal surface velocity in excess of the vertical average;

u_c = horizontal velocity at the critical section;

$\mathbf{W}$ = upwinding matrix;

W_{ij} = elements of upwinding matrix;

w = vertical velocity;

$\overline{w}$ = vertically averaged vertical velocity;

w'	=	vertical velocity fluctuation;
w'_2	=	mid-depth vertical velocity in excess of the average of the vertical velocity at the bed and surface;
w_b	=	vertical velocity at the bed;
w_h	=	vertical velocity at the surface;
x	=	horizontal coordinate;
z	=	vertical coordinate;
$\bar{z}$	=	mid-depth elevation;
z_b	=	bed elevation;
α_0	=	mixing length proportionality constant;
β	=	momentum flux correction factor;
γ	=	specific weight of water;
$\delta\Phi$	=	correction to the assumed guesses;
δ_{ij}	=	Kronecker delta;
ε	=	dissipation rate of turbulent kinetic energy;
η	=	non-dimensional vertical coordinate;
θ	=	implicitness;
Λ	=	a matrix of eigen values;
λ_i	=	eigen values;
ρ	=	density;
σ_x	=	Reynolds normal stress in longitudinal direction;
$\bar{\sigma}_x$	=	depth averaged turbulent normal stress in horizontal direction;
σ_z	=	Reynolds normal stress in vertical direction;
$\bar{\sigma}_z$	=	depth averaged turbulent normal stress in vertical direction;
τ_b	=	bed shear stress;
τ_{xz}	=	Reynolds shear stress;

$\overline{\tau}_{xc}$ = depth averaged turbulent shear stress;

Φ = vector of unknown variables at each node;

ω = upwinding parameter;

Chapter 1

Introduction

Rapidly varied transitions, such as rapid expansion or contraction of the flow in a vertical or horizontal plane, in open channels typically involve flows with high curvatures and/or slopes. The length of such transitions are usually short, the pressure distributions are significantly non-hydrostatic and the velocity distributions are highly non-uniform. Also, the bed shear stress may be significantly different from the corresponding uniform flow conditions. These situations can be modeled satisfactorily using a two-dimensional model in a vertical plane, while a three-dimensional model would be required if the lateral variations across the channel are to be considered. However, the computational effort involved in modeling long river reaches and the complexity of the equations are often the limiting factors. On the other hand, one and

1

two-dimensional depth averaged modeling of gradually varied open channel flow, on account of their simplicity and computational ease, are common.

At present most computational models of open channels are based on the depth averaged St. Venant equations. In these equations, uniform longitudinal velocity and hydrostatic pressure distributions are assumed thus limiting their applicability to very shallow flows, with wavelength to depth ratio in excess of about 20 (Henderson, 1966). In order to model the rapidly varied flow phenomena using the advantages of depth averaged equations, assumed velocity and pressure distributions have to be incorporated in these equations. One such attempt is represented by the Boussinesq equations, which assume linear vertical velocity and non-hydrostatic linear pressure distributions. These equations are applicable for moderately shallow flows with wavelength to depth ratio of about six (Steffler and Jin, 1993). For both the above sets of equations, the longitudinal velocity is represented only by its mean value, thus uniform flow bed shear stress has to be used even for the case of highly non-uniform flow. Also, for scour and erosion problems the direction of bed shear may be significantly different from that of the mean flow (Steffler and Jin, 1993).

A further alternative in this area was the introduction of the vertically averaged and moment (VAM) equations by Steffler and Jin (1993). Therein, the plane Reynolds equations were vertically averaged and the moment equations were developed by vertically integrating the Reynolds equations after being multiplied by the vertical coordinate. The three extra equations allowed specification of three further flow parameters. A linear longitudinal velocity distribution and quadratic pressure and vertical velocity distributions were assumed and the equations were rewritten in terms of the parameters of these distributions. The longitudinal velocity distribution, although crude, allows for estimating the bed shear using the near bed velocity rather than the

mean velocity. Also, the above set of equations yields to easy incorporation of the turbulent normal and shear stresses through turbulent closure models.

The VAM equations, although vertically averaged, provide a better representation of the flow by incorporating more vertical details when compared to the St. Venant and Boussinesq equations. Small amplitude wave analysis, Steffler and Jin (1993), showed that these equations are valid up to a wavelength to depth ratio of about one, a considerable improvement when compared to the St. Venant and Boussinesq equations. Also, the present model has a potential for extension to two-dimensional flow in a horizontal plane, wherein the vertical detail incorporated in the model can provide a better representation of the flow with the advantages of two-dimensional depth averaged models (Jin and Steffler, 1993). Because of the above advantages, the VAM equations are investigated for developing a general purpose open channel flow model, which in addition to modeling gradually varied flow should be capable of modeling rapidly varied open channel flows.

Both the Boussinesq and St. Venant equations are traditionally depth averaged. However, the Boussinesq equations, used in this study are derived as a special case of the VAM equations by neglecting the longitudinal velocity distribution and assuming linear pressure and vertical velocity distributions. The resulting equations, although similar to that reported by Gharangik and Chaudhry (1991), are called vertically averaged (VA) equations.

The VAM, VA and St. Venant equations are modeled using a hybrid Petrov-Galerkin and Bubnov-Galerkin finite element scheme. The Characteristic Dissipative Galerkin finite element scheme, a member of Petrov-Galerkin schemes, recently introduced by Hicks and Steffler (1992), is employed for the continuity and longitudinal momentum equations. While the rest of the equations, if applicable, are modeled using the Bubnov-Galerkin finite element scheme.

3

As a first test, the results from the Boussinesq and VAM equations are compared with the measured data for three different cases of flow over curved beds. First, flow from a horizontal to a steep (up to 60 degree) slope with a circular transition is modeled. Second, flow over a symmetric and an asymmetric bed profile is tested. Last, flow over a flip-bucket spillway with a sloping upstream face is modeled. A flip-bucket spillway consists of a steep chute with a circular arc at the end which deflects the incoming flow to a desired angle. The results show that the VAM equations are more suitable, for predicting bed pressure and water surface profiles, for curved beds with large flows and large bed and water surface curvatures.

A rectangular free overfall, which represents a vertical drop in the channel with zero submergence, has been extensively investigated experimentally, numerically and analytically by many researchers. The numerical and analytical solutions are based on potential flow theory and the solution is limited to smooth horizontal beds.

Next, the rectangular free overfall problem is modeled using the VAM equations and at the same time the applicability of the solution is extended to large slopes by modeling flow over sharp crested weirs with sloping upstream faces and rough beds. For modeling the free jet downstream of an overfall or a weir, the VAM equations are modified and two types of elements are specified. A zero bed pressure is specified for the free jet elements and the lower surface profile is obtained, while for the second type of elements the bed profile is given and bed pressures are evaluated. At the junction of two types of elements, internal boundary conditions of zero bed pressure and a fixed bed elevation are specified. The results from the VAM equations compare well with the measured data, both for the upper and lower nappe profiles of the free jet and the upstream surface profiles. Also, the computed results of the vertical velocity and pressure distributions upstream of the overfall agree well with the measured data; while the computed longitudinal velocity distributions match

4

satisfactorily with the two-dimensional potential flow model developed by Montes (1992). The results for weirs with 4:1 (4 horizontal to 1 vertical) and 2:1 upstream slopes are in good agreement with the measured data, while for 45 degree upstream slope and large weir heights the modeled water surface upstream of a weir shows numerical instabilities.

The hydraulic jump, which represents a transitional state between an upstream supercritical flow and a downstream subcritical flow, has a fixed length and location for a given flow condition. Both the Boussinesq and St. Venant equations have been numerically modeled to simulate the hydraulic jump. However, the dissipative shock capturing schemes, adapted from the gas dynamics methods, for modeling these equations emphasize mainly on suppressing the oscillations before and after the jump and maintaining momentum balance across the jump (Abbott et al., 1969). The jump location is well predicted, but the length of the jump is a function of the spatial discretization. The main limitation of the above sets of equations is the uniform longitudinal velocity which cannot generate the turbulent stresses and total momentum flux to spread the jump over its observed length.

A consideration of momentum conservation within a hydraulic jump leads to the conclusion that both the momentum correction due to the non-uniform longitudinal velocity profile and the depth averaged turbulent normal stress are important mechanisms. Using the moment of longitudinal momentum equation and a simplified algebraic stress model, a single new term in the St. Venant momentum equation is proposed. This new term, called the jump momentum flux, combines the turbulent stress and velocity distribution effects in terms of depth and depth averaged velocity. With an appropriate calibration of a single coefficient, the model gives good results for the location, length and profile of hydraulic jumps ranging in Froude numbers from 2.3 to 7.0, independent of the spatial discretization.

5

The three tests mentioned above are presented respectively in chapters two, three and four, while the major conclusions and recommendation for future work follow in chapter five. The details of the numerical scheme applied are provided in appendix A.

References

Abbott, M. B., Marshall, G., and Rodenhius, G. S. (1969). "Amplitude-Dissipative and Phase-Dissipative Scheme for Hydraulic Jump Simulation." 13th Congress IAHR, Tokyo, Japan, Vol. 1, 313-329.

Gharangik, A. M., and Chaudhry, M. H. (1991). "Numerical Simulation of Hydraulic Jump." J. Hydr. Engrg., ASCE, 117(9), 1195-1211.

Henderson, F. (1966). "Open Channel Flow." Macmillan, New York, New York.

Hicks, F. E., and Steffler, P. M. (1992). "Characteristic Dissipative Galerkin Scheme for Open-Channel Flow." J. Hydr. Engrg., ASCE, 118(2), 337-352.

Jin, Y., and Steffler, P. M. (1993). "Predicting Flow in Curved Open Channels by Depth-Averaged Method." J. Hydr. Engrg., ASCE, 119(1), 109-124.

Steffler, P. M., and Jin, Y. (1993). "Depth Averaged and Moment Equations for Moderately Shallow Free Surface Flow." Journal of Hydraulic Research, IAHR, Vol. 31, No. 1, 5-17.

Montes, J. S. (1992). "A Potential Flow Solution for the Free Overfall." Proceedings Institution of Civil Engineers, Water, Maritime and Energy, 96, 259-266.

Chapter 2

Vertically Averaged and Moment Equations Model for Flow Over Curved Beds *

2.1 Introduction

Rapidly varied transitions in open channels typically involve flows with high curvatures and/or slopes. The length of such transitions is usually short, the pressure distributions are significantly non-hydrostatic and the velocity distributions are highly non-uniform. While two-dimensional free surface (usually potential flow, e.g. Montes, 1994) models are feasible, hydraulic engineering practice relies primarily on physical model studies for flow analysis of these situations. On the other hand, one-dimensional modeling of gradually varied open channel flow is common. The purpose

of this paper is to present the results of an effort to extend the applicability of one-dimensional modeling to rapidly varied flow problems.

At present, most computational modeling of open channel flows are based on the depth averaged St. Venant equations. In these equations, uniform longitudinal velocity and hydrostatic pressure distributions are assumed. Correction coefficients may be applied for different distributions if they can be established a-priori (Yen, 1973). These equations are applicable for very shallow flows, with wavelength to depth ratios in excess of about 20 (Henderson, 1966). For moderately shallow flows (i.e. for shorter feature wavelengths), the Boussinesq equations are the next level of approximation (Chaudhry, 1993). While the Boussinesq equations are applicable to somewhat shorter lengths (about six depths) they do not appear to have been successfully applied to problems with steep slopes (Montes, 1994).

Dressler (1978) attempted to extend the one-dimensional approach to higher curvature flows by using a curvilinear, orthogonal coordinate system based on the bed geometry. This approach, applied by Sivakumaran et al. (1983), is based on a potential flow assumption. The method, however, does not account for the water surface curvature being different from the bed curvature and reduces to the St. Venant equations for a flat bed.

Hager and Hutter (1984) presented a method, based on a potential flow in a streamline coordinate system, which assumes a linear variation of flow angle and curvature between the bed and surface. The result was shown to be an improvement over the Boussinesq equations but is limited to geometrically mild slopes. Hager (1985) extended this method to moderate slopes (up to about 30 degree). A similar, but higher order method, was developed by Matthew (1991) in a Cartesian coordinate system. This method involves an iterative solution. Corrections for the effects of friction were also incorporated.

9

A further alternative was presented by Steffler and Jin (1993). Therein, the plane Reynolds equations were vertically averaged and moment equations were developed by vertically integrating the Reynolds equations after they had been multiplied by the vertical coordinate. The three extra equations allow specification of three further flow parameters. A linear longitudinal velocity distribution and quadratic pressure and vertical velocity distributions were assumed and the equations were rewritten in terms of the parameters of these distributions. Essentially, the approach amounts to a low order weighted residual method. The method suffers from the crudeness and arbitrariness of the assumed distributions and results in some long and complex equations where the terms are not of uniform order. It does have the advantage of incorporating the effect of turbulent stresses directly, although these are not important in the applications considered in this paper. More importantly for the present purpose, there is no geometric limitation on slope until the flow is almost vertical, where the assumed vertical distributions become meaningless.

In this paper, these vertically averaged and moment equations are used for simulating flow over curved beds. A Petrov-Galerkin finite element scheme is developed and applied to three test cases. First, flow from a horizontal to a steep (up to 60 degree) slope with a circular arc transition is modeled. Second, flow over a symmetric and an asymmetric bed profile is tested. Last, flow over a flip-bucket spillway with a sloping upstream face is attempted. The ultimate objective is to develop a general one-dimensional model which naturally incorporates rapidly varied flow transitions.

2.2 Equations Modeled

The vertically averaged and moment equations (Steffler and Jin, 1993) consist of three vertically averaged and three moment equations derived from the two-dimensional (vertical - longitudinal, Fig. 2.1) Reynolds equations. The vertically averaged continuity, longitudinal momentum, and vertical momentum equations are as follows:

$$\frac{\partial h}{\partial t} + \frac{\partial q}{\partial x} = 0 \quad ....(2.1)$$

$$\frac{\partial q}{\partial t} + \frac{\partial}{\partial x}\left(\frac{q^2}{h}\right) + \frac{1}{2}\frac{\partial g h^2}{\partial x} + \frac{1}{3}\frac{\partial h u_1^2}{\partial x} + \frac{1}{2\rho}\frac{\partial h p_1}{\partial x}$$

$$+ \frac{2}{3\rho}\frac{\partial h p_2}{\partial x} - \frac{1}{\rho}\frac{\partial h \overline{\sigma}_x}{\partial x} + g h \frac{\partial z_b}{\partial x} + \frac{p_1}{\rho}\frac{\partial z_b}{\partial x} + \frac{\tau_b}{\rho} = 0 \quad ....(2.2)$$

$$\frac{\partial h \overline{w}}{\partial t} + \frac{\partial q \overline{w}}{\partial x} - \frac{1}{6}\frac{\partial}{\partial x}\left[h u_1\left(w_b - w_h\right)\right] - \frac{1}{\rho}\frac{\partial h \overline{\tau}_{zx}}{\partial x} + \frac{\tau_b}{\rho}\frac{\partial z_b}{\partial x} - \frac{p_1}{\rho} = 0 \quad ....(2.3)$$

where x is the longitudinal (horizontal) coordinate, z is the vertical coordinate, t is time, h is the depth of flow measured vertically from the bed, $q(= h u_0)$ is the discharge per unit width, z_b is the bed elevation, g is the gravitational acceleration, and ρ is the fluid density. The other symbols appearing in the above equations are explained below.

The assumed horizontal velocity distribution, shown in Fig. 2.2, is given by

$$u \approx u_0 + u_1(2\eta - 1) \quad ....(2.4)$$

11

where u_0 is the vertically averaged velocity, u_1 is the velocity at the surface in excess of the mean and η is a non-dimensional vertical coordinate defined by

$$\eta = \frac{z - z_b}{h} \quad\text{...(2.5)}$$

The vertical velocity distribution, shown in Fig. 2.3, is given by

$$w \approx w_b(1 - \eta) + w_2 4\eta(1 - \eta) + w_h\eta \quad\text{...(2.6)}$$

where w_b and w_h are the vertical velocities at the bed and surface respectively, and w_2 is the mid-depth vertical velocity in excess of the average of the vertical velocities at the surface and bed. The vertical velocities at the bed and surface are given by bed and surface kinematic conditions as follows

$$w_b = \left(\frac{q}{h} - u_1\right)\frac{\partial z_b}{\partial x} \quad\text{...(2.7)}$$

$$w_h = \frac{\partial h}{\partial t} + \left(\frac{q}{h} + u_1\right)\frac{\partial(z_b + h)}{\partial x} \quad\text{...(2.8)}$$

From (2.6), the mean vertical velocity is

$$\overline{w} = \frac{w_b}{2} + \frac{2}{3}w_2 + \frac{w_h}{2} \quad\text{..(2.9)}$$

and the mean square vertical velocity (needed in a subsequent equation) is

$$\overline{w^2} = \overline{w}^2 + \frac{w_b^2}{12} + \frac{w_h^2}{12} - \frac{w_b w_h}{6} + \frac{1}{20}(2\overline{w} - w_b - w_h)^2 \quad\text{...(2.10)}$$

12

The pressure distribution, shown in Fig. 2.4, is assumed to be quadratic and is given by

$$p \approx (\rho g h + p_1)(1 - \eta) + p_2 4 \eta (1 - \eta) \dots\dots\dots\dots\dots\dots\dots\dots\dots\dots\dots\dots\dots\dots\dots(2.11)$$

where p_1 is the bed pressure in excess of hydrostatic, and p_2 is the mid-depth pressure in excess of the average of the pressure at the bed and surface. The bed stress, τ_b, is modeled with Chezy's equation as

$$\frac{\tau_b}{\rho} = \frac{\left(u_0^2 + \overline{w}^2 \right)}{C_*^2} \dots\dots\dots\dots\dots\dots\dots\dots\dots\dots\dots\dots\dots\dots\dots\dots\dots\dots\dots\dots(2.12)$$

where C_* is the non-dimensional Chezy conveyance coefficient, calculated from Manning's equation or an appropriate log law. The average vertical velocity may be important in this equation for steep slopes. The potential exists in this model to use near bed velocities, rather than mean velocities. However, for the cases considered herein, the bed stress term was mostly of secondary importance only and the above model was adequate. The vertically averaged turbulent normal and shear stresses are represented by $\overline{\sigma_x}$, and $\overline{\tau_{zx}}$, respectively. For the present examples, all involving accelerating flows, these terms are neglected entirely. A turbulence closure model would be required in cases where they were significant.

Three further equations are required to close the above system. Basically, the additional equations are models for u_1, w_2, and p_2. Setting these variables to zero results in a set of equations similar to the Boussinesq equations (Gharangik and Chaudhry, 1991). These equations will be referred to hereafter as the "VA" (Vertically Averaged) equations. Further, setting p_1 to zero and ignoring (2.3) leaves two equations analogous to the St. Venant equations. The difference is that the present equations are vertically averaged (despite the title of the Steffler and Jin, 1993 paper)

13

where the St. Venant and Boussinesq equations are traditionally depth averaged. For flat slopes, the respective equation sets become equivalent.

Following Steffler and Jin (1993), three moment equations are used to compute the three additional distribution parameters u_1, w_2, and p_2. These equations are derived by vertically averaging the same three Reynolds equations after multiplying through by the vertical coordinate z. After some manipulation (including subtracting the mean elevation times the vertically averaged equations), the resulting equations can be written as

$$\frac{1}{4}\frac{\partial h^2}{\partial t} + q\frac{\partial \bar{z}}{\partial x} + \frac{1}{6}\frac{\partial h^2 u_1}{\partial x} - h\overline{w} = 0 \dots\dots\dots\dots\dots(2.13)$$

$$\frac{\partial u_1}{\partial t} + \frac{\partial}{\partial x}\left(\frac{qu_1}{h}\right) - \frac{1}{2\rho}\left(\frac{\partial p_1}{\partial x} - \frac{p_1}{h}\frac{\partial h}{\partial x}\right) + \frac{4p_2}{h\rho}\frac{\partial \bar{z}}{\partial x} - \frac{6}{h\rho}\left(\frac{\tau_b}{2} + \overline{\sigma}_x\frac{\partial \bar{z}}{\partial x} - \overline{\tau}_{xz}\right) = 0 \dots\dots(2.14)$$

$$\frac{\overline{w}}{4}\frac{\partial h^2}{\partial t} - \frac{\partial}{\partial t}\left[\frac{h^2}{12}(w_b - w_h)\right] + \left[q\overline{w} - \frac{hu_1}{6}(w_b - w_h)\right]\frac{\partial \bar{z}}{\partial x} - \frac{\partial}{\partial x}\left[\frac{hq}{12}(w_b - w_h)\right]$$

$$+ \frac{\partial}{\partial x}\left[\frac{h^2 u_1}{10}\left(\overline{w} + \frac{w_b}{3} + \frac{w_h}{3}\right)\right] - h\overline{w^2} - \frac{h}{\rho}\left(\overline{\tau}_{xz}\frac{\partial \bar{z}}{\partial x} - \overline{\sigma}_z\right) - \frac{h\tau_b}{2\rho}\frac{\partial z_b}{\partial x} - \frac{2}{3\rho}hp_2 = 0 \dots(2.15)$$

where

$$\bar{z} = z_b + \frac{h}{2} \dots\dots\dots\dots\dots\dots\dots\dots\dots\dots\dots\dots\dots\dots\dots\dots\dots(2.16)$$

is the mean elevation of a vertical section. For convenience, the full set of equations including (2.13) - (2.15) will be referred to as the VAM (Vertically Averaged and Moment) equations in the following sections.

2.3 Numerical Model

Substituting (2.9), (2.10), (2.12), and (2.16) into (2.1)-(2.3), (2.7), (2.8), and (2.13)-(2.15) leaves a coupled system of eight first order equations with eight unknowns (h, q, u_1, w_b, w_h, $\overline{w}$, p_1, and p_2). While these equations could be further reduced, this expanded form was found to be convenient and is used in the numerical model.

The equations are discretized and solved using the Characteristic Dissipative Galerkin (CDG-1D) finite element scheme of Hicks and Steffler (1992). This scheme provides selective artificial dissipation necessary for shock capturing. For both sets of equations, the upwinding parameter is set to 0.25 and only continuity and longitudinal momentum equations are upwinded. In all cases, to minimize numerical error as much as possible, the spatial discretization was reduced until no change was observed in the solution. Generally, the final element length is an order of magnitude less than the depth of flow.

As the main aim of the study is to explore the applicability of the VAM equations for flow over curved beds, the CDG-1D finite element scheme is employed for illustration purposes. However, these equations can be modeled using any conservative numerical scheme.

The VAM equations, in comparison to the VA equations, have three extra flow parameters to be evaluated at every node and the computational time for these equations should be higher. A steady state test conducted for finding the computational efficiency showed that the VAM equations took about 30 percent more time, to converge to the final steady state solution, as compared to the VA equations. However, in terms of programming effort both sets of equations were found to be similar.

The problems considered, although steady, are solved as unsteady until the asymptotic final solution is reached. An initial condition of constant depth and discharge and all other variables equal to zero is arbitrarily specified. To accelerate convergence, a fully implicit finite difference time stepping scheme is used. Preliminary tests indicated that stable, unique final solutions could be obtained for Courant numbers up to about 6, which is used in the test runs conducted in this study.

For the resulting implicit set of non-linear algebraic equations, a Newton-Raphson iterative solver, with an analytical Jacobian, is used to advance the solution to the next time level. The convergence of the solution to a new time level is assessed by the following convergence criteria

$$\sqrt{\frac{\Sigma(\delta\Phi)^2}{\Sigma\Phi^2}} \leq \text{ 'tolerance'} \dots\dots\dots\dots\dots\dots\dots\dots\dots\dots\dots\dots\dots\dots\dots\dots\dots\dots\dots\dots(2.17)$$

where Φ is the vector of unknowns (length = 8 times the number of nodes), $\delta\Phi$ is the vector of differences between the Φ vectors at two successive iterations. The convergence to final steady state solution is also assessed using (2.17), with $\delta\Phi$ being the difference between the Φ vectors at two successive time levels. In this study, for both convergence criteria, a tolerance of 10^{-6} is used.

2.4 Transition from Horizontal to Steep Slopes

The experimental data for water surface and bed pressure profiles are obtained from the plots provided by Montes (1994). These experiments were performed in a smooth channel of 0.402 m width. Two steep slopes of 45 and 60 degree were studied. For both slopes, the transition from a horizontal to a steep slope was obtained through a circular arc of 0.1 m radius.

The model boundary conditions used for this case, with critical flow occurring at the upstream boundary, are a specified upstream depth (h_0) and vanishing derivatives of the extra pressure and velocity variables $\left(\dfrac{\partial u_1}{\partial x} = \dfrac{\partial p_1}{\partial x} = \dfrac{\partial p_2}{\partial x} = 0 \right)$. As the downstream flow is supercritical, no conditions are applied at the downstream end. For this case the bed shear stress term is neglected.

Figs. 2.5 and 2.6 show the computed and measured water surface and bed pressure profiles respectively, for different discharges, for the 45 degree slope transition. The VAM equations model both the water surface and bed pressure profiles extremely well. The VA equations predict a slightly lower water surface elevation and higher minimum bed pressure in the transition region. For the 60 degree slope transition, the water surface and bed pressure profiles are shown in Figs. 2.7 and 2.8. The behavior of the VA equations is similar to the 45 degree slope case. The VAM equations predict the water surface profiles accurately, and while the bed pressure prediction follows the measured values closely, the minimum pressure is overestimated slightly. The agreement appears to improve with increasing discharge. The overall quality of the solutions compare reasonably well with the two-dimensional potential flow solution presented in the same paper.

2.5 Symmetric and Asymmetric Bed Profiles

The experimental data, consisting of depths and bed pressures, for flow over symmetric and asymmetric bed profiles is obtained from Sivakumaran et al. (1983). These experiments were performed in a horizontal flume 915 cm long, 65 cm high and 30 cm wide. Two bed profiles, symmetric and asymmetric as shown in Figs. 2.9 and 2.11, were tested. The leading edge of the profile in each case was placed 366 cm downstream of the inlet box i.e. head tank. The upstream undisturbed depth was

measured at 16 cm from the leading edge of the profile, and is used as an upstream boundary condition for the models. The symmetric profile was shaped according to a normal distribution and was 20 cm high and 120 cm long. The asymmetric profile, with 150 cm length, was achieved by passing a B-spline through a fixed set of coordinates. Further details of the experimental system and bed profiles can be found in the reference cited above.

The results of both sets of model along with the experimental data for the symmetric shape are shown in Figs. 2.9 and 2.10. For the low flow, the water surface elevation and bed pressure predictions for both the VA and VAM models are almost identical. The predicted water surface elevation matches well with the measured data in the supercritical region, while the results in the subcritical region, although acceptable, may be affected by the boundary conditions adopted for the two models. The modeled bed pressures compare well with the measured data in the subcritical region, while in the supercritical region the measured data show some scatter that may be due to local curvature error and resulting turbulence as discussed by Sivakumaran et al. (1983). For the high flow, the VA equations start to deviate from the results of both the VAM equations and the measured data for surface elevation and bed pressure. For the supercritical region, the VA equations predict a higher surface elevation and bed pressure, while oscillations are predicted for both surface elevation and bed pressure just upstream of the crest. The VAM equations perform well in both subcritical and supercritical regions.

The results for the asymmetric dune shape are shown in Figs. 2.11 and 2.12. For the asymmetric shape, the VA equations underpredict both the depth and pressure in a region of steep slope and large bed and water surface curvatures. The solution deteriorates further for the higher flow. The full equation model performs satisfactorily for the asymmetric dune shape in the entire region. A small blip is noticeable just at the

crest, however. As before, the bed pressures show scatter in the supercritical flow region.

2.6 Flip-Bucket Spillway

An idealized model flip-bucket spillway was constructed and tested to investigate the behavior of the model for an hydraulic system consisting of several components. The spillway crest is similar to the preceding comparisons but the chute and flip-bucket present new requirements. A model capable of treating the entire system at once could be useful in practical design work.

The experimental set-up is shown in Fig. 2.13. The upstream face of the dam was set at an angle of 70 degree, while the spillway chute was set at 20 degree with the horizontal. The two slopes were connected with a circular arc of radius 16.2 cm. The chute was 182.9 cm long. The flip-bucket was also a circular arc of radius 15.4 cm with a 45 degree lip angle. The floor and walls of the chute were made of Plexiglas and the circular arcs were constructed from PVC pipe segments. The flip-bucket spillway was placed inside a 671 cm long, 46.4 cm wide and 90.5 cm high, channel with a head tank. The water was supplied to the head tank from a sump through a 12.7 cm diameter pipe. The pipe was equipped with a valve for controlling the discharge and a magnetic flow meter for measuring the discharge. Although the flow rates considered in this test were small, the radius of the spillway crest and flow depths involved were such that the surface tension and viscosity effects, according to the criteria given by Rao (1975), were negligible.

The water surface elevation was measured by a manual gauge with an accuracy of 0.1 mm. The bed pressures were measured by means of 3 mm taps drilled through

the spillway floor. The base readings for the taps, in each experiment, were obtained immediately after the flow was shut off.

For this test the bed friction term is included, assuming a smooth boundary resistance law. The upstream boundary, for modeling purposes, is fixed at 10.1 cm upstream of the start of the spillway. The boundary conditions are the same as in the preceding cases, except that the bed pressure at the end of the flip-bucket is set to zero.

The predicted and experimental results for the flip-bucket spillway are shown in Figs. 2.14 and 2.15. For the relatively low discharges measured, the surface elevation and bed pressures predictions of both the VA and VAM models for surface elevation and bed pressures agree well with the measurements. As in the previous tests, the VA equations show some wobble near the crest at the higher discharge. In the flip-bucket, both the rising and falling parts of the bed pressures are modeled accurately by both methods.

2.7 Conclusions

Vertically averaged and moment equations models are tested for flow from a horizontal to a steep slope and flow over symmetric and asymmetric bed profiles and a flip-bucket spillway with encouraging success. Comparisons of the results with the measured water surface and bed pressure profiles indicate that, the VAM equations are more suitable for curved beds with large flows and large bed and water surface curvatures. The satisfactory performance of the VAM equations in these cases may be attributed to a higher degree of vertical detail incorporated in the model. While the present study does not give much insight into the mechanisms embodied in the vertically averaged and moment equations, it does indicate that they may be useful in open channel flow modeling.

For the symmetric and asymmetric bed profiles, the results of the VAM equations compare well with the method applied by Sivakumaran et al. (1983). Since the latter method is applicable only for the product of depth and bed curvature in the range of -2 to 0.54, the bed pressures could not be predicted for certain regions of the domain. For the VAM equations no such limitation is encountered and a solution for the bed pressure throughout the whole domain could be obtained. For the transition from a horizontal to a steep slope, the computed results agree well with the two-dimensional potential flow model of Montes (1992). The advantage of the present model is its potential for extension to two-dimensional flow in horizontal plane, wherein the vertical detail incorporated in the model can provide a better representation of the flow with the advantages of two-dimensional depth averaged models. Also, in spite of the fact that for the VAM equations three extra parameters have to be evaluated at each node, the time required for convergence to a final steady state solution was found to be only 30 percent higher than the VA equations.

References

Chaudhry, M.H. (1993). "Open Channel Flow." Prentice-Hall, Englewood Cliffs, New Jersey.

Dressler, R. F. (1978). "New Nonlinear Shallow-Flow Equations with Curvature." Journal of Hydraulic Research, IAHR, Vol. 16, No. 3, 205-220.

Gharangik, A. M., and Chaudhry, M. H. (1991). "Numerical Simulation of Hydraulic Jump." J. Hydr. Engrg., ASCE, 117(9), 1195-1211.

Hager, W.H. and Hutter, K. (1984). "Approximate Treatment of Plane Channel Flow." Acta Mechanica, Vol. 51, 31-48.

Hager, W.H., (1985). "Equations for Moderately Curved Open Channel Flows". J. Hydr. Engrg., ASCE, 111(3), 541-546.

Henderson, F. (1966). "Open Channel Flow." Macmillan, New York.

Hicks, F. E., and Steffler, P. M. (1992). "Characteristic Dissipative Galerkin Scheme for Open-Channel Flow." J. Hydr. Engrg., ASCE, 118(2), 337-352.

Matthew, G. D. (1991). "Higher Order One-Dimensional Equations of Potential Flow in Open Channels." Proc. Instn. Civ. Engrs., Part 2, Vol. 91, June, 187-201.

Montes, J. S. (1994). "Potential-Flow Solution to 2D Transition from Mild to Steep Slope." J. Hydr. Engrg., ASCE, 1(5), 601-621.

Rao, N. S. L. (1975). "Theory of Weirs." Advances in Hydroscience, Vol. 10, Academic Press, New York.

Sivakumaran, N. S., Tingsanchali, T., and Hosking, R. J. (1983). "Steady Shallow Flow Over Curved Beds." J. Fluid Mech., Vol. 128, March, 469-487.

Steffler, P. M., and Jin, Y. (1993). "Depth Averaged and Moment Equations for Moderately Shallow Free Surface Flow." Journal of Hydraulic Research, IAHR, Vol. 31, No. 1, 5-17.

Yen, B.C. (1973). "Open Channel Flow Equations Revisited" J. Eng. Mech. Div.,
ASCE, Vol. 99, No. EM5, 979-1009.
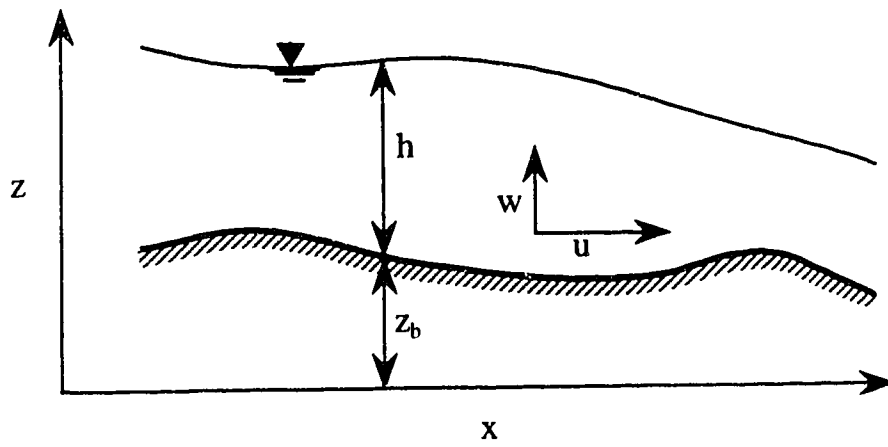
FIG. 2.1. Definition Sketch
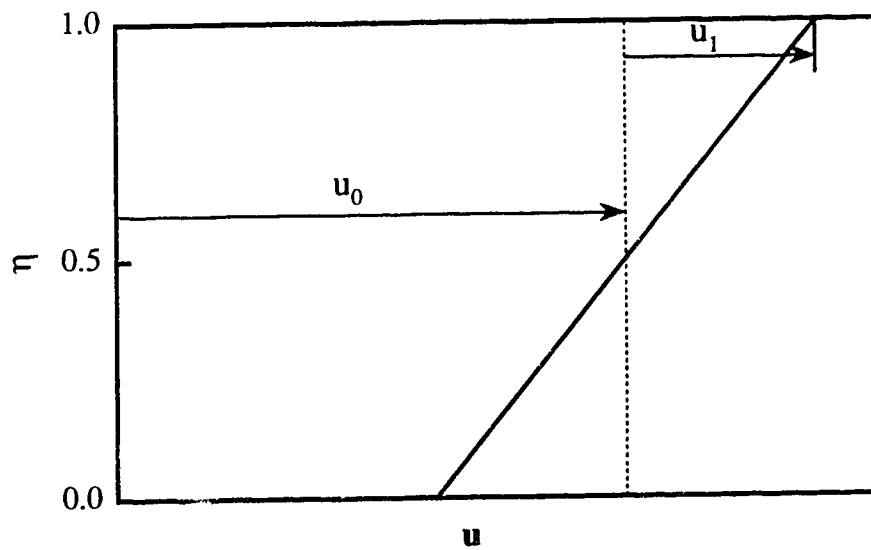
FIG. 2.2. Horizontal Velocity Distribution
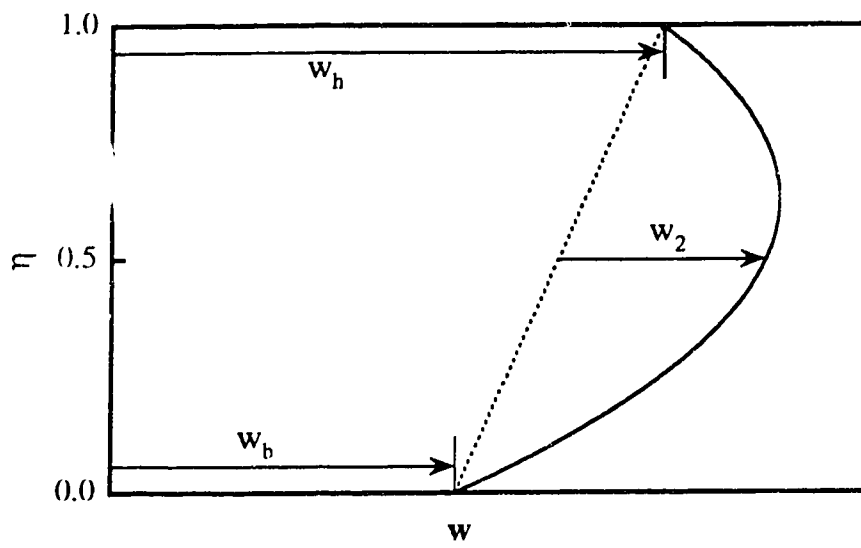
FIG. 2.3. Vertical Velocity Distribution
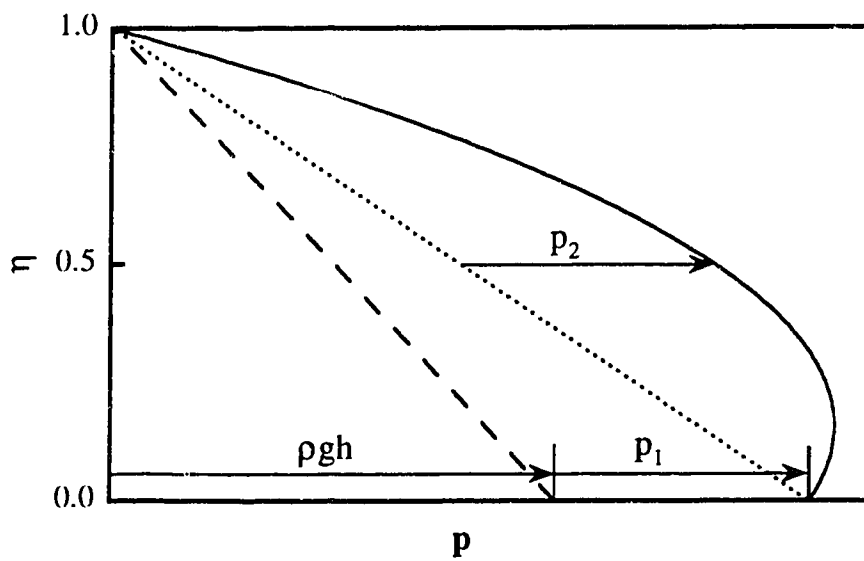
FIG. 2.4. Pressure Distribution
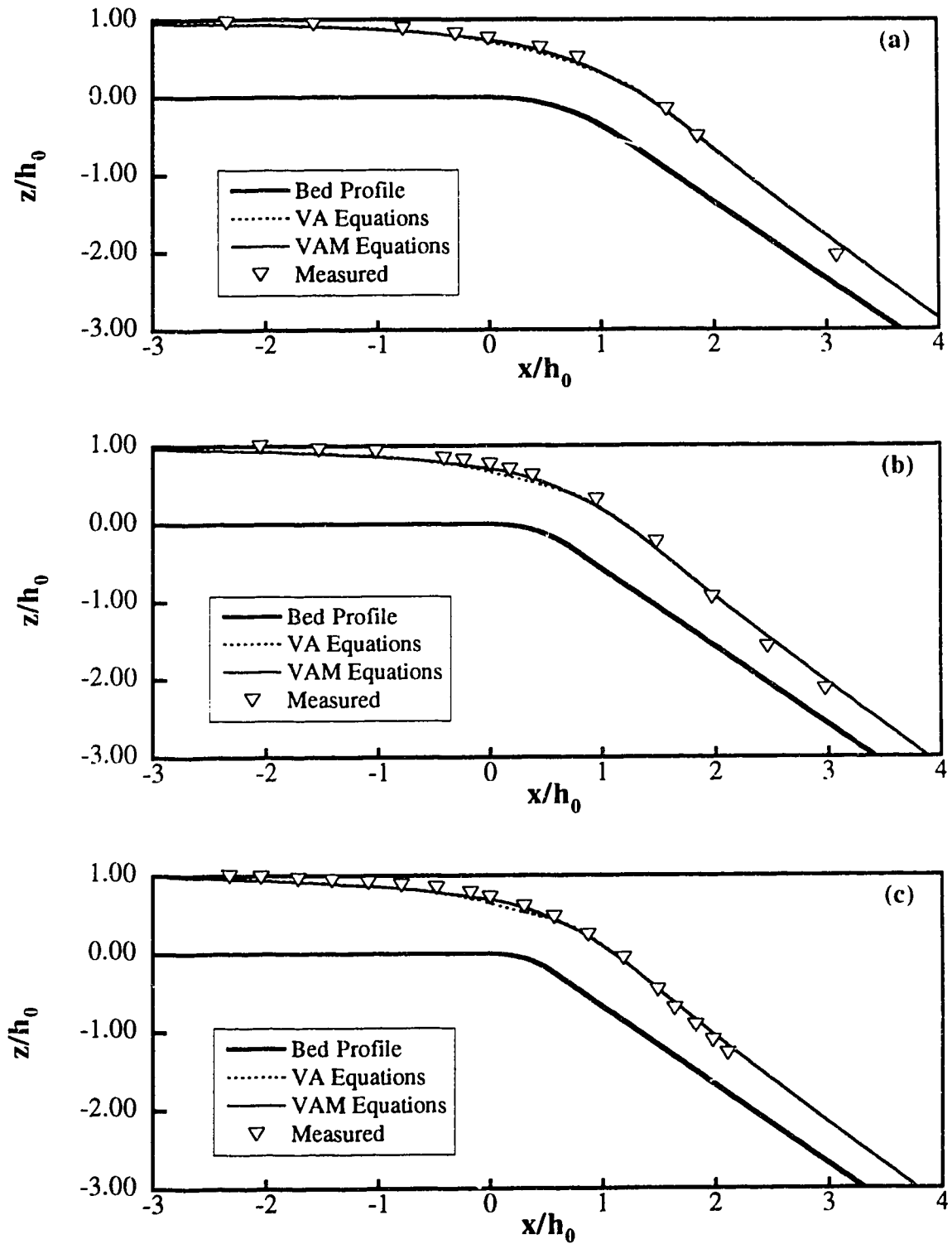
FIG. 2.5. Water Surface Profiles for Transition to 45 Degrees Slope:
(a) Q = 0.02 m³/s; (b) Q = 0.04 m³/s; and (c) Q = 0.06 m³/s
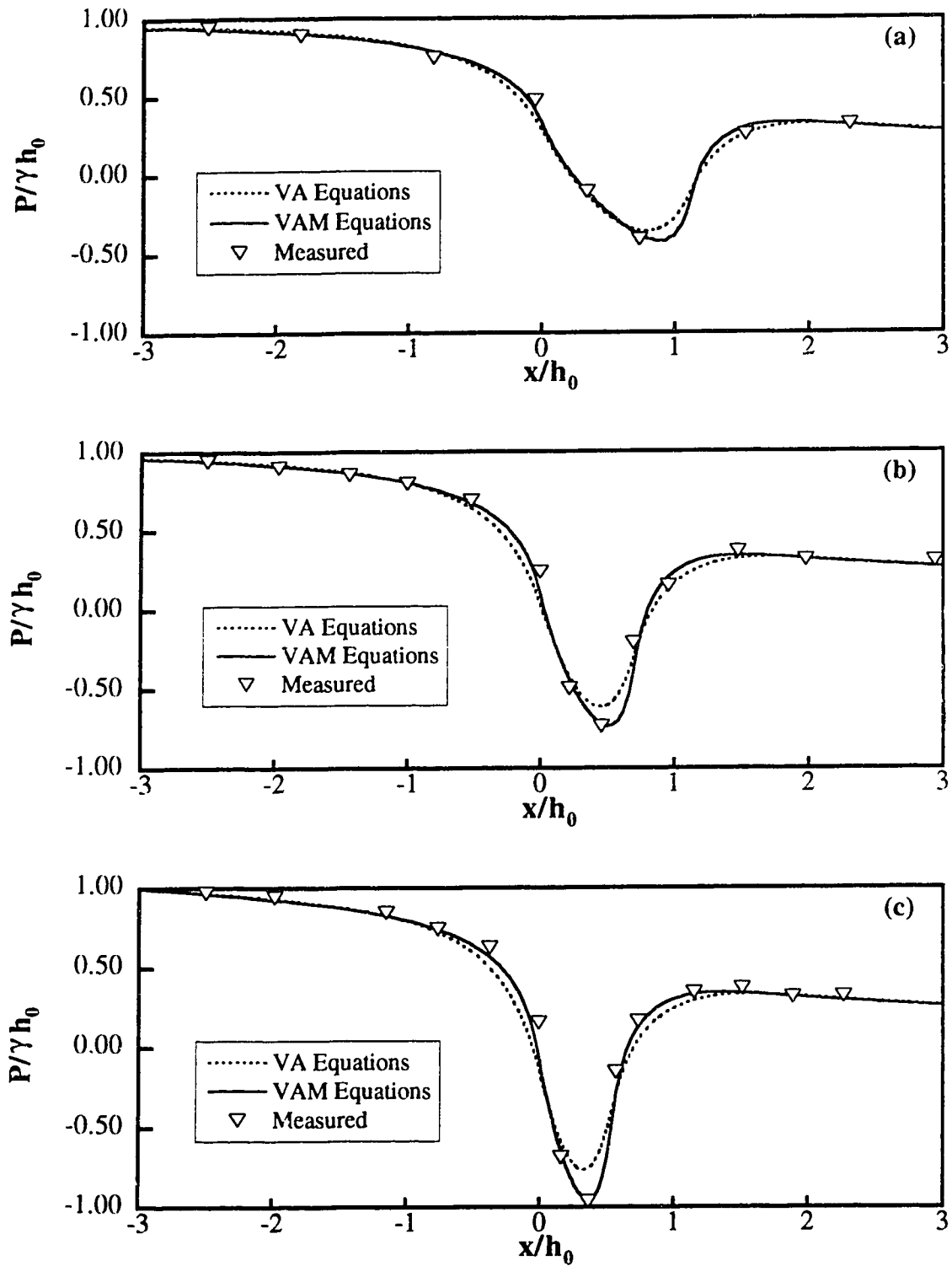
FIG. 2.6. Bed Pressure Profiles for Transition to 45 Degrees Slope:
(a) $Q = 0.02$ m³/s; (b) $Q = 0.04$ m³/s; and (c) $Q = 0.06$ m³/s
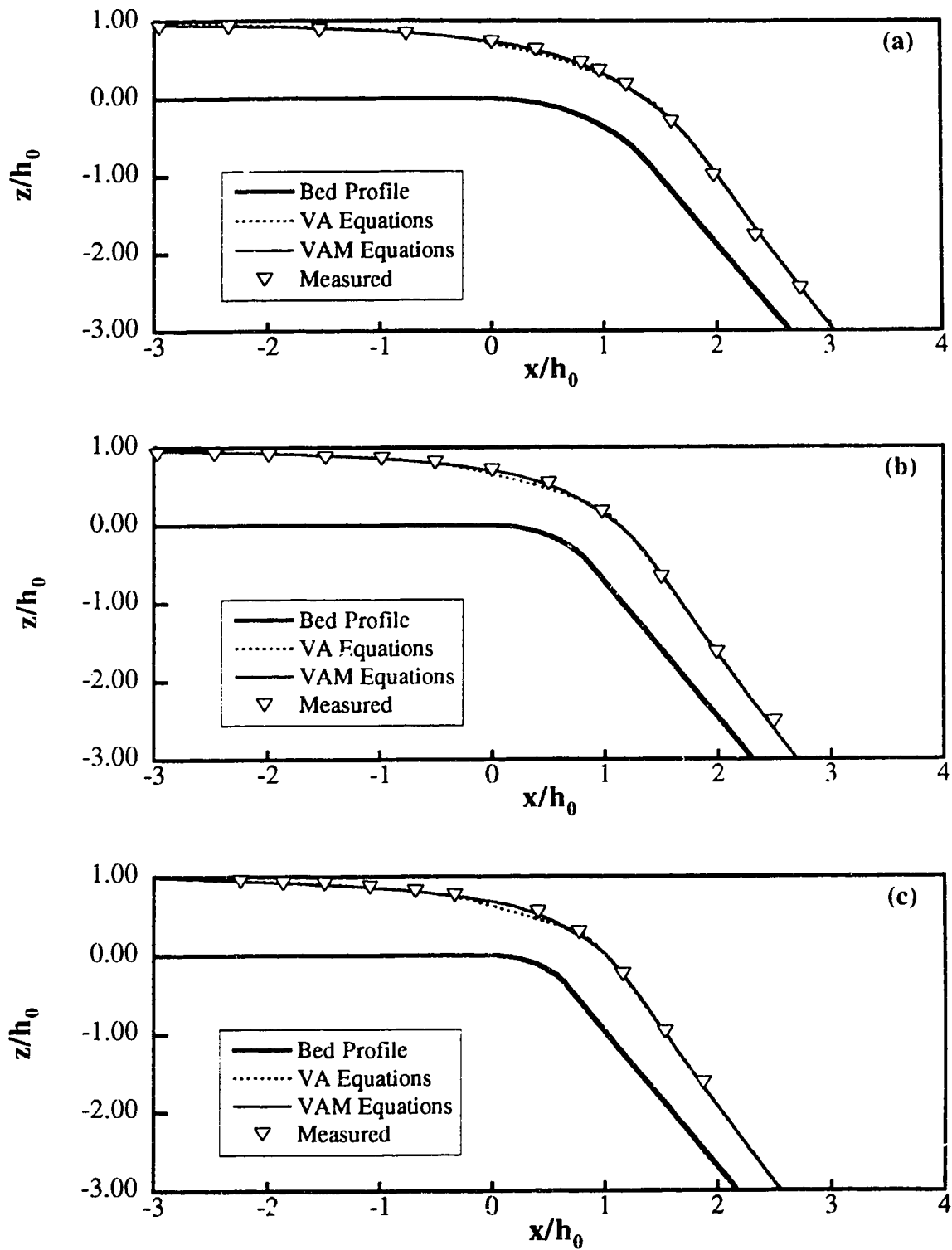
FIG. 2.7. Water Surface Profiles for Transition to 60 Degrees Slope:
(a) $Q = 0.02$ m^3/s; (b) $Q = 0.04$ m^3/s; and (c) $Q = 0.06$ m^3/s
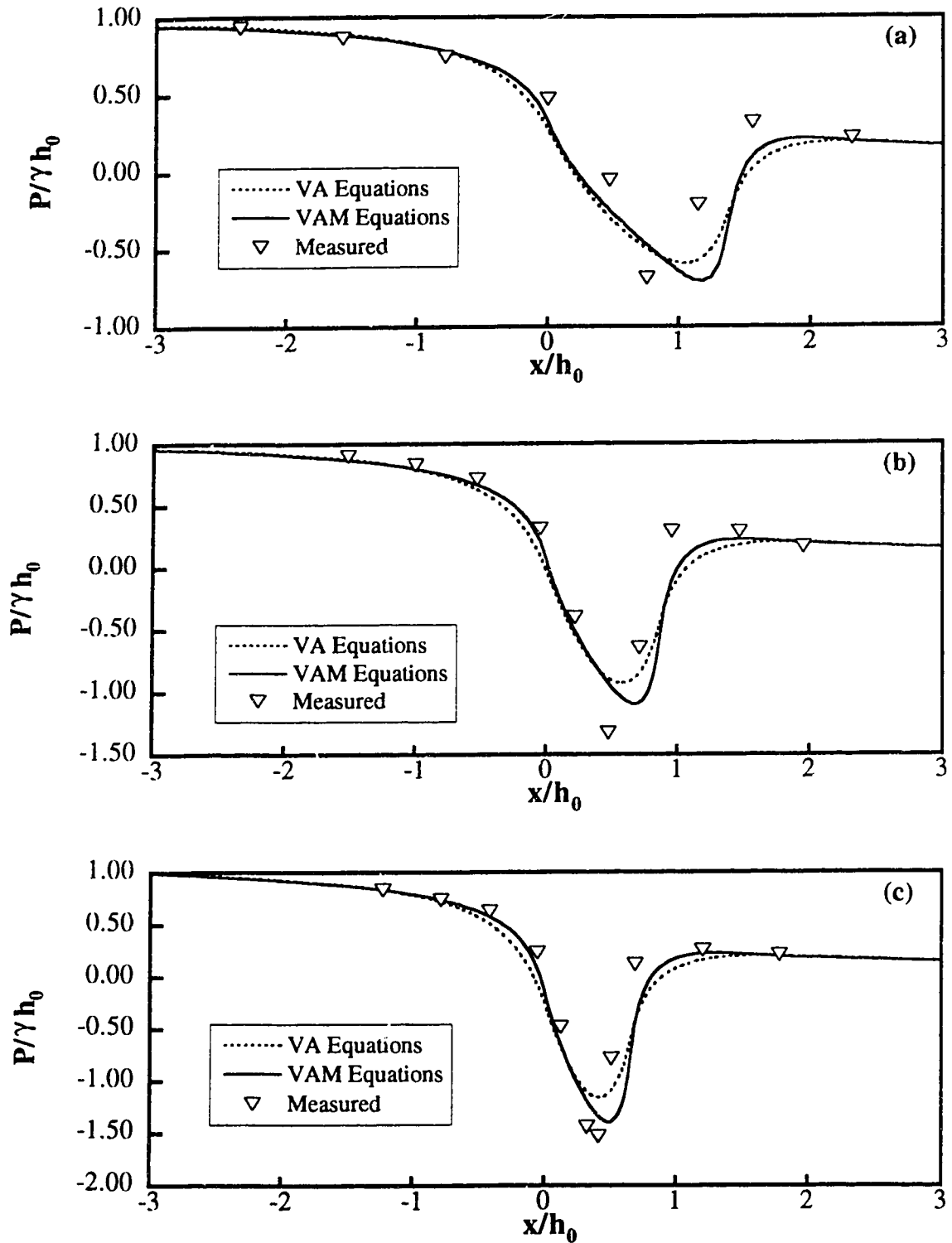
FIG. 2.8. Bed Pressure Profiles for Transition to 60 Degrees Slope:
(a) Q = 0.02 m³/s; (b) Q = 0.04 m³/s; and (c) Q = 0.06 m³/s
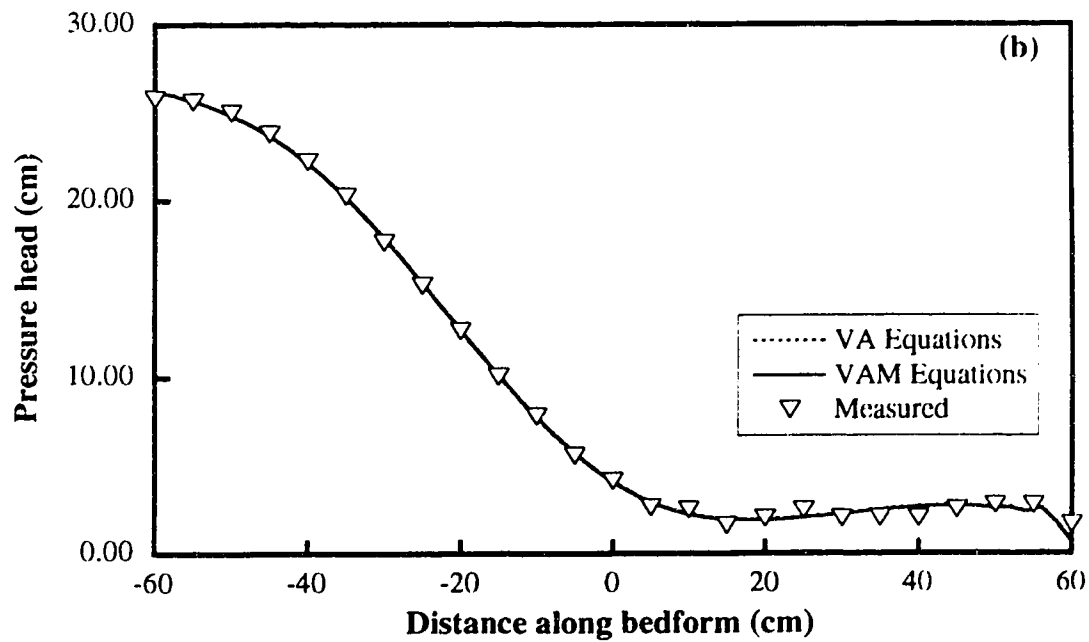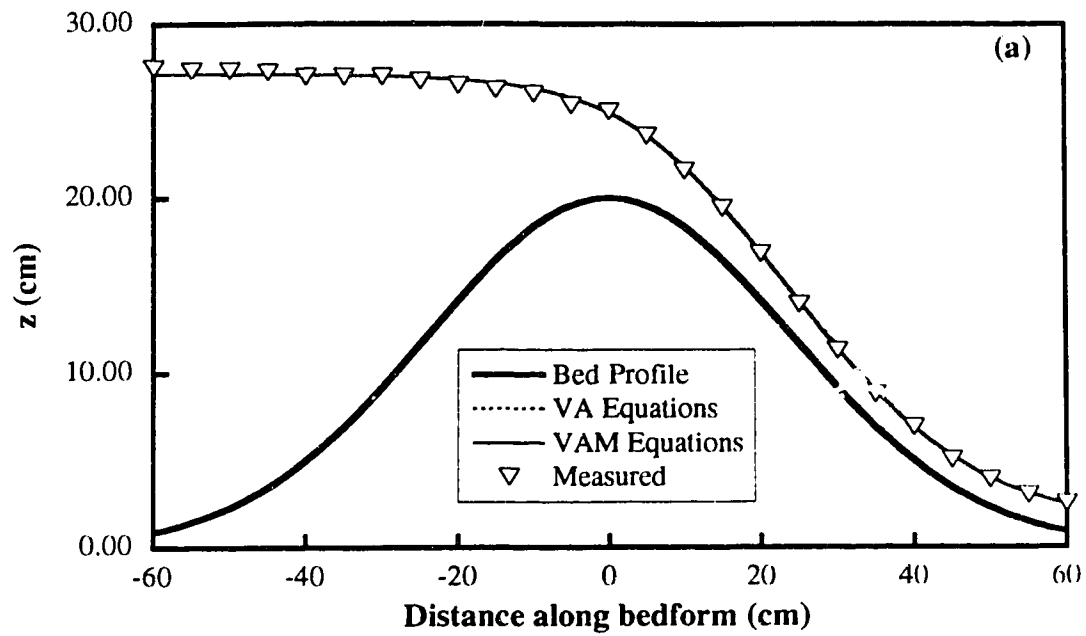
FIG. 2.9. Flow Over Symmetric Bedform (q = 359.9 cm²/s): (a) Water Surface Profile; and (b) Bed Pressure Profile
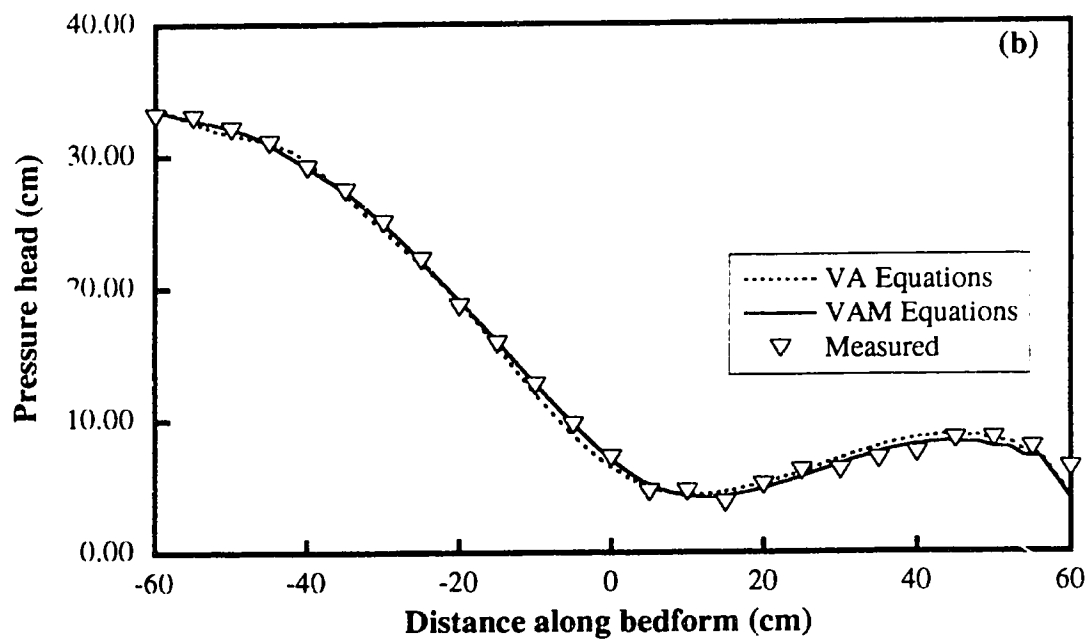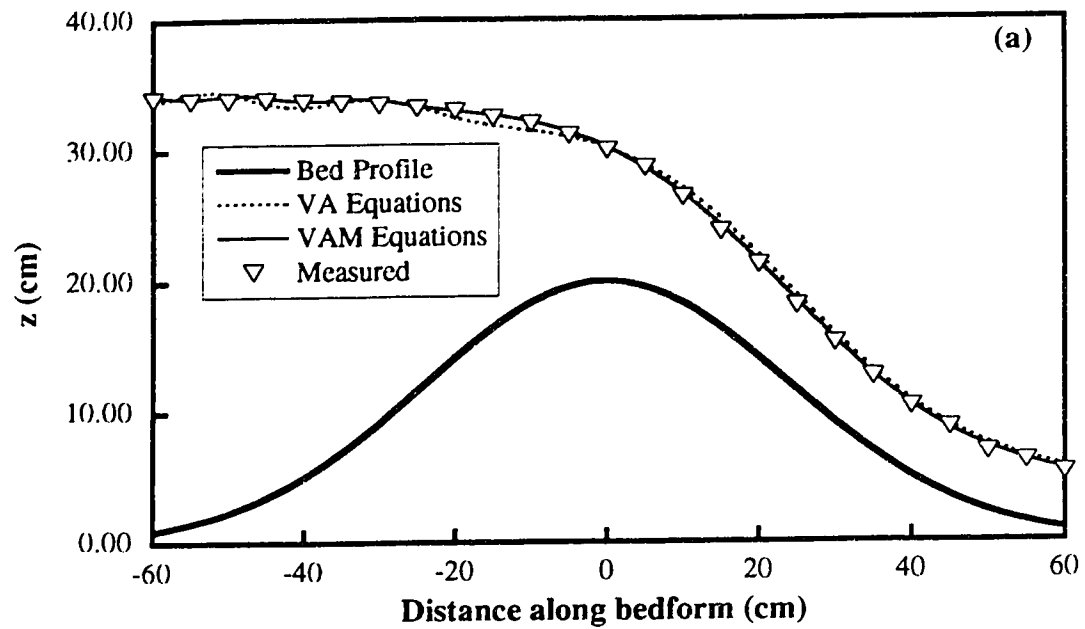
FIG. 2.10. Flow Over Symmetric Bedform (q = 1119.7 cm²/s):
(a) Water Surface Profile; and (b) Bed Pressure Profile

31
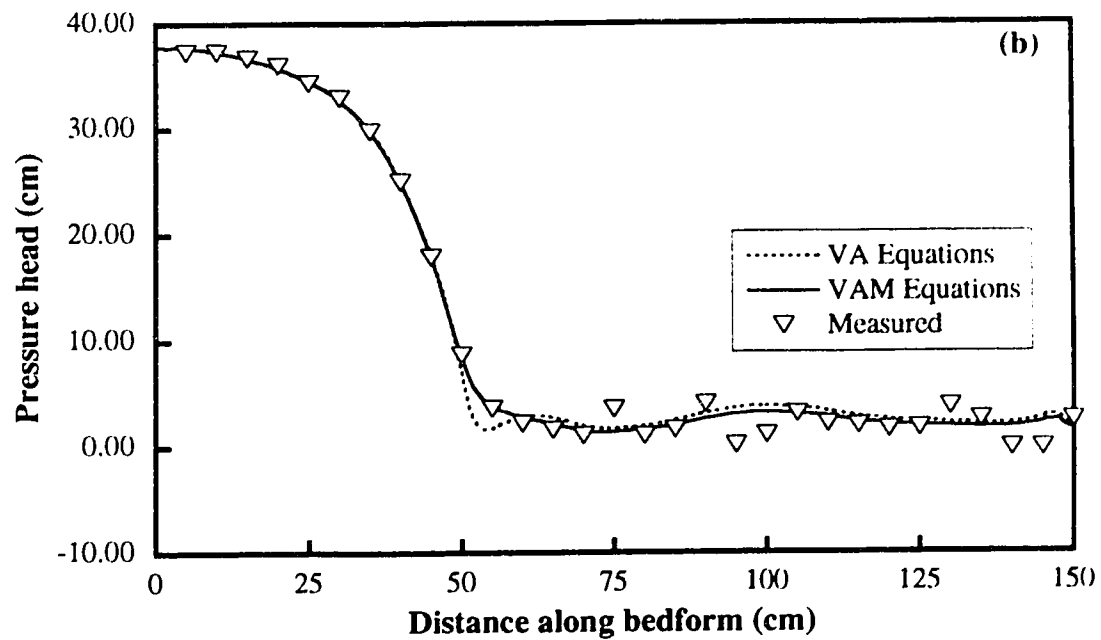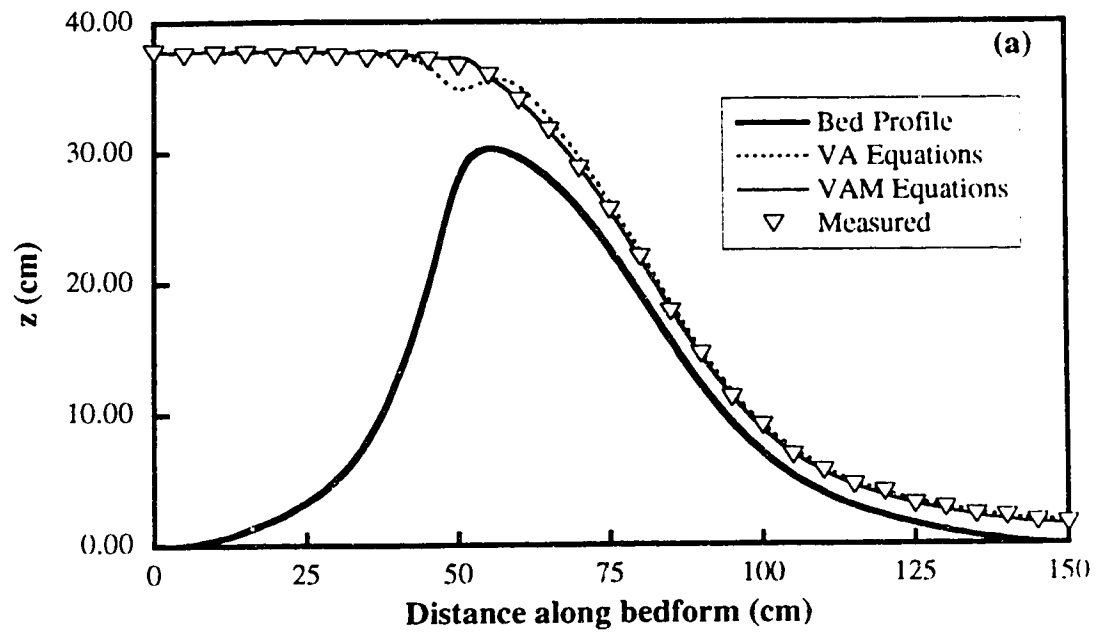
FIG. 2.11. Flow Over Asymmetric Bedform (q = 375.0 cm²/s):
(a) Water Surface Profile; and (b) Bed Pressure Profile
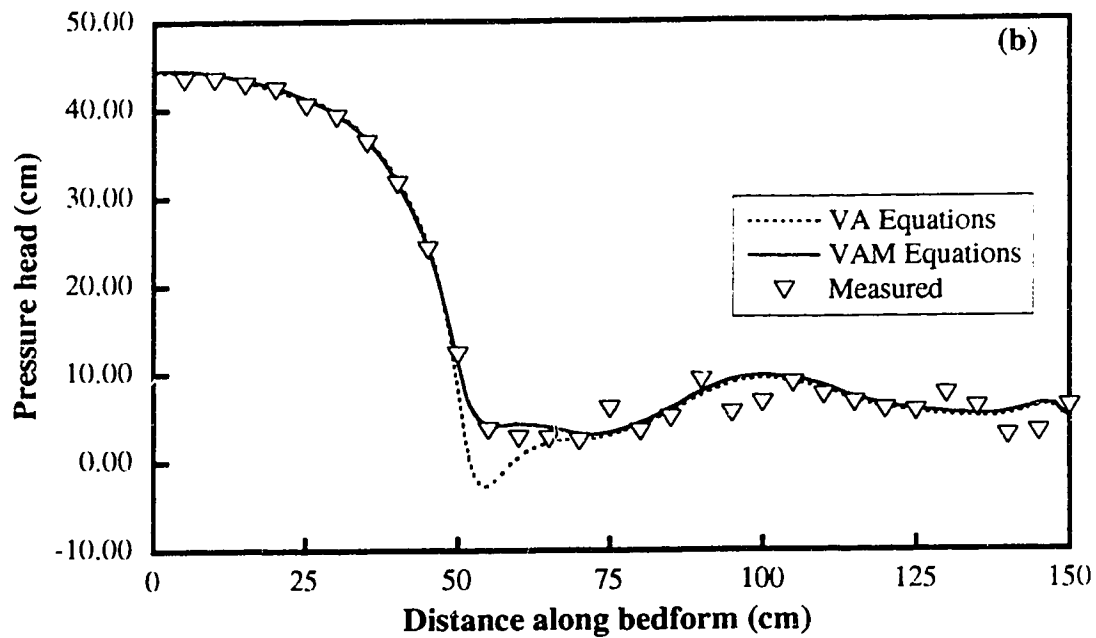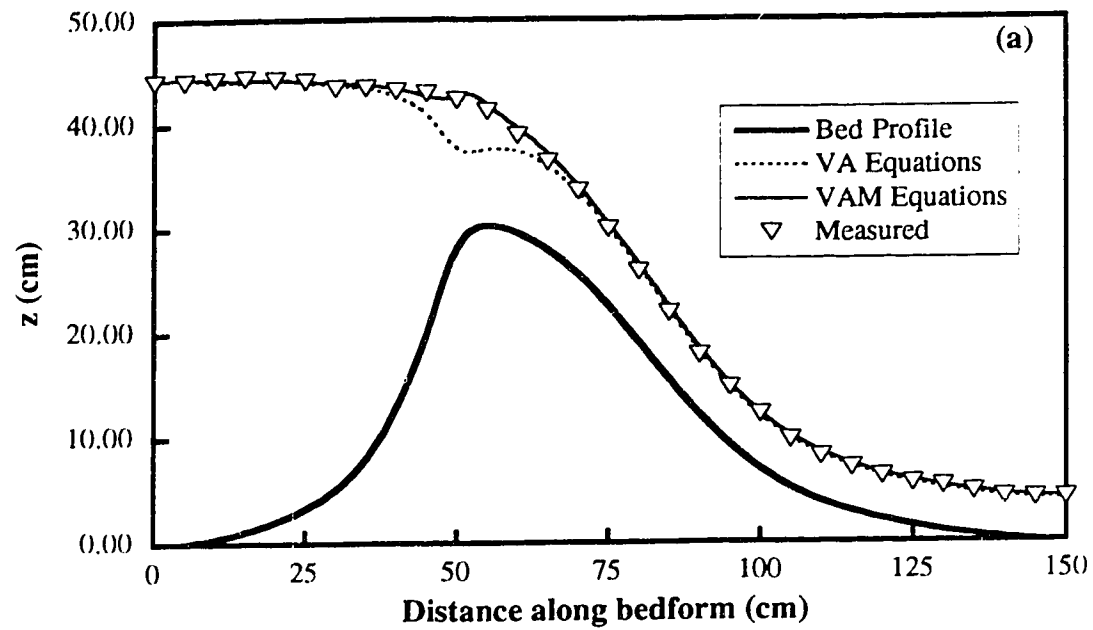
**FIG. 2.12. Flow Over Asymmetric Bedform (q = 1116.5 cm²/s):
(a) Water Surface Profile; and (b) Bed Pressure Profile**

Upstream boundary for numerical models at 10.1 cm from the start of the spillway

Radius = 16.2 cm

70°

20°

Radius = 15.4 cm

90.5 cm

To sump

Head tank

From sump

182.9 cm

Section a-a

Inlet, 82.6 cm long

Seal for side channels

24.5 cm

171.9 cm

46.4 cm

30.5 cm

a

a

Plan view
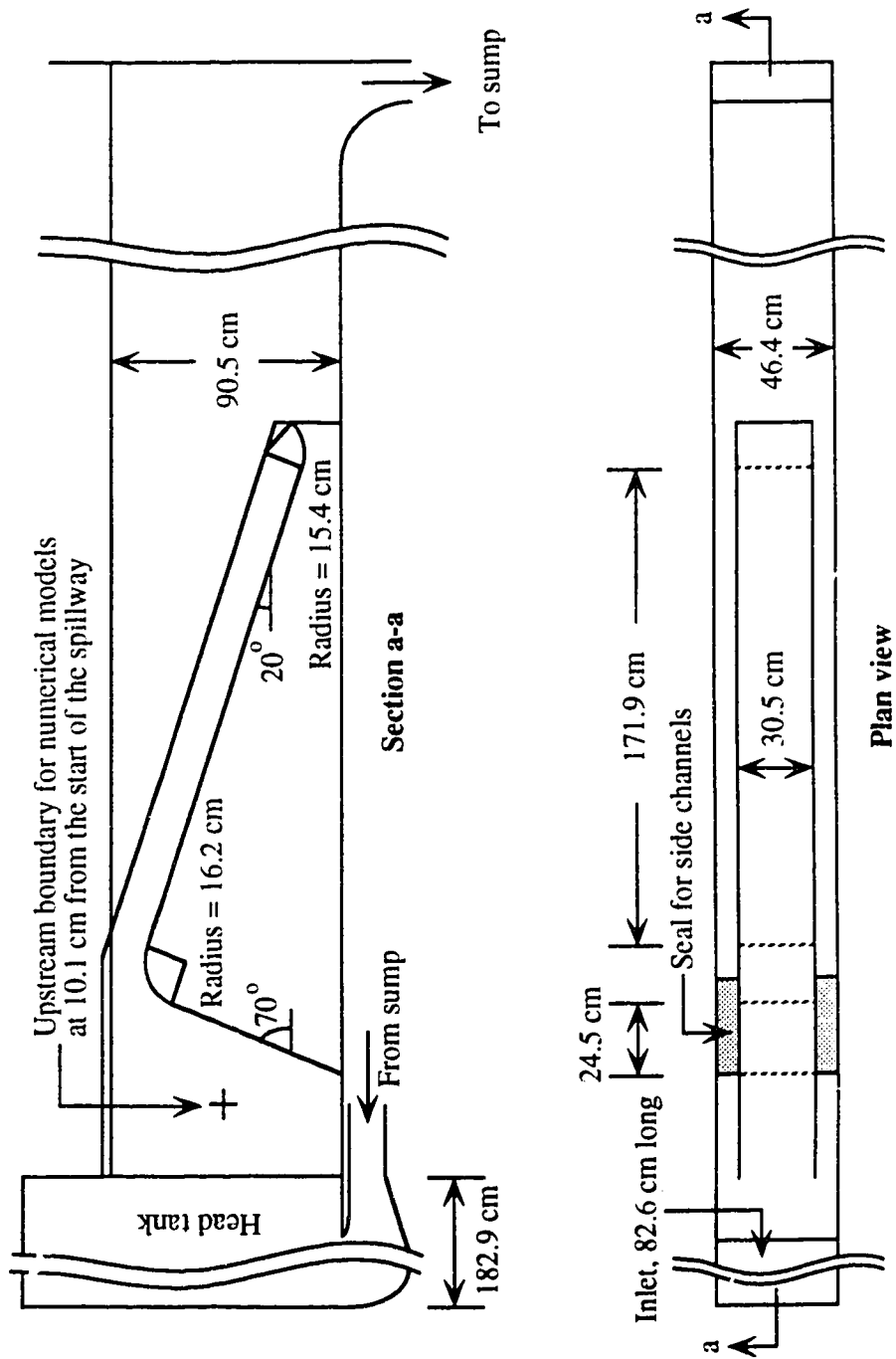
FIG. 2.13. Experimental Set-Up for Flip-Bucket Spillway

34
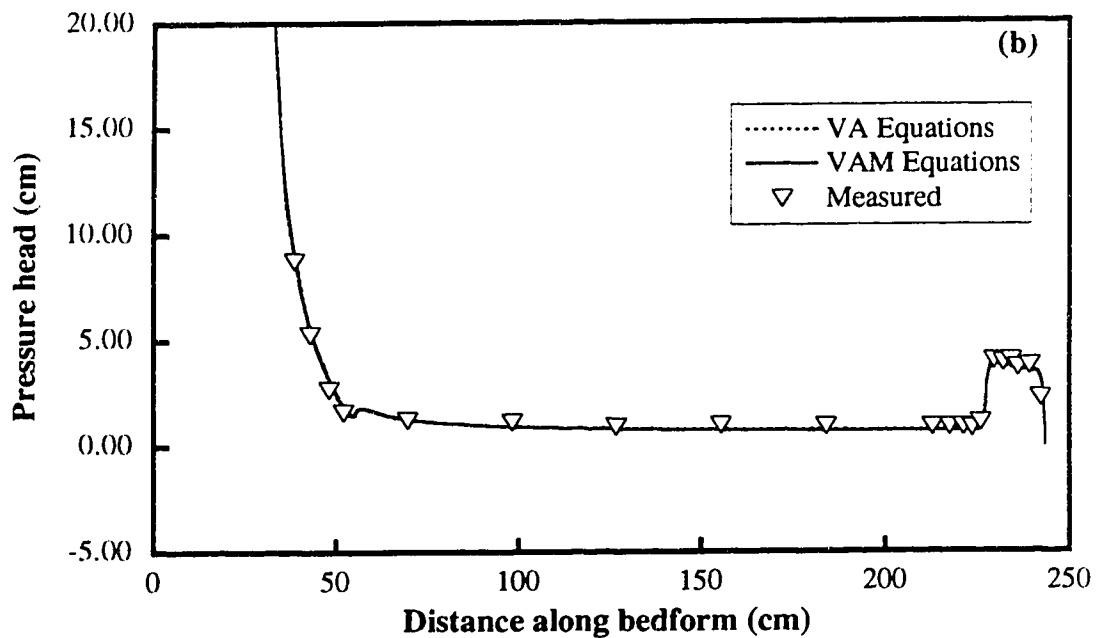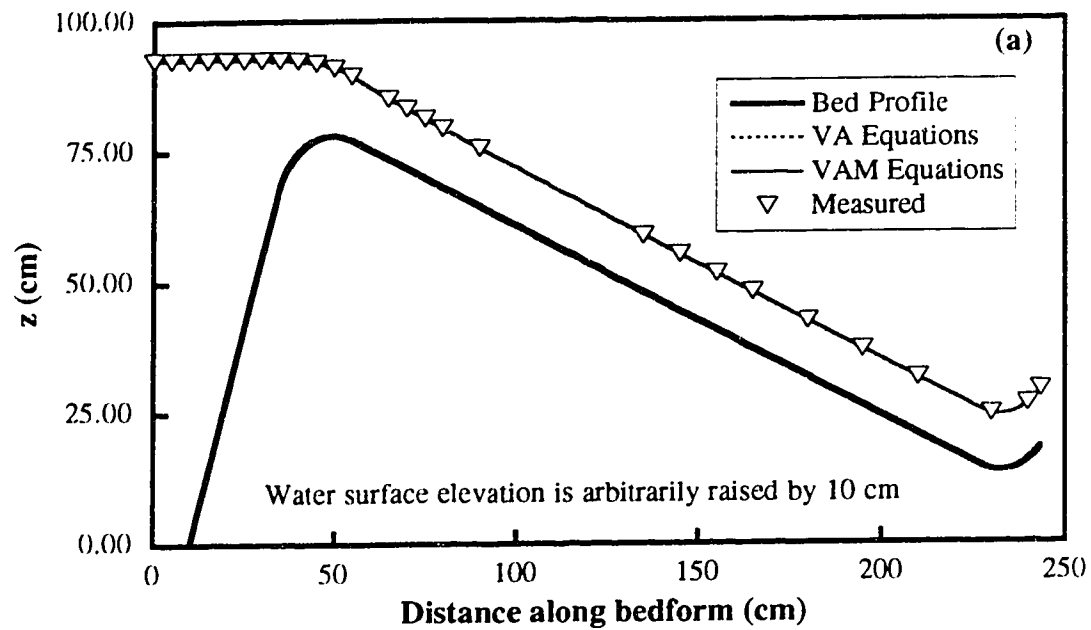
FIG. 2.14. Flow Over Spillway (q = 187 cm²/s):
(a) Water Surface Profile; and (b) Bed Pressure Profile
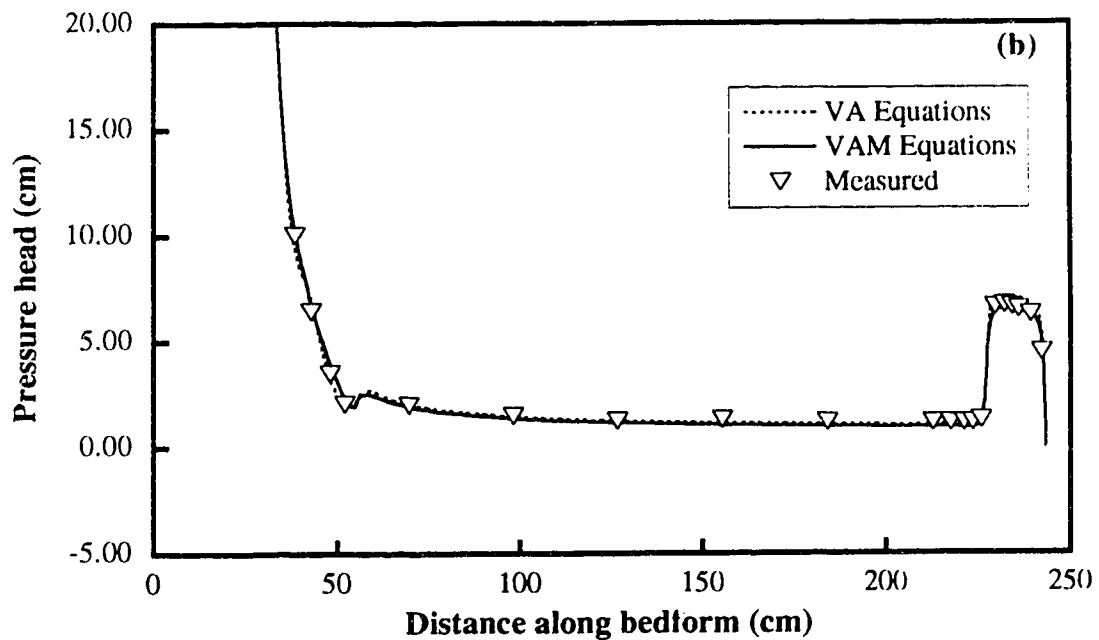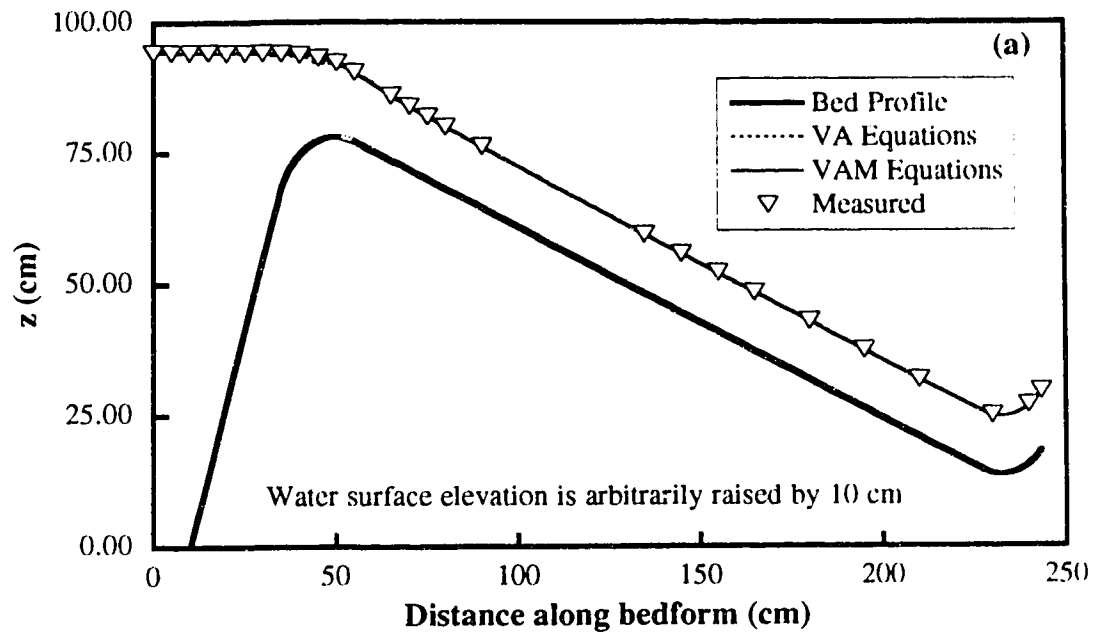
FIG. 2.15. Flow Over Spillway (q = 292 cm²/s):
(a) Water Surface Profile; and (b) Bed Pressure Profile

Chapter 3

Modeling Overfalls Using Vertically Averaged and Moment Equations *

3.1 Introduction

A free overfall represents a vertical drop in a channel with zero submergence. A simple case of the free overfall is a horizontal or sloping channel with a vertical drop or a channel with zero weir height at the end. The study of the simple free overfall is important because of its possible use as a discharge measuring device. However, a relatively more important case, from the point of view of the design of an Ogee spillway, is the study of an overfall with a weir (with a vertical or sloping upstream face) at the end of the channel.

On one hand, the simple free overfall has been extensively studied experimentally, analytically and numerically. Rouse (1936, 1943) experimentally investigated the end depth ratio of the rectangular free overfall, and measured the lower and upper nappe profiles of the free jet issuing from a horizontal rectangular free overfall respectively. Paderi (1954, 1956, 1959), examined experimentally the rectangular free overfall for horizontal, positive and negative bed slopes. These studies mainly focused on the upstream section of the overfall. Rajaratnam et al. (1968, 1972), carried out a detailed experimental study of velocity, pressure and shear stress distribution in the upstream section of the rectangular free overfall for various bed slopes, and studied the effects of bed roughness on the end depth ratio and velocity and pressure distributions at the brink respectively.

Markland (1965) and Clarke (1965), used a two-dimensional potential flow approach with integration by a relaxation method to solve for the surface profile upstream of a rectangular free overfall and the boundaries of the free jet. Strelkoff and Moayeri (1970) used potential flow theory with numerical integration to arrive at the solution of the free rectangular overfall. Ali and Sykes (1971), applied free vortex velocity distribution and curvature to arrive at the end depth and the water surface profile upstream of the overfall for rectangular, triangular and parabolic free overfalls. Hager (1983), applied an analytical approach using an extended Bernoulli equation to solve the rectangular free overfall problem. Recently, Montes (1992), solved the potential flow equations numerically and Marchi (1993) solved analytically the potential flow equations by expanding the stream function in a power series of the vertical distance, to obtain the solution for the rectangular free overfall.

On the other hand, the design of an Ogee spillway, which requires the trajectory of the lower nappe of the jet issuing from a sharp crested weir has been accomplished exclusively through experimental investigation. Although most spillways are designed

with a vertical upstream face, spillways with a sloping upstream face are not uncommon, especially for small irrigation projects. In this study, a different approach is presented to solve the simple free overfall phenomena and at the same time the applicability of the solution is extended to more practical problems by modeling sharp crested weirs with sloping upstream face and rough beds. The equations used are the vertically averaged and moment (VAM) equations recently presented by Steffler and Jin (1993). These equations, although vertically averaged, assume a linear longitudinal velocity profile and quadratic pressure and vertical velocity profiles. To solve for the additional parameters of these assumed distributions, moment equations were generated by vertically averaging the Reynolds equations after being multiplied by the vertical coordinate. In this study, a hybrid Petrov-Galerkin and Bubnov-Galerkin finite element scheme is developed and applied to rectangular free overfalls with smooth and rough beds and sharp crested weirs with sloping upstream faces.

3.2 Equations Modeled

The two-dimensional Reynolds equations were used by Steffler and Jin (1993) to generate three vertically averaged and three moment equations. These equations along with kinematic bed and surface conditions can be used to determine the parameters of the assumed distributions together with the depth and average velocity. Referring to Fig. 3.1, the assumed longitudinal velocity, pressure and vertical velocity distributions are as follows:

$$u \approx u_0 + u_1(2\eta - 1) \quad\text{...(3.1)}$$

$$p \approx (\rho g h + p_1)(1 - \eta) + p_2 4\eta(1 - \eta) \quad\text{...............................(3.2)}$$

$$w \approx w_b(1-\eta) + w_2 4\eta(1-\eta) + w_h \eta \dots\dots\dots(3.3)$$

where u_0 is the vertically averaged longitudinal velocity, u_1 is the longitudinal velocity at the surface in excess of the mean, p_1 is the bed pressure in excess of hydrostatic, p_2 is the mid-depth pressure in excess of the average of the pressures at the bed and surface, w_b and w_h are the vertical velocities at the bed and surface respectively, w_2 is the mid-depth vertical velocity in excess of the average of the vertical velocities at the surface and bed, and g is the gravitational acceleration. The non-dimensional vertical coordinate η is defined by

$$\eta = \frac{z - z_b}{h} \dots\dots\dots(3.4)$$

where z, z_b and h are respectively the vertical coordinate, bed elevation and depth of flow measured vertically.

The vertically averaged continuity, longitudinal momentum, and vertical momentum equations are as follows:

$$\frac{\partial h}{\partial t} + \frac{\partial q}{\partial x} = 0 \dots\dots\dots(3.5)$$

$$\frac{\partial q}{\partial t} + \frac{\partial}{\partial x}\left(\frac{q^2}{h}\right) + \frac{1}{2}\frac{\partial g h^2}{\partial x} + \frac{1}{3}\frac{\partial h u_1^2}{\partial x} + \frac{1}{2\rho}\frac{\partial h p_1}{\partial x}$$

$$+ \frac{2}{3\rho}\frac{\partial h p_2}{\partial x} - \frac{1}{\rho}\frac{\partial h \overline{\sigma}_x}{\partial x} + g h \frac{\partial z_b}{\partial x} + \frac{p_1}{\rho}\frac{\partial z_b}{\partial x} + \frac{\tau_b}{\rho} = 0 \dots\dots\dots(3.6)$$

$$\frac{\partial h\overline{w}}{\partial t} + \frac{\partial q\overline{w}}{\partial x} + \frac{1}{6}\frac{\partial hu_1 w_h}{\partial x} - \frac{hu_1}{6}\frac{\partial w_b}{\partial x} - \frac{1}{6}\left[\left(\frac{q}{h} - u_1\right)\frac{\partial z_b}{\partial x}\right]\frac{\partial hu_1}{\partial x}$$

$$-\frac{1}{\rho}\frac{\partial h\overline{\tau}_{zx}}{\partial x} + \frac{\tau_b}{\rho}\frac{\partial z_b}{\partial x} - \frac{p_1}{\rho} = 0 \dots\dots\dots\dots\dots\dots\dots\dots\dots\dots\dots\dots\dots\dots\dots\dots\dots(3.7)$$

where x is the longitudinal (horizontal) coordinate, t is time, $\overline{\sigma}_x$ and $\overline{\tau}_{xz}$ are the vertically averaged turbulent normal and shear stresses, ρ is fluid density and q $(= hu_0)$ is the discharge per unit width. The depth averaged vertical velocity $\overline{w}$ from (3.3), and bed shear stress τ_b are given by

$$\overline{w} = \frac{w_b}{2} + \frac{2}{3}w_2 + \frac{w_h}{2} \dots\dots\dots\dots\dots\dots\dots\dots\dots\dots\dots\dots\dots\dots\dots\dots\dots\dots\dots(3.8)$$

$$\frac{\tau_b}{\rho} = \frac{\left(u_0^2 + \overline{w}^2\right)}{C_*^2} \dots\dots\dots\dots\dots\dots\dots\dots\dots\dots\dots\dots\dots\dots\dots\dots\dots\dots\dots\dots(3.9)$$

where C_* is the non-dimensional Chezy conveyance coefficient, calculated from

$$C_* = 5.75\log\left(\frac{h}{k_s}\right) + 6.2 \dots\dots\dots\dots\dots\dots\dots\dots\dots\dots\dots\dots\dots\dots\dots\dots(3.10)$$

where k_s is the equivalent sand grain height of the bed roughness. The vertical velocity at the bed and surface are given by the bed and surface kinematic conditions as follows

$$w_b = \left(\frac{q}{h} - u_1\right)\frac{\partial z_b}{\partial x} \dots\dots\dots\dots\dots\dots\dots\dots\dots\dots\dots\dots\dots\dots\dots\dots\dots\dots(3.11)$$

$$w_h = \frac{\partial h}{\partial t} + \left(\frac{q}{h} + u_1\right)\frac{\partial(z_b + h)}{\partial x} \dots\dots\dots\dots\dots\dots\dots\dots\dots\dots\dots\dots\dots\dots(3.12)$$

Three more equations are required for evaluating u_1, w_2, and p_2, which were obtained, by Steffler and Jin (1993), by depth averaging the Reynolds equations after they had been multiplied by the vertical coordinate. The three resulting moment equations are

$$\frac{1}{4}\frac{\partial h^2}{\partial t} + q\frac{\partial \bar{z}}{\partial x} + \frac{1}{6}\frac{\partial h^2 u_1}{\partial x} - h\overline{w} = 0 \dotfill (3.13)$$

$$\frac{\partial u_1}{\partial t} + \frac{\partial}{\partial x}\left(\frac{qu_1}{h}\right) - \frac{1}{2\rho}\left(\frac{\partial p_1}{\partial x} - \frac{p_1}{h}\frac{\partial h}{\partial x}\right) + \frac{4\hat{p}_2}{h\rho}\frac{\partial \bar{z}}{\partial x} - \frac{6}{h\rho}\left(\frac{\tau_b}{2} + \overline{\sigma}_x\frac{\partial \bar{z}}{\partial x} - \overline{\tau}_{xz}\right) = 0 \dotfill (3.14)$$

$$\frac{\overline{w}}{4}\frac{\partial h^2}{\partial t} - \frac{\partial}{\partial t}\left[\frac{h^2}{12}(w_b - w_h)\right] + \left[q\overline{w} - \frac{hu_1}{6}(w_b - w_h)\right]\frac{\partial \bar{z}}{\partial x} - \frac{\partial}{\partial x}\left[\frac{hq}{12}(w_b - w_h)\right]$$

$$+ \frac{\partial}{\partial x}\left[\frac{h^2 u_1}{10}\left(\overline{w} + \frac{w_b}{3} + \frac{w_h}{3}\right)\right] - h\overline{w^2} - \frac{h}{\rho}\left(\overline{\tau}_{xz}\frac{\partial \bar{z}}{\partial x} - \overline{\sigma}_z\right) - \frac{h\tau_b}{2\rho}\frac{\partial z_b}{\partial x} - \frac{2}{3\rho}h p_2 = 0 \dots (3.15)$$

where $\overline{\sigma}_z$ is turbulent normal stress in the vertical direction. In the above equations, the mean square vertical velocity $\overline{w^2}$ (obtained using (3.3)) and the mean bed elevation $\bar{z}$ are given by

$$\overline{w^2} = \overline{w}^2 + \frac{w_b^2}{12} + \frac{w_h^2}{12} - \frac{w_b w_h}{6} + \frac{1}{20}\left(2\overline{w} - w_b - w_h\right)^2 \dotfill (3.16)$$

$$\bar{z} = z_b + \frac{h}{2} \dotfill (3.17)$$

To model the fixed bed and free jet portion of the flow together, both z_b and p_1 are considered to be unknown. For the fixed bed portion of the domain the following additional equation constraining z_b is added to the system

$$\frac{\partial z_b}{\partial t} = 0 \dotfill (3.18)$$

For the free jet portion, (3.18) is replaced by

$$p_1 + \rho g h = 0 \dotfill (3.19)$$

forcing the pressure at the underside of the nappe to be atmospheric. For the applications considered in this study, all involving accelerating flows, the internal turbulent stresses are neglected.

3.3 Numerical Model

Eqs. (3.5)-(3.7), (3.11), (3.12), (3.13)-(3.15), and (3.18) or (3.19) constitute a closed system, both for fixed bed and free jet, with nine unknowns (h, q, p_1 or z_b, w_b, w_h, $\overline{w}$, u_1, p_2, z_b or p_1). Although these equations can be reduced to a system of six equations, the above expanded form is used for numerical modeling to avoid cross and higher order derivatives.

The above set of equations is numerically modeled using a hybrid Petrov-Galerkin and Bubnov-Galerkin finite element schemes. The continuity and longitudinal momentum equations are upwinded using the Characteristic Dissipative Galerkin (CDG-1D) finite element scheme of Hicks and Steffler (1992). This scheme provides selective dissipation for shock capturing. The upwinding parameter for this study is set to 0.5.

The flow situations considered, although steady, are solved as unsteady problems until a final asymptotic solution is reached. For all the tests, initial conditions of constant water surface elevation and discharge are specified for the fixed bed

portion. For the free jet, a constant depth equal to the brink depth and a parabolic lower nappe profile, computed based on the bed slope and longitudinal velocity at the brink, are specified as initial conditions. For the subcritical flow upstream of the overfall or weir, an essential boundary condition for the discharge, and natural boundary condition for the pressures and longitudinal velocity profiles parameters are specified at the upstream boundary. For supercritical flow, in addition to the above conditions an essential boundary condition for the depth is also specified at the upstream boundary. At the junction between the fixed bed and free jet, two internal boundary conditions are imposed. The bed pressure at the brink is forced to be atmospheric and the bed elevation is kept unchanged. For free overfalls with smooth beds and subcritical flow upstream, the upstream boundary for modeling purpose is located near a critical flow section.

The coupled system of non-linear equations is discretized using linear interpolating functions, and the time derivatives are approximated using finite difference formulation. To minimize numerical error, the ratio of depth to spatial discretization, for all tests, is kept between 10 and 20. To accelerate convergence, in addition to using fully implicit time stepping scheme, the time step is geometrically increased. The resulting discretized equations are solved implicitly using a Newton-Raphson iterative scheme with an analytical Jacobian. The convergence of the solution to a new time level is assessed by the following convergence criteria

$$\sqrt{\frac{\Sigma(\delta\Phi)^2}{\Sigma\Phi^2}} \leq \text{'tolerance'} \dots\dots\dots(3.20)$$

where Φ is the vector of unknowns and $\delta\Phi$ is the vector of differences between the Φ vectors at two successive iterations. The convergence to final steady state solution is also assessed using (3.20), with $\delta\Phi$ being the difference between the Φ values at two

44

successive time levels. In this study, for both convergence criteria, a tolerance of 10^{-6} is used.

3.4 Rectangular Free Overfall with Smooth Bed

The data for the rectangular free overfall with smooth horizontal bed, both for the water surface profile upstream of the overfall and lower nappe profiles for the free jet, is obtained from the plots provided by Marchi (1993). Three tests, two for subcritical upstream flow and one for supercritical upstream flow, are conducted and the numerical results are compared with the measured data in each case. The bed shear term is neglected in this case.

Figs. 3.2 to 3.4 show the computed and measured water surface elevation and the lower nappe profile of the free jet for all three cases. The vertically averaged and moment (VAM) equations model both the water surface upstream of the overfall and upper and lower nappe profiles of the free jet extremely well.

To compare the results of the simulated longitudinal velocity, vertical velocity and pressure distributions upstream of the overfall with the measured data, a fourth test with a subcritical upstream flow is conducted. The measured data for this test is obtained from Rajaratnam et al. (1968) and Rajaratnam (1995).

Figs. 3.5 and 3.6 show that the water surface profile and the bed pressure profile along the channel can be modeled accurately using the VAM equations. The pressure profiles at the brink and upstream of the overfall are shown in Fig. 3.7. At the brink, although the maximum pressure is modeled accurately, the limitation of the assumed pressure distribution becomes apparent. The simulated pressure profiles upstream of the brink show good agreement with the measured data.

Fig. 3.8 shows a comparison of the computed longitudinal velocity profiles with that obtained from the two-dimensional potential flow model developed by Montes (1992). Although the assumed linear longitudinal velocity distribution is crude, the agreement is satisfactory. Fig. 3.9 shows the computed and measured vertical velocity distributions at the brink and upstream of the overfall. Although the VAM equations predict slightly lower vertical velocities upstream of the overfall, the agreement is satisfactory.

3.5 Rectangular Free Overfall with Rough Bed

The experimental data for the rectangular free overfall with a rough horizontal bed is obtained from Rajaratnam et al. (1976) and Rajaratnam (1995). The bed shear stress is modeled using (3.9), wherein the non-dimensional Chezy conveyance is evaluated using a k_s value of 1.19 cm as suggested by Rajaratnam et al. (1976). In this case, only the water surface profile upstream of the overfall was available and is compared with the numerical model. Fig. 3.10 shows an excellent match of the measured and computed results.

3.6 Weirs with Sloping Upstream Face

In this case, the data published by Bureau of Reclamation (1948) for sharp crested weirs with sloping upstream faces is used. Three tests for upstream slope of 4:1 (4 horizontal and 1 vertical), 2:1 and 3:3 are examined. The upstream flow in all the above tests was subcritical. The bed shear stress is neglected.

Figs. 3.11 to 3.16 show the comparison of measured water surface profile and the trajectory of the free jet with the computed results. For the upstream weir slope of

4:1 and 2:1, both the water surface elevation and the free jet trajectory are modeled accurately by the VAM equations. For the 45 degree slope, the free jet trajectory is modeled satisfactorily, but the computed results for the water surface elevation upstream of the weir show numerical instabilities for larger weir heights. It is believed that these oscillations are the results of the combined effects of the internal boundary conditions, flow rate, weir height and significant non-linearity of the actual longitudinal velocity profile at the brink.

3.7 Conclusions

In this study, the existing potential flow models for free overfalls, which are valid only for smooth horizontal beds, has been extended using the vertically averaged and moment equations. The VAM equations are applied to horizontal rectangular free overfalls with smooth and rough beds and to sharp crested weirs with sloping upstream faces.

The comparison of computed results with the measured data for rectangular overfalls show the validity of the model for both rough and smooth beds, with excellent results for both the water surface elevation upstream of the overfall and the free jet trajectory. The computed results of vertical velocity and pressure distributions, for the smooth horizontal rectangular overfall, generally show a good agreement with the measured data; while the computed longitudinal velocity profiles compare well with a two-dimensional potential flow model. At the brink section, although the magnitude of the maximum pressure is predicted accurately, the assumed quadratic pressure distribution is limited in predicting the measured pressure profile accurately.

For weirs with upstream slope of 4:1 and 2:1, the computed results are in excellent agreement with the measured results, both for water surface elevation and

free jet trajectory. The water surface profile upstream of the weir, for 45 degree upstream slope and large weir heights, shows numerical instabilities and is thought to be the combined effect of internal boundary conditions, flow rate, weir height and significant non-linearity of longitudinal velocity profile. However, the free jet trajectory is modeled satisfactorily.

References

Ali, K. H. M., and Sykes, A. (1972). "Free-Vortex Theory Applied to Free Overfall." Journal of the Hydraulic Division, ASCE, Vol. 98, HY5, 973-979.

Bureau of Reclamation (1948). "Studies of Crests for Free Overfall Dams." Boulder Canyon Project, Final Reports, Part VI-Hydraulic Investigations, Bulletin 3.

Clarke, N. S. (1965). "On Two-Dimensional Inviscid Flow in a Waterfall." Journal of Fluid Mechanics, Vol. 22, Part 2, 359-369.

Hager, W. H. (1982). "Hydraulics of Plane Free Overfall." J. Hydr. Engrg., ASCE, 109(12), 1683-1697.

Hicks, F. E., and Steffler, P. M. (1992). "Characteristic Dissipative Galerkin Scheme for Open-Channel Flow." J. Hydr. Engrg., ASCE, 118(2), 337-352.

Marchi, E. (1993). "On the Free Overfall." Journal of Hydraulic Research, IAHR, Vol. 31, No. 6, 777-790.

Markland, E. (1965). "Calculation of Flow at a Free Overfall by Relaxation Method." Proceedings of the Institution of Civil Engineers, Vol. 31, 71-78.

Montes, J. S. (1992). "A Potential Flow Solution for the Free Overfall." Proceedings Institution of Civil Engineers, Water, Maritime and Energy, 96, 259-266.

Paderi, F. (1954). "Sulla Chiamata di Sbocco." L' Energia Elettrica, 742-748.

Paderi, F. (1956). "Sulla Chiamata di Sbocco in Canale a Fondo Declive." L' Energia Elettrica, 792-800.

Paderi, F. (1959). "Sulla Chiamata di Sbocco in Canale a Fondo Acclive." L' Energia Elettrica, 883-888.

Rajaratnam, N. (1995). "Personal Communications."

Rajaratnam, N., and Muralidhar, D. (1967). "Characteristics of the Rectangular Free Overfall." Journal of Hydraulic Research, IAHR, Vol. 6, No. 3, 233-258.

Rajaratnam, N., Muralidhar, D., and Beltaos, S. (1976). "Roughness Effects on Rectangular Free Overfall." Journal of the Hydraulics Division, Vol. 102, HY5, 599-614.

Rouse, H. (1936). "Discharge Characteristics of the Free Overfall." Civil Engineering, Vol. 6, No. 4, 257-260.

Rouse, H. (1943). "Discussion to Energy Loss At the Base of Free Overfall." Transactions ASCE, Vol. 108, 1383-1387.

Steffler, P. M., and Jin, Y. (1993). "Depth Averaged and Moment Equations for Moderately Shallow Free Surface Flow." Journal of Hydraulic Research, IAHR, Vol. 31, No. 1, 5-17.

Strelkoff, T., and Moayeri, M. S. (1970). "Pattern of Potential Flow in a Free Overfall." Journal of the Hydraulic Division, ASCE, Vol. 96, HY4, 879-901.
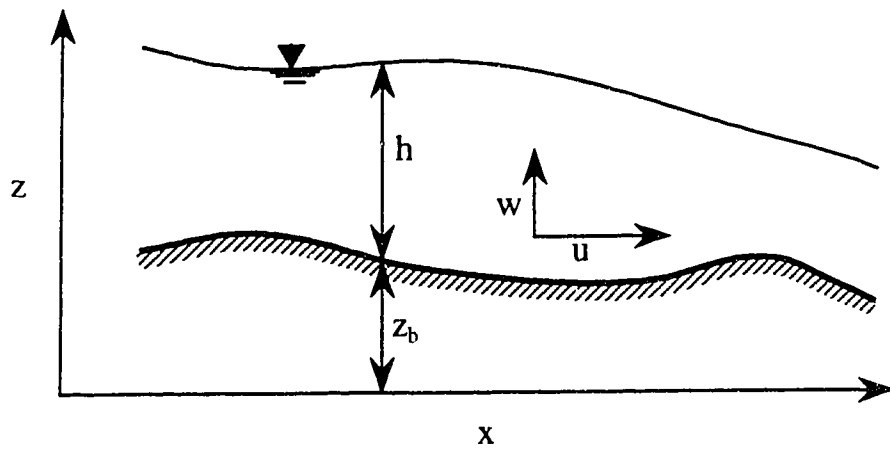
FIG. 3.1. Definition Sketch
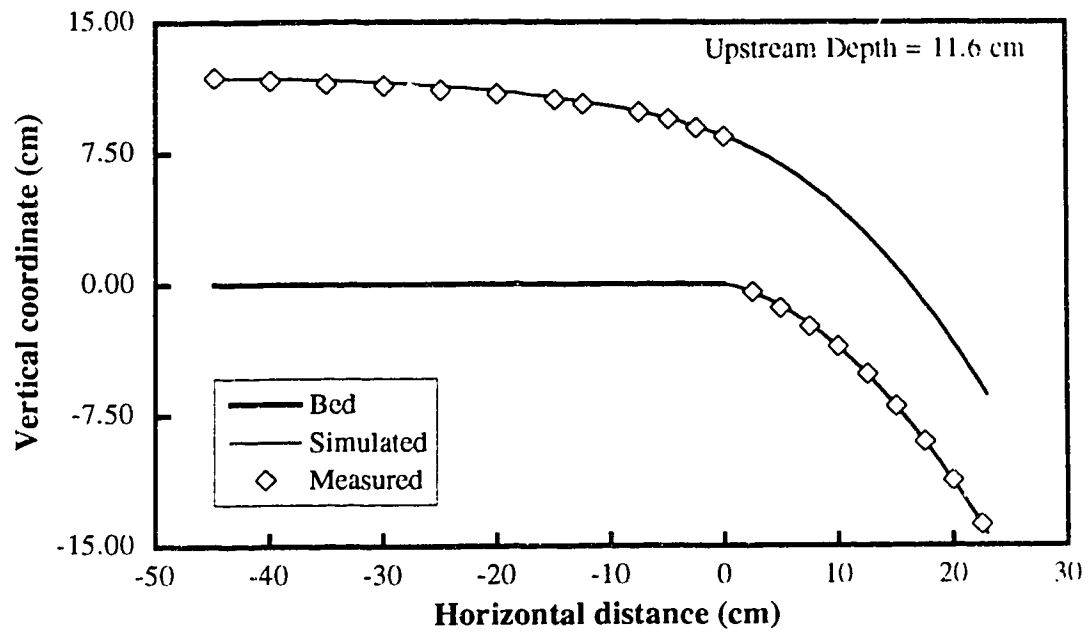
**FIG. 3.2. Free Overfall with Subcritical Upstream Flow
(q = 1269.6 cm²/sec)**
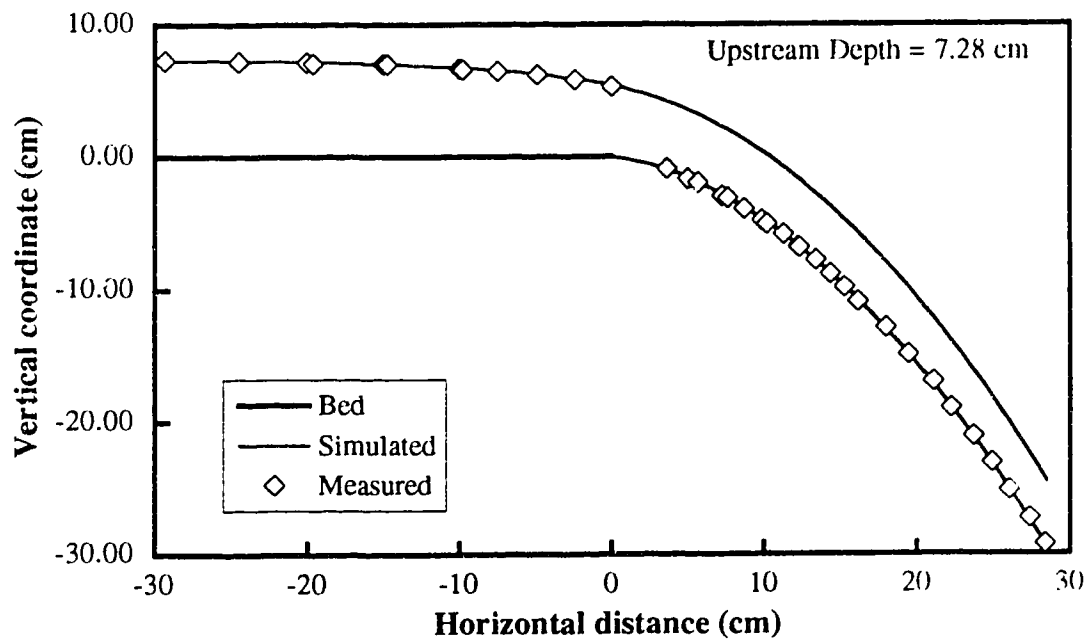
**FIG. 3.3. Free Overfall with Subcritical Upstream Flow
(q = 643.3 cm²/sec)**
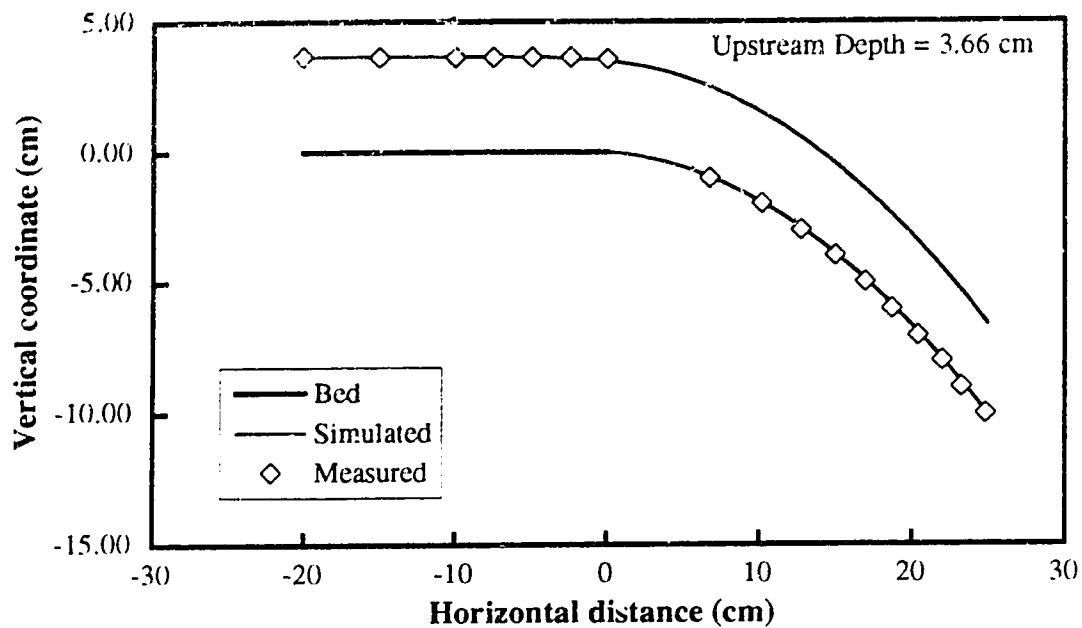
FIG. 3.4. Free Overfall with Supercritical Upstream Flow
(q = 643.3 cm²/sec)
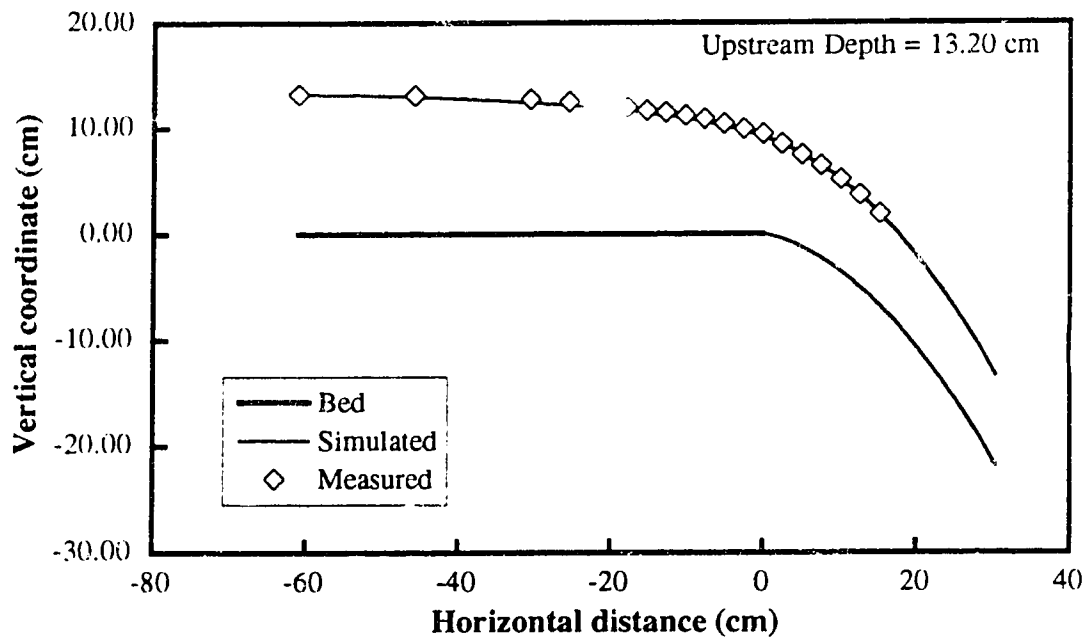
FIG. 3.5. Free Overfall with Subcritical Upstream Flow
(q = 1430.7 cm²/sec)
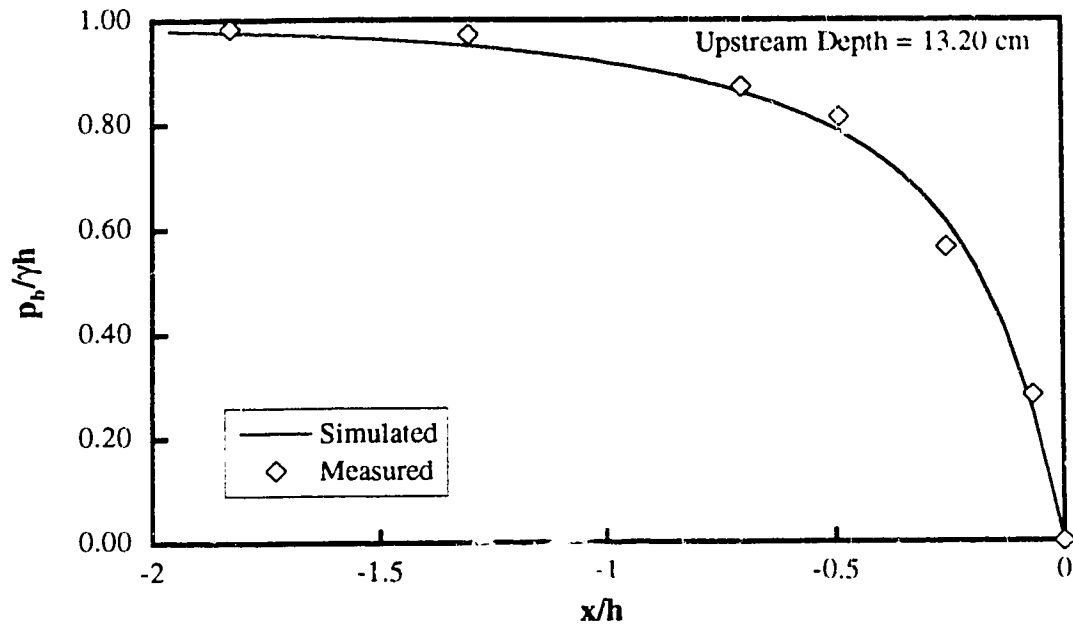
FIG. 3.6. Bed Pressure Along the Channel
(q = 1430.7 cm²/sec)

FIG. 3.7. Pressure Profiles Upstream of the Fall
(q = 1430.7 cm²/sec)

FIG. 3.8. Longitudinal Velocity Profiles Upstream of the Fall
($q = 1430.7$ cm²/sec)
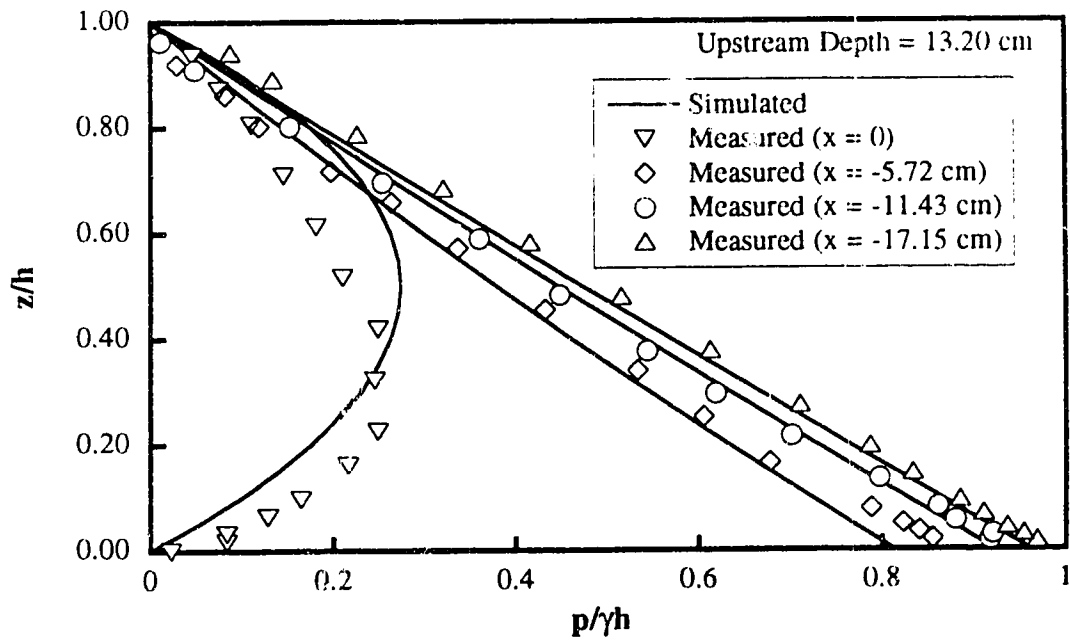
FIG. 3.9. Vertical Velocity Profiles Upstream of the Fall
($q = 1430.7$ cm²/sec)
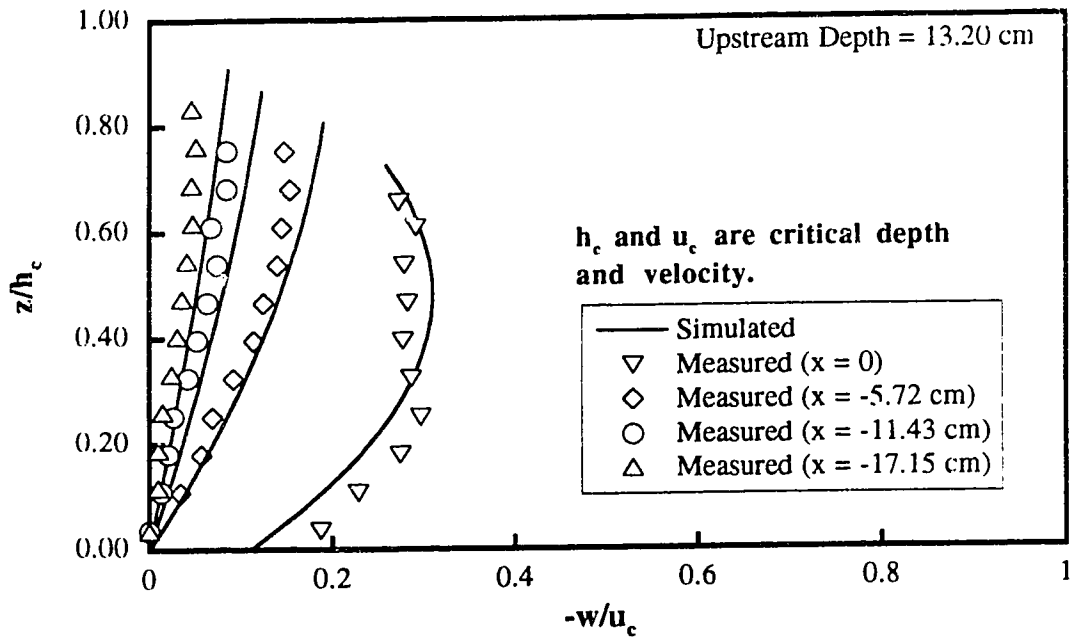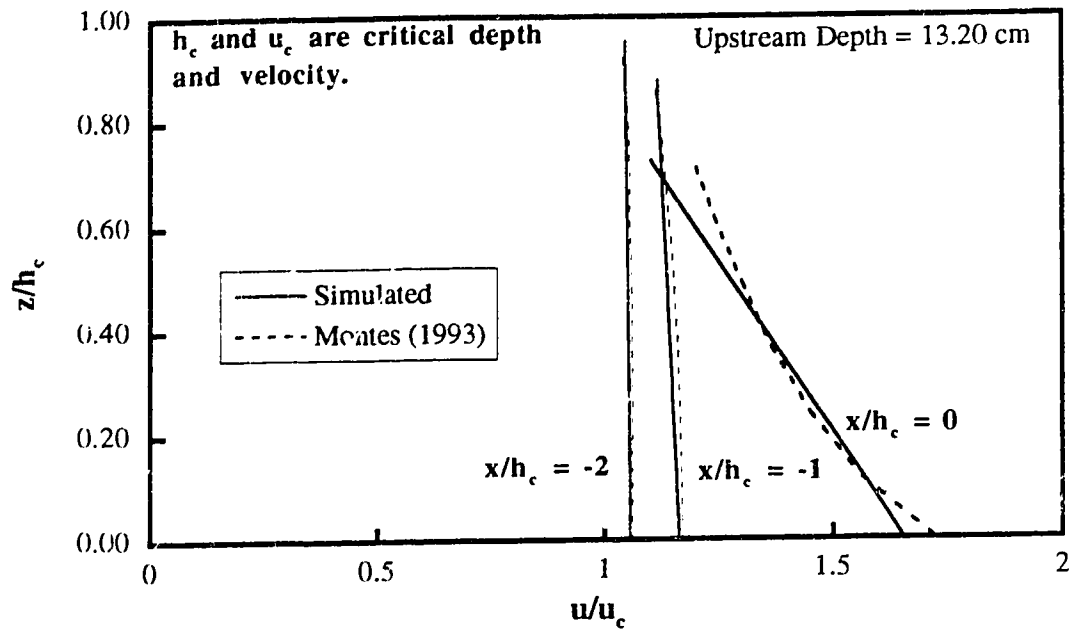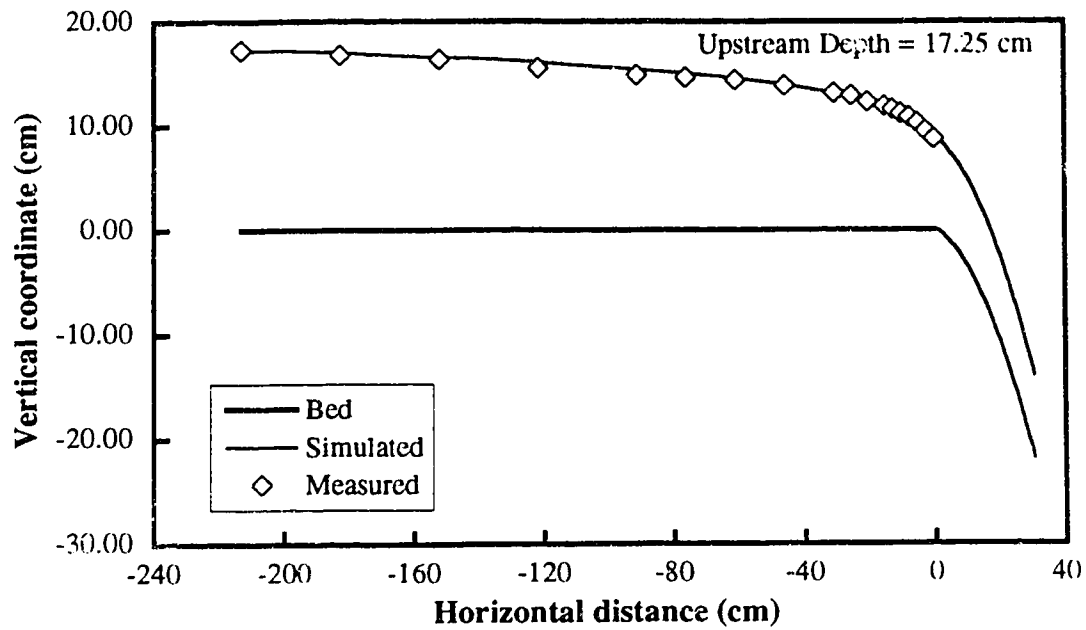
FIG. 3.10. Free Overfall with Rough Bed
(q = 1454.9 cm²/sec)
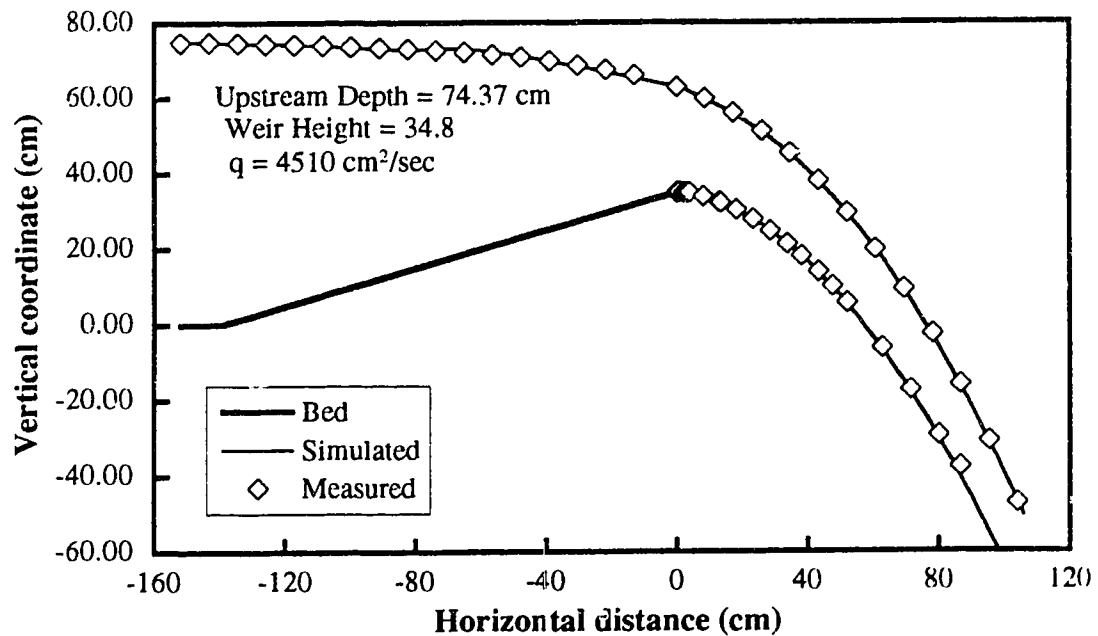
FIG. 3.11. Flow Over a Sharp Crested Weir with Upstream
Face at 4H:1V Slope

56
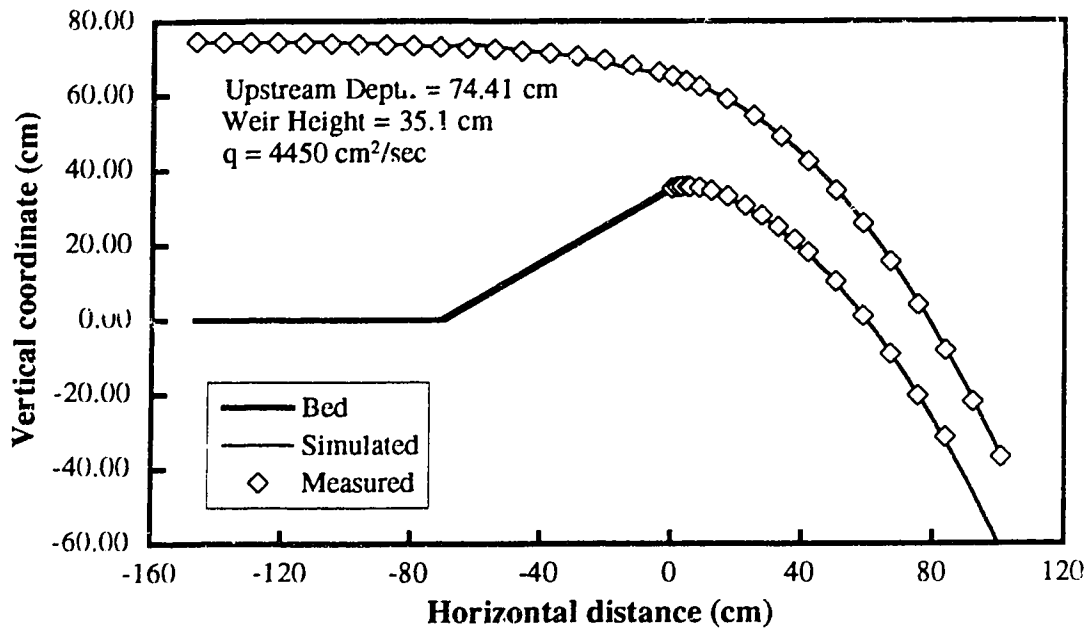
FIG. 3.12. Flow Over a Sharp Crested Weir with Upstream Face at 2H:1V Slope
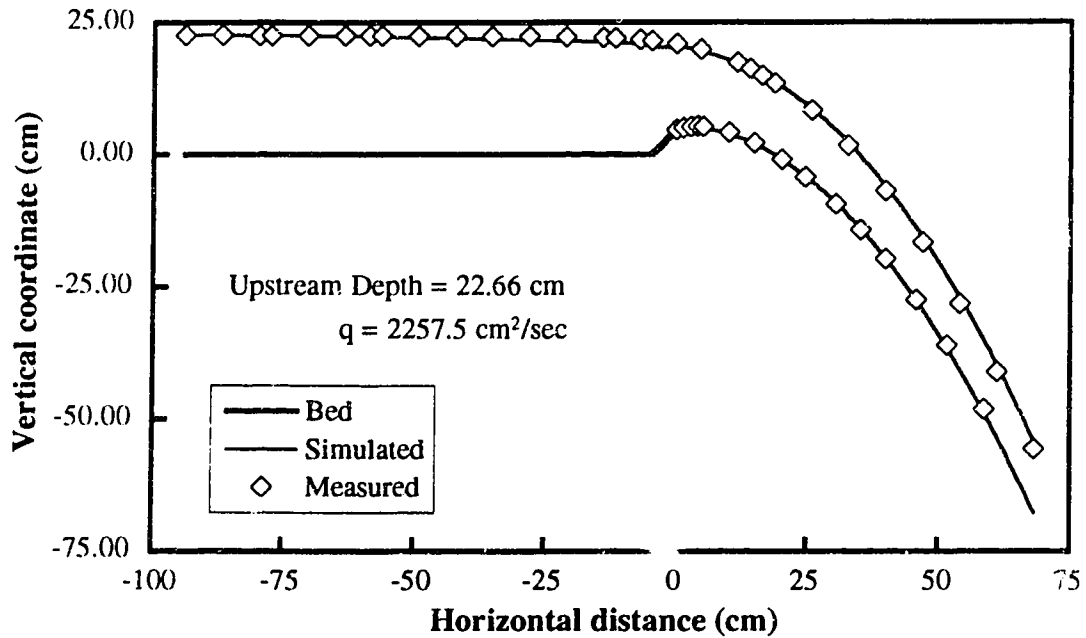
FIG. 3.13. Flow Over a Sharp Crested Weir with Upstream Face at 3H:3V Slope (Weir Height = 4.6 cm)
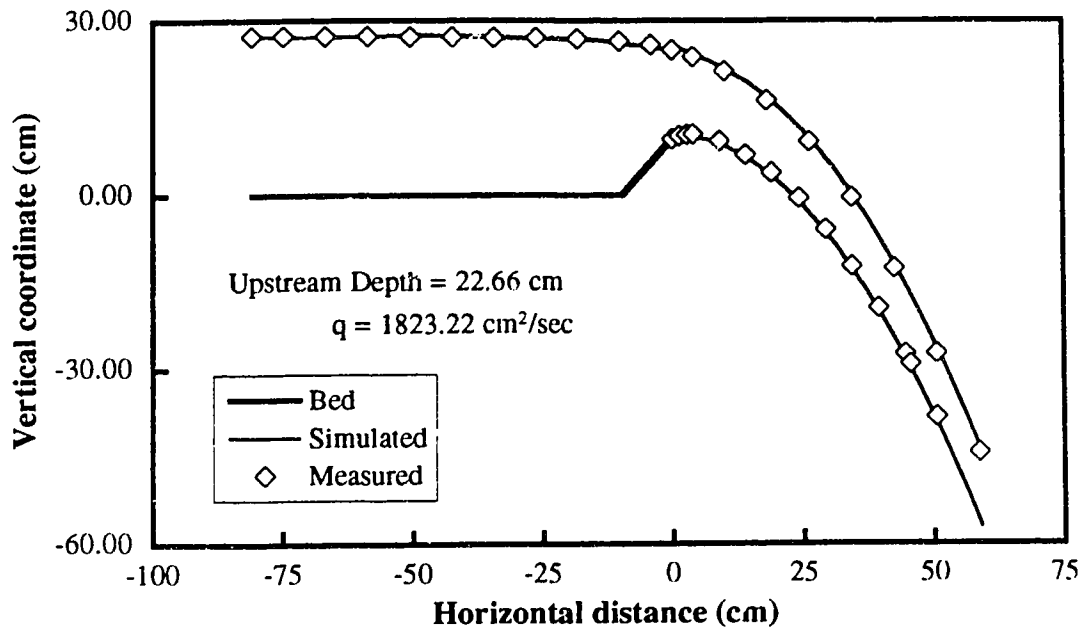
FIG. 3.14. Flow Over a Sharp Crested Weir with Upstream Face at 3H:3V Slope (Weir Height = 9.66 cm)

Upstream Depth = 22.66 cm

q = 1823.22 cm²/sec

- Bed
- Simulated
- ◇ Measured
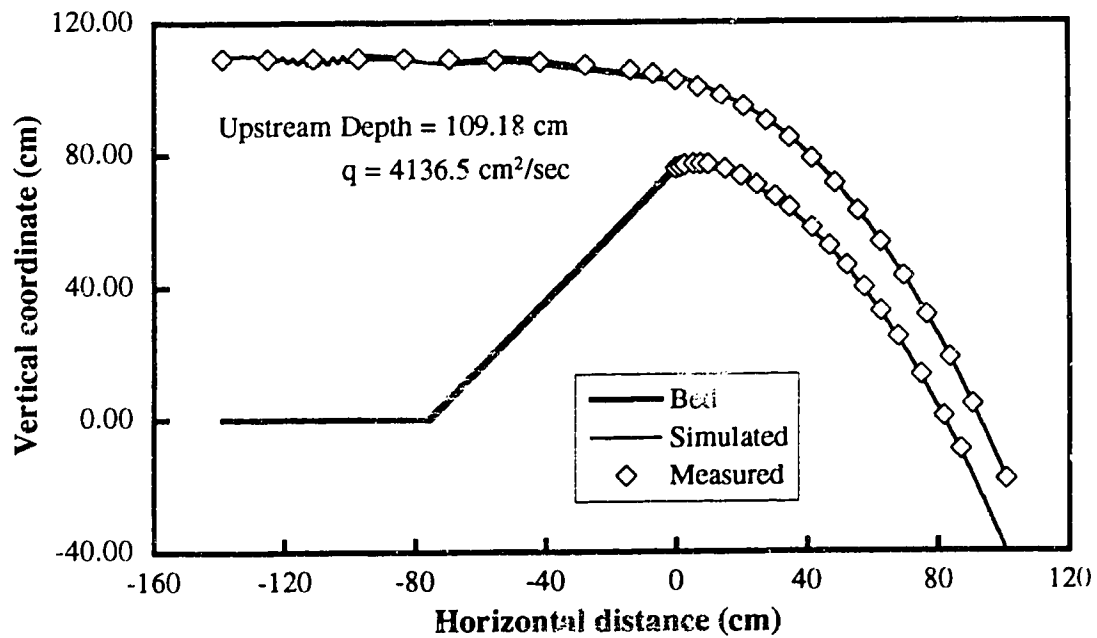
FIG. 3.15. Flow Over a Sharp Crested Weir with Upstream Face at 3H:3V Slope (Weir Height = 75.7 cm)

Upstream Depth = 109.18 cm

q = 4136.5 cm²/sec

- Bed
- Simulated
- ◇ Measured

58

Chapter 4

A Physically Based Hydraulic Jump Model for Depth Averaged Computations *

4.1 Introduction

The hydraulic jump is a transitional state between an upstream supercritical and downstream subcritical flow, and for a given set of flow conditions has a fixed position and length. For design purposes, an open channel flow model should ideally be capable of accurately predicting both the location and length of a hydraulic jump as a part of general flow conditions. Most St. Venant equations models which presently allow jumps, however, treat the jumps as thin shocks, using a dissipative, shock capturing scheme adapted from the gas dynamics methods. The main emphasis is on suppressing

---

* Submitted for publication to the J. Hydr. Engrg., ASCE.

the oscillations before and after the jump and maintaining the momentum balance across the jump (Abbott et al., 1969). The jump location is well predicted but the jump length is necessarily dependent on the spatial discretization, typically spread over one to three intervals. Methods developed include finite difference with an explicit artificial viscosity (e.g. Gharangik and Chaudhry, 1991; Younus and Chaudhry, 1994), or with flux limiters (Jha et al., 1994; Garcia-Navarro et al., 1994) and Petrov-Galerkin finite element schemes (Katopodes, 1984; Hicks and Steffler, 1992).

Gharangik and Chaudhry (1991), attempted to model the hydraulic jump using both the St. Venant and Boussinesq equations. Second and fourth order finite difference shock capturing techniques with added artificial diffusion were used to numerically model these equations. The Boussinesq equations did not give an improved solution while the fourth order scheme was found to be superior to the second order method. The jump length was matched to experimental results but was only two or three discretization intervals long. Younus and Chaudhry (1994) incorporated a depth averaged $k - \varepsilon$ turbulence model but found that the jump length was primarily governed by the numerical diffusion coefficients chosen. It appears that, regardless of the equations and overall numerical scheme, the jump length is still governed by the artificial diffusion and the spatial discretization.

The St. Venant and Boussinesq equations (for sufficiently high upstream Froude numbers) are well known to predict jumps of infinitesimal length, justifying the shock capturing approach. The main limitation of these equations appears to be the assumption of a uniform flow type velocity distribution which cannot generate the turbulent stresses and total momentum flux necessary to spread the jump over its observed length. Any improvement in jump modeling, therefore, must be based on including more physics in the form of velocity, turbulence, and possibly pressure distribution information.

Narayanan (1975) and McCorquodale and Khalifa (1983) used the two-dimensional Reynolds equations with an integral approach for solving hydraulic jumps. An empirical relationship, based on the experimental studies of Rouse et al. (1958) and Resch and Leutheusser (1972), was used to model the turbulent stresses. Madsen and Svendsen (1983), also used an integral method with a one equation turbulence model and were able to predict some of the turbulence characteristics within the jump. While these studies were able to predict some of the detailed characteristics of hydraulic jumps, they are too complex to be incorporated into general open channel flow models.

This study begins with an analysis of momentum conservation within a jump which identifies that the important momentum flux mechanisms governing the jump profile are the velocity distribution and the difference in longitudinal over vertical turbulent stresses. A simplified algebraic stress turbulence model, assuming local equilibrium of production and dissipation, is used to relate the turbulent stresses to the velocity distribution. The velocity distribution is then evaluated using a moment of longitudinal momentum equation, coupled with a simple linear velocity distribution (Steffler and Jin, 1993). A single new momentum flux term is thereby developed which includes one empirical parameter, related mainly to the turbulent length scale. Comparison of numerical solutions with experimental jump profiles shows that a unique value of this parameter gives acceptable results for jumps ranging in Froude number from 2.3 to 7.0. A Petrov-Galerkin finite element scheme, with and without numerical dissipation, is employed to solve these equations.

4.2 Momentum Conservation within a Hydraulic Jump

An analysis of momentum conservation within a hydraulic jump is undertaken to identify the important physical mechanisms which determine the overall

61

characteristic of jump length and profile. Consider a simple, classical, hydraulic jump in a wide rectangular, horizontal channel as shown in Fig. 4.1. The longitudinal coordinate is x and the vertical coordinate is z. At any point along the jump, the mean (time averaged) flow depth is indicated by h and u_0 is the depth averaged mean longitudinal velocity. The time averaged velocity components at any point are indicated by u and w respectively. Section 1 is upstream of the jump and section 2 is downstream.

The depth averaged momentum equation can be derived by integrating the Reynolds equation in the longitudinal direction over the depth of flow. The Liebnitz rule and the kinematic surface condition are used to eliminate terms evaluated at the surface. The resulting equation can be written as

$$\frac{\partial}{\partial x}\int_0^h \rho u^2 dz + \frac{\partial}{\partial x}\int_0^h p\,dz - \frac{\partial}{\partial x}\int_0^h \sigma_x dz = -\tau_b \dotfill (4.1)$$

where ρ is the water density, p is the pressure, σ_x is the Reynolds normal stress, and τ_b is the bed shear stress. Denoting the momentum flux integral as M, the pressure integral as P and the stress integral as S, (4.1) can be integrated from section 1 to any point x along the jump, resulting in

$$(M + P - S) = (M_1 + P_1 - S_1) - \int_{x_1}^{x}\tau_b dx \dotfill (4.2)$$

For the end of the jump, at section 2, (4.2) becomes the usual jump momentum equation

$$(M_2 + P_2 - S_2) = (M_1 + P_1 - S_1) - \int_{x_1}^{x_2}\tau_b dx \dotfill (4.3)$$

Assuming uniform velocity and hydrostatic pressure 'istributions and neglecting the contribution of the turbulent normal stresses and the total bed shear force gives the elementary jump equation;

$$\rho u_{0_1}^2 h_1 + \frac{\gamma h_1^2}{2} = \rho u_{0_2}^2 h_2 + \frac{\gamma h_2^2}{2} = F \quad\text{............(4.4)}$$

where F is the total specific force. An approximate (<1% error for $F_1 > 2$) solution to (4.4) for the sequent depth ratio, f, is (Hager, 1992)

$$f = \frac{h_2}{h_1} = \sqrt{2}F_1 - \frac{1}{2} \quad\text{............(4.5)}$$

where $F = u_0 / \sqrt{gh}$ is the Froude number. For $F_1 = 7.5$, f is very close to 10, which is a useful scale in the following analysis.

Manipulation of (4.4) gives the following relative contributions of the individual momentum balance terms.

$$\frac{M_1}{F} = 1 - \frac{f}{f^3 + 2F_1^2} \quad\text{............(4.6)}$$

$$\frac{P_1}{f} = 1 - \frac{M_1}{F} = \frac{f}{f^3 + 2F_1^2} \quad\text{............}$$

$$\frac{M_2}{F} = 1 - \frac{f^2}{1 + 2F_1^2} \quad\text{............(4.8)}$$

$$\frac{P_2}{f} = 1 - \frac{M_2}{F} = \frac{f^2}{1 + 2F_1^2} \quad\text{............(4.9)}$$

Eq. (4.5) can be used to eliminate the sequent depth ratios so that the right hand side depends on F_1 only. As a rough estimate for jumps in the 6 - 8 Froude number range, take $M_1 / F \approx 1$, $P_1 / F \approx 0$, $M_2 / F \approx 0.1$, and $P_2 / F \approx 0.9$.

The next step is to estimate the contributions to the total specific force within the jump. The mean momentum flux and pressure force contributions can be estimated based upon measured profiles. The remainder gives an estimate of the turbulent stress contribution. This estimate will give some idea of the turbulent intensity within the jump. Consider the point along the jump where the depth is half of the final depth, h_2. This point will be close to the middle of the jump and likely in the vicinity of maximum non-uniformity and turbulence. At this point

$$h = \frac{h_2}{2} \quad \text{..............(4.10)}$$

$$u_0 = \frac{h_1 u_{0_1}}{h_2 / 2} = \frac{2}{f} u_{0_1} \quad \text{..............(4.11)}$$

The mean momentum flux contribution can be evaluated approximately by means of the momentum flux correction factor, β, as in

$$M = \int_0^h \rho u^2 dz = \beta \rho u_0^2 h \quad \text{..............(4.12)}$$

Hager (1992) suggested a function that can be used as a reasonable approximation for the velocity profile for jumps ranging in upstream Froude number from four to nine. This can be expressed as

$$\frac{u - u_s}{u_b - u_s} = \left[\cos\left(\frac{5\pi}{9} \frac{z}{h} \right) \right]^2 \quad \text{..............(4.13)}$$

64

The subscripts indicate bed and surface velocities. Since an estimate of the depth average velocity for the distribution from (4.11) is already available, only one of u_b or u_s needs to be specified. Hager (1992) showed that the maximum backward surface velocity occurs near the middle of the jump and is approximately equal in magnitude to the downstream uniform velocity. Thus

$$u_s = -u_{0_2} = -\frac{h_1 u_{0_1}}{h_2} = -\frac{1}{f} u_{0_1} \dots \dots (4.14)$$

Using (4.11) with (4.13) and (4.14) gives an estimate for the maximum forward velocity at the jump midpoint as

$$u_b = \frac{5.65}{f} u_{0_1} \dots \dots (4.15)$$

This result corresponds very well to the measured maximum velocities as shown in Fig. 2.11 of Hager (1992). From this distribution β can be evaluated and is found to be very close to 2.5. Now the total momentum flux of the mean flow can be estimated as

$$M = \beta \rho u_0^2 h = 2.5 \rho \left(\frac{2}{f} u_{0_1} \right)^2 \frac{h_2}{2} = \frac{5}{f} \rho u_{0_1}^2 h_1 = \frac{5}{f} M_1 \dots \dots (4.16)$$

Thus for a Froude number of 7.5, the total momentum flux of the mean flow represents about 50 percent of the total specific force. Note that the relative contribution decreases as the Froude number increases. Also note that this estimate makes sense only for Froude numbers greater than about 5. Likely, for smaller Froude numbers, β should be smaller than 2.5.

The pressure force can also be estimated based on some presumptions about the pressure distribution within the jump. The pressure distribution is governed by the vertical momentum equation, which can be expressed as

$$u\frac{\partial w}{\partial x} + w\frac{\partial w}{\partial z} = -\frac{1}{\rho}\frac{\partial p}{\partial z} + \frac{\partial \tau_{xz}}{\partial x} + \frac{\partial \sigma_z}{\partial z} - g \quad\text{..............................(4.17)}$$

where τ_{xz} is the Reynolds shear stress and g is the acceleration due to gravity. The first two terms of (4.17) represent the vertical acceleration. Since w is an order of magnitude smaller than u, the first of these terms should be significantly larger than the second. The first term will be positive near the beginning of the jump as the flow begins to expand. Past the middle of the jump, this term will become negative as the flow straightens out into the subcritical parallel flow. It can be expected, therefore, that in the vicinity of the middle of the jump, this term is at a transition and should be close to zero. In terms of curvature, the flow in the upstream half of the jump is concave upwards while in the downstream half the flow is concave downwards. Near the middle, at the maximum upward angle of flow, an inflection point exists where the curvature, and therefore the acceleration, is zero.

Further assume that the longitudinal variation of shear stress and the density variation due to air entrainment can be neglected. Both effects would tend to lead to reduced pressures, but the bulking effect of air entrainment would result in a slightly higher integrated pressure force. As turbulence in the jump is strong, the normal stress is retained. The approximate vertical momentum equation then becomes

$$\frac{\partial}{\partial z}(p - \sigma_z) = -\rho g \quad\text{...(4.18)}$$

Integration as usual leads to the pressure distribution

$$p - \sigma_z = -\rho g (h - z) \quad\text{...(4.19)}$$

The pressure force contribution is therefore

$$P = \int_0^h p\,dz = \rho g \frac{h^2}{2} + \int_0^h \sigma_z\,dz \quad\text{..(4.20)}$$

which indicates that the pressure is effectively hydrostatic, but reduced by the vertical turbulence. Integration gives the pressure force as

$$P = \frac{P_2}{4} + \int_0^h \sigma_z\,dz \quad\text{...(4.21)}$$

Combining the momentum and pressure contributions results in

$$M + P - S = F = \frac{5}{f} M_1 + \frac{P_2}{4} - \int_0^h \sigma_x\,dz + \int_0^h \sigma_z\,dz \quad\text{...........................(4.22)}$$

from which the difference in magnitude of turbulent stresses can be deduced as follows

$$\frac{h \langle \sigma_z - \sigma_x \rangle}{F} = 1 - \frac{5}{f} \frac{M_1}{F} - \frac{1}{4} \frac{r^2}{r^2} \quad\text{...(4.23)}$$

where the angle brackets indicate depth averages. For a Froude number of 7.5, the stress difference appears to account for about 25% of the total specific force. This magnitude may be more easily appreciated by using $M_1 \cong P_2 \cong F$ and substituting the velocity fluctuation correlations for the Reynolds stresses.

$$h\left(\overline{\rho u'^2} - \overline{\rho w'^2}\right) = \left(\frac{3}{4} - \frac{5}{f}\right)\rho h_1 u_{0_1}^2 \quad\text{...(4.24)}$$

which can be written as

$$\left\langle \overline{u'^2} - \overline{w'^2}\right\rangle = \left(\frac{3}{4} - \frac{5}{f}\right)\frac{2}{f}u_{0_1}^2 \quad\text{..(4.25)}$$

The turbulence must be highly anisotropic for this difference to exist. If it is assumed that the vertical intensity is about half of the longitudinal (typical for turbulent shear flows), then an estimate for the typical longitudinal fluctuation can be obtained in terms of the depth ratio and inflow velocity.

$$U' \equiv \sqrt{\left\langle \overline{u'^2}\right\rangle} \approx \sqrt{\left(\frac{3}{4} - \frac{5}{f}\right)\frac{4}{f}}u_{0_1} \quad\text{...(4.26)}$$

For a Froude number of 7.5, the turbulent velocity is about 30 percent of the inflow velocity. In terms of local velocity scales at the jump midpoint, the depth averaged turbulent velocity is approximately 1.5 times the depth averaged velocity or about half of the maximum velocity near the bed. These values are somewhat larger than those reported in experimental studies. Rouse et al. (1958) indicated a value of about 15 percent of inflow velocity for a Froude number of 6.0 while the above estimate is 25 percent. R   nd Leutheusser (1972), also for a Froude number of 6.0, showed about 30 percent for fully developed inflow but much less for undeveloped inflow. The former experiments were performed in a closed conduit which prevented the large scale surface oscillations that are observed in free jumps. The latter experiments were performed with a hot film probe   ay not have been accurate

in flow regions with a high ratio of turbulence to mean flow velocities, particularly where the flow direction was constantly changing. The above estimates, while approximate, indicate that there remains a need for definitive turbulence measurements in a hydraulic jump.

The main conclusion of this analysis is that the momentum transfer effects of the non-uniform mean velocity distribution and the turbulent normal stress difference are both important components of the momentum balance within a jump. For a Froude number of 7.5, these two mechanisms account for about 55 percent of the total momentum flux. The key to a distributed jump model, therefore, is to express these effects in terms of the usual mean flow properties and their gradients. An attempt in this direction is introduced in the following section.

4.3 Depth Averaged Jump Model

The transient St. Venant equations for a wide rectangular channel, neglecting lateral flows, can be written as

$$\frac{\partial h}{\partial t} + \frac{\partial q}{\partial x} = 0 \dots\dots\dots\dots\dots\dots\dots\dots\dots\dots\dots\dots\dots\dots\dots\dots\dots\dots\dots\dots\dots\dots\dots\dots(4.27)$$

$$\frac{\partial q}{\partial t} + \frac{\partial}{\partial x}\left(\frac{q^2}{h}\right) + \frac{\partial}{\partial x}\left(\frac{gh^2}{2}\right) + \frac{\partial J}{\partial x} = gh\left(S_0 - S_f\right)\dots\dots\dots\dots\dots\dots\dots\dots\dots\dots\dots(4.28)$$

where t is time, q ($= hu_0$) is the discharge per unit width, S_0 and S_f are the usual bed and friction slopes respectively. The transient equations are used for generality and to facilitate an orderly development of steady state solutions. J represents the momentum fluxes due to the non-uniform velocity distribution and the turbulent normal stresses.

69

For generality, J should automatically become active in the presence of a jump and be negligible elsewhere. Essentially, the purpose of this paper is to develop and test an expression for J.

From the proceeding section J can be written as

$$J = h\left(\left\langle \overline{u'^2} \right\rangle - \left\langle \overline{w'^2} \right\rangle\right) + (\beta - 1)hu_0^2 \dots\dots\dots(4.29)$$

4.3.1 Velocity Distribution

To proceed, the velocity and turbulence distributions must be specified. For simplicity, a crude linear velocity profile,

$$u \cong u_0 + u_1\left(2\frac{z}{h} - 1\right) \dots\dots\dots(4.30)$$

is assumed. The parameter u_1 is the velocity at the surface in excess of the depth averaged velocity. The corresponding momentum correction coefficient is then

$$\beta = 1 + \frac{1}{3}\left(\frac{u_1}{u_0}\right)^2 \dots\dots\dots(4.31)$$

The second part of the jump flux expression then becomes

$$(\beta - 1)hu_0^2 = \frac{1}{3}hu_1^2 \dots\dots\dots(4.32)$$

4.3.2 Turbulence Model

Leaving the estimation of u_1 for the moment, consider the turbulent stress component of J. Since the anisotropy of the stresses is important, an algebraic stress closure, albeit highly simplified, will be used. From the ASCE Task Committee on Turbulence Models (1988), assuming that the production of turbulence is approximately equal to the dissipation, the turbulent stresses can be written as

$$\overline{u_i'u_j'} = k\left[\frac{2}{3}\delta_{ij} + A\left(\frac{\mathcal{P}_{ij}}{\varepsilon} - \frac{2}{3}\delta_{ij}\right)\right] \dots\dots\dots(4.33)$$

where i and j are tensor indices for the three coordinate directions, k is the turbulent kinetic energy, δ_{ij} is the Kronecker delta (= 1 for $i = j$, = 0 for $i \neq j$), A is a modeling constant and ε is the rate of dissipation of turbulent energy. The components of production of turbulent energy, $\mathcal{P}_{ij}$, are given by

$$\mathcal{P}_{ij} = -\overline{u_i'u_l'}\frac{\partial u_j}{\partial x_l} - \overline{u_j'u_l'}\frac{\partial u_i}{\partial x_l} \dots\dots\dots(4.34)$$

From the measurements of Rouse et al. (1958), turbulence production is greater than dissipation in the upstream part of the jump while dissipation is greater than production in the downstream. Production equal to dissipation appears to be a reasonable approximation near the middle of the jump and leads to considerable simplification. Further simplification can be obtained by consideration of the order of magnitude of the velocity gradients in (4.34). If the lateral mean velocity and lateral gradients are zero, estimates for the remaining gradients near the middle of jump are:

71

$$\frac{\partial u}{\partial z} \sim \frac{u_s - u_b}{h} \sim \frac{13}{f} \frac{u_{0_1}}{h_2}$$

$$\frac{\partial u}{\partial x} \sim \frac{1}{5} \frac{u_{0_1}}{h_2}$$

$$\frac{\partial w}{\partial z} \sim \frac{u_0}{5h} \sim \frac{1}{f} \frac{u_{0_1}}{h_2} \qquad\qquad\qquad\qquad\qquad\qquad\qquad (4.35)$$

$$\frac{\partial w}{\partial x} \sim 0$$

Clearly the vertical gradient of the longitudinal velocity is by far the largest for any Froude number. By estimating that $\overline{u'^2} \sim 2\overline{w'^2} \sim 3\overline{u'w'}$, then (4.34) can be simplified to

$$\wp_{xx} \cong -2\left(\overline{u'w'}\frac{\partial u}{\partial z} + \overline{u'^2}\frac{\partial u}{\partial x} \right) \qquad\qquad\qquad\qquad (4.36)$$

$$\wp_{xz} \cong -\overline{w'^2}\frac{\partial u}{\partial z} \qquad\qquad\qquad\qquad\qquad\qquad\qquad (4.37)$$

and

$$\wp_{zz} \cong 0 \qquad\qquad\qquad\qquad\qquad\qquad\qquad\qquad\qquad\qquad (4.38)$$

The second term of (4.36) should be about half the size of the first term, as the size of the stress partially compensates for the smaller gradient. In the following development this term will be neglected, but an allowance will be made by allowing adjustment of a model constant.

The turbulent stresses can then be evaluated as

$$\overline{u'^2} \cong \frac{2}{3}k(1-A) + \frac{4}{3}\frac{A^2 k^3(1-A)}{\varepsilon^2}\left(\frac{\partial u}{\partial z}\right)^2 \quad \text{.........................(4.39)}$$

$$\overline{w'^2} \cong \frac{2}{3}k(1-A) \quad \text{.........................(4.40)}$$

and

$$\overline{u'w'} \cong -\frac{2}{3}\frac{k^2 A(1-A)}{\varepsilon}\frac{\partial u}{\partial z} \quad \text{.........................(4.41)}$$

The assumption of production equal to dissipation, as well as using only the largest of the production terms, allows us to write

$$-\overline{u'w'}\frac{\partial u}{\partial z} = c_D \frac{k^{3/2}}{L} \quad \text{.........................(4.42)}$$

where L is a turbulent length scale and c_D is a model constant. Substitution of (4.41) allows evaluation of k and ε which may then be reintroduced into (4.39) -(4.41). The final result can be expressed as

$$\overline{u'^2} \cong a\ell_m^2\left(\frac{\partial u}{\partial z}\right)^2 \quad \text{.........................(4.43)}$$

$$\overline{w'^2} \cong b\ell_m^2\left(\frac{\partial u}{\partial z}\right)^2 \quad \text{.........................(4.44)}$$

and

$$\overline{u'w'} \cong -\ell_m^2 \left|\frac{\partial u}{\partial z}\right|\left(\frac{\partial u}{\partial z}\right) \qquad\qquad (4.45)$$

where

$$\ell_m^2 = \left[\frac{2}{3}A(1-A)\right]^{3/2}\frac{L^2}{c_D^2} \qquad\qquad (4.46)$$

is the effective mixing length. The constants a and b are, in principle, functions of A only. Using $A \cong 0.25$, for example, gives $a \cong 0.28$ and $b \cong 0.14$. In view of the gross simplifications made, however, these constants will be allowed to be adjustable. In particular, it is expected that a should be somewhat larger to account for the neglected longitudinal gradient production term. The key point of the preceding analysis is the final form of (4.43) - (4.45), wherein the turbulent stresses are separately related to the principal velocity gradient.

An estimate for the average velocity gradient can be obtained directly form the assumed distribution, (4.30), as

$$\frac{\partial u}{\partial z} \cong \frac{u_i}{h} \qquad\qquad (4.47)$$

In addition, it will be assumed that the average mixing length is a proportion, α_0, of the flow depth

$$\ell_m = \alpha_0 h \qquad\qquad (4.48)$$

74

Thus, simple expressions for the depth averaged turbulent stresses can be obtained

$$\left\langle \overline{u'^2} \right\rangle \cong 4a\alpha_0^2 u_1^2 \dots\dots\dots(4.49)$$

$$\left\langle \overline{w'^2} \right\rangle \cong 4b\alpha_0^2 u_1^2 \dots\dots\dots(4.50)$$

and

$$\left\langle \overline{u'w'} \right\rangle \cong 4\alpha_0^2 |u_1| u_1 \dots\dots\dots(4.51)$$

Substituting (4.32), (4.49), and (4.50) into (4.29) gives a relation for the jump momentum flux in terms of the excess surface velocity:

$$J = \left(\frac{1}{3} + 4(a-b)\alpha_0^2 \right) h u_1^2 \dots\dots\dots(4.52)$$

To complete the development, a model for the excess surface velocity is required.

4.3.3 Surface Velocity Model

A general equation for u_1, derived from the moment of momentum principle, is provided by Steffler and Jin (1993). Assuming that the vertical turbulence is the only significant effect on the pressure distribution and neglecting the effect of bed stress, the equation reads

$$\frac{\partial u_1}{\partial t} + \frac{\partial u_0 u_1}{\partial x} = \frac{3}{h}\left\langle \overline{w'^2} \right\rangle \frac{\partial h}{\partial x} - \frac{3}{h}\left\langle \overline{u'^2} \right\rangle \frac{\partial h}{\partial x} + \frac{6}{h}\left\langle \overline{u'w'} \right\rangle \dots\dots\dots(4.53)$$

Using the turbulent stress relations (4.49) - (4.51), assuming steady state conditions and that u_1 reaches a maximum near the midpoint of the jump gives

$$u_1 \frac{\partial u_0}{\partial x} = \frac{\alpha_0^2}{h}\left[-24|u_1| + \frac{12}{5}(a-b)u_1\right]u_1 \dots\dots\dots\dots\dots\dots\dots\dots\dots\dots\dots\dots\dots\dots(4.54)$$

Three solutions are possible for u_1. The first is simply $u_1 = 0$. Consideration of (4.53) shows that this solution is stable for $\frac{\partial u_0}{\partial x} > 0$, but unstable for $\frac{\partial u_0}{\partial x} < 0$, which is the jump condition. This equation appears to capture, in general form at least, the significant difference between accelerating and decelerating flows.

Two further roots are also possible; one positive and one negative. There may be some physical justification for a positive root, if it is interpreted as indicating a separated jump or a jump with an undeveloped roller (Hager, 1992). Such jumps seem to occur with fully developed upstream flow conditions. Again, this is consistent with (4.53), since the incoming flow would enter the jump with some positive u_1, which would tend to grow. While qualitatively plausible, quantitative prediction would be unreliable because the flow field is more complex than that of the classical jump and many of the assumptions made would no longer be valid.

The negative root of (4.54) is the one corresponding to the classical jump situation. This solution is

$$u_1 = \frac{h}{\alpha_0^2\left[24 - \frac{12}{5}(a-b)\right]}\frac{\partial u_0}{\partial x} \dots\dots\dots\dots\dots\dots\dots\dots\dots\dots\dots\dots\dots\dots(4.55)$$

It should be noted that the velocity predicted by this equation is a better indication of r . . . rall velocity distribution than it is of the actual surface velocity. In particular, surface velocity estimate will tend to be higher than the actual due to the difference

between the assumed and actual velocity distribution shapes. Substituting (4.55) into (4.52) yields:

$$J = \frac{\left(\frac{1}{3} + 4(a-b)\alpha_0^2\right)}{\alpha_0^4\left[24 - \frac{12}{5}(a-b)\right]^2} h^3\left(\frac{\partial u_0}{\partial x}\right)^2 \quad\text{...(4.56)}$$

The turbulence constants can be collapsed into a single coefficient, K_1, which will be determined from numerical experiments. The jump flux model is then simply

$$J = K_1 h^3\left(\frac{\partial u_0}{\partial x}\right)^2 \quad\text{..(4.57)}$$

The diffusive character of (4.57) is apparent when substituted into the St. Venant momentum equation, (4.28). A second derivative of u_0 term arises which has a negative sign set by the longitudinal gradient of u_0.

Eq. (4.57) is developed to apply near the middle of the jump where J is maximum. As shown in the following section, if (4.57) is used over the entire jump, a value $K_1 = 7.4$ gives good jump lengths but tends to predict an overly smooth, rounded off jump profile. Slightly better results are obtained by a modification which allows K_1 to vary with the square of the water surface slope. While somewhat ad-hoc, this modification is physically reasonable since it reduces the jump flux at the toe and end of the jump. The modified model is

$$J = K_2\left(\frac{\partial h}{\partial x}\right)^2 h^3\left(\frac{\partial u_0}{\partial x}\right)^2 \quad\text{...(4.58)}$$

As is also shown in the following section, $K_2 = 441$ gives good results for both length and profile shape for all jumps considered. The values of the constants appear to be physically reasonable; for example, $a = 4$, $b = 1.5$, and $\alpha_0 = 0.23$ give the above value of K_1. These constants give a reverse surface velocity about 30% larger than measured, but this is expected due to the crude linear velocity profile assumed. The value of K_1 also approximates the average of $441\left(\dfrac{\partial h}{\partial x}\right)^2$ over the length of the jump. Either of the jump flux formulations is highly non-linear and very sensitive to the longitudinal gradients. Included in the general equation, they will have negligible effect except in the vicinity of rapidly varying flows. Care should be taken, however, in regions of rapid acceleration, to set the jump flux to zero. In addition, the sign of J should change with flow direction.

4.4 Numerical Model

To test the proposed jump flux formulations, a Petrov-Galerkin Finite Element numerical formulation is used. The code is based on the Characteristic Dissipative Galerkin (CDG-1D) finite element scheme of Hicks and Steffler (1992). The method reduces to a standard Bubnov-Galerkin without any numerical dissipation when the upwinding parameter is set to zero. Linear interpolation functions for depth and velocity are used. A fully implicit time stepping scheme is used to rapidly solve for the final steady state jump profiles from an arbitrary initial condition. The implicit set of non-linear algebraic equations at each time step is solved by a Newton-Raphson iterative procedure with analytical evaluation of the Jacobian derivatives. In running the model, it was found that some care was necessary while the jump was forming and moving. The Courant Number during this stage is limited to no greater than about five. Once the jump is properly located, however, convergence is very rapid and very large

time steps can be used. For boundary conditions, both depth and velocity are specified at the upstream (supercritical inflow) section and depth is specified at the downstream (subcritical outflow) section.

4.5 Experimental Verification

The experimental data from Gharangik (1988) is selected for calibration and ʾʿcation of the jump flux model. These experiments, also reported in Gharangik and ·y (1991), were performed in a rectangular, horizontal, metal flume 14 m long, ʿı ıı high and 0.46 m wide. Jump profiles for inflow Froude numbers ranging from 2.3 to 7.0 were measured using a point gauge with an accuracy of 0.3 mm. In modeling these experiments, the element length is set to 0.061 m (0.2 ft.) which is one to two times the supercritical flow depth. Manning's n varied from 0.0063 to 0.0077, essentially to properly locate the jump for profile comparison.

Figs. 4.2 to 4.5 show the measured and calculated jump surface profiles for inflow Froude numbers of 2.3, 4.23, 5.74, and 7.0. Results obtained using both jump flux formulations, from (4.57) and (4.58), are shown in these figures. In general, both methods give good estimates of the jump length and overall profile. Underprediction of the downstream depth can be explained by bulking due to air entrainment in the experiments which was not accounted for in the model. In all cases the depths matched well a short distance further downstream. The values of the constants in the computational models give very close results for the intermediate Froude numbers. The simple model however, gives a slightly shorter jump at the high Froude number and a slightly longer jump at the low Froude number. The modified model gives uniformly close jump lengths for all Froude numbers. The modified model also shows a somewhat sharper transition at the toe of the jump.

Figs. 4.6 and 4.7 show the effect of spatial discretization on the computed results for the modified me 'el. For the CDG scheme (upwinding parameter = 0.25), the overa le is not significantly affected until the element size exceeds the downstream depth. The location of the jump toe shifts to the nearest node and the profile becomes very sharply varied. Further increasing the element length past the jump length gives some oscillations with a slight overshoot at the end of the jump. The Bubnov-Galerkin scheme (upwinding parameter = 0) is more sensitive to the discretization. The finest discretization (about one tenth of the downstream depth) gives very good results with very small oscillations downstream of the jump. As the discretization becomes coarser, these oscillations become stronger and the jump location shifts upstream. At the coarsest discretization, oscillations upstream of the jump become evident. The solution within the jump remains very consistent, albeit shifted in position. This is consistent with the modified jump flux model which dramatically reduces the flux at the beginning and end of the jump. The unmodified model (not show n) displayed significantly less difference in profile between the dissipative and non-dissipative schemes.

The proposed jump model does not, in general, obviate the need for artificial dissipation mechanisms. Depending on the resolution desired by the modeler, the jump model may or may not be effective. combining both a jump model and artificial dissipation would work well as long as it was understood that accurate jump lengths would only be obtained for sufficiently fine discretizations.

A profile of the total specific force along the channel computed using the modified jump flux model for the 7.0 Froude number jump is shown in Fig. 4.8. The St. Venant line includes the momentum flux based on the depth averaged velocity (i.e. $\beta = 1$) and the pressure force. The jump flux is therefore the difference between the total and the S. Venant lines. The slight oscillation in the total line is attributable to

numerical error in evaluating the jump flux from the nodal values of the variables. Inter element fluxes are automatically conserved by the finite element formulation used. The magnitude and distribution of the jump flux is approximately as indicated by the initial order of magnitude estimate. Away from the jump, the jump flux is entirely negligible, despite being included in the calculation.

4.6 Conclusions

In this study, a new method for simulating hydraulic jumps in depth averaged computations is developed and presented. The model is physically based, using a simplified algebraic stress turbulence closure and a moment of longitudinal momentum equation for estimating the vertical distribution of longitudinal velocity. The model takes the form of a jump momentum flux term which may be added to the usual St. Venant momentum equation. The model is based on conditions at the middle of the jump but is easily modified to apply over the full jump length. A single constant, of physically reasonable magnitude, is adequate to simulate all measured jumps. The jump flux term can be used as a shock-capturing mechanism, since it becomes active only in the presence of a jump and is entirely negligible elsewhere.

In developing this model, some interesting insights into the behavior of the fluid flow within the jump have been gained. First, half or more of the total specific force within the jump is carried by the difference in depth averaged turbulent normal stresses and non-uniform momentum flux. Second, a flow instability, with a classical or separated solution, is indicated by the velocity distribution analysis. As is observed, small differences in inflow conditions may change the jump conditions. Third, rough estimates of the relative magnitudes of the turbulent stresses and mixing length have been obtained from the condition that the jump flux constant give the measured jump

length. These estimates await detailed turbulence measurements for independent verification.

The proposed jump model is incorporated into a finite element model for illustration and verification, but may be used with any conservative numerical scheme. Since the term becomes active only at jump length scales, it does not remove the need for dissipative mechanisms in general models where the spatial discretization used may be significantly larger. The jump flux model is easily adapted to two-dimensional models as well. It may also be used as a first estimate for moving surges, and jumps on slopes and may also be adapted to arbitrary channel sections. Further research and verification in these areas are warranted, however.

References

Abbott, M. B., Marshall, G., and Rodenhius, G. S. (1969). "Amplitude-Dissipative and Phase-Dissipative Scheme for Hydraulic Jump Simulation." 13th Congress IAHR, Tokyo, Japan, Vol. 1, 313-329.

ASCE Task Committee on Turbulence Models in Hydraulic Computations (1988). "Turbulence Modeling of Surface Water Flow and Transport: Part II." J. Hydr. Engrg., ASCE, 114(9), 992-1014.

Garcia-Navarro, P., Priestley, A., and Alcrudo, F. (1994). "An Implicit Method For Water Flow Modeling in Channels and Pipes." J. Hydr. Res., IAHR, Vol. 32, No. 5, 721-742.

Gharangik, A. M. (1988). "Numerical Simulation of Hydraulic Jump." Thesis presented to Washington State University, at Pullman, Wash., in partial fulfillment of the requirements for the degree of Master of Science.

Gharangik, A. M., and Chaudhry, M. H. (1991). "Numerical Simulation of Hydraulic Jump." J. Hydr. Engrg., ASCE, 117(9), 1195-1211.

Hager, W.H. (1992). "Energy Dissipators and Hydraulic Jump." Kluwer Academic Publishers, Dordrecht, The Netherlands.

Hicks, F. E., and Steffler, P. M. (1992). "Characteristic Dissipative Galerkin Scheme for Open-Channel Flow." J. Hydr. Engrg., ASCE, 118(2), 337-352.

Jha, A. K., Akiyama, J., and Ura, M. (1994). "Modeling Unsteady Open-Channel Flows - Modification to Beam and Warming Scheme." J. Hydr. Engrg., ASCE, 120(4), 461-476.

Katopodes, N. D. (1984). "A Dissipative Galerkin Scheme for Open-Channel Flow." J. Hydr. Engrg., ASCE, 118(2), 337-352.

Leutheusser, H. J., and Kartha, V. C. (1972). "Effects of Inflow Conditions on Hydraulic Jump." J. Hydr. Div., ASCE, 98(8), 1367-1385.

Madsen, P. A., and Svendsen, I. A. (1983). "Turbulent Bores and Hydraulic Jumps." J. Fluid Mech., Vol. 129, 1-25.

McCorquodale, J. A., and Khalifa, A. (1983). "Internal Flow in Hydraulic Jumps." J. Hydr. Engrg., ASCE, 109(5), 684-701.

Narayanan, R. (1975). "Wall Jet Analogy to Hydraulic Jump." J. Hydr. Div., ASCE, 101(3), 347-359.

Resch, F. J., and Leutheusser, H J. (1972). "Reynolds Stress Measurements in Hydraulic jumps." J. of Hydr. Res., IAHR, Vol. 10, No. 4, 409-429.

Rouse, H., Siao T. T., and Nagaratnam, S. (1958). "Turbulence Characteristics of the Hydraulic Jump." J. Hydr. Div., ASCE, 84(1), 1528-1-1528-30.

Steffler, P. M., and Jin, Y. (1993). "Depth Averaged and Moment Equations for Moderately Shallow Free Surface Flow." J. of Hydr. Res., IAHR, Vol. 31, No. 1, 5-17.

Younus M., and Chaudhry, M. (1994). "A Depth Averaged $k-\varepsilon$ Model for the Computation of Free Surface Flow." J. of Hydr. Res., IAHR, Vol. 32, No. 3, 415-444.
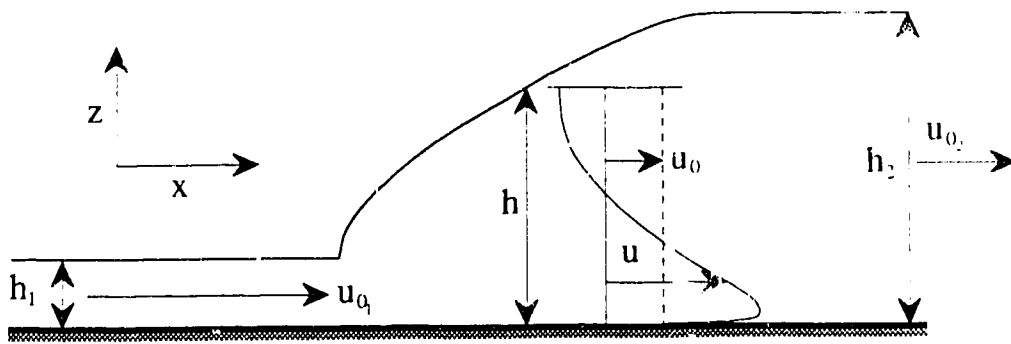
FIG. 4.1. Definition Sketch for a Hydraulic Jump
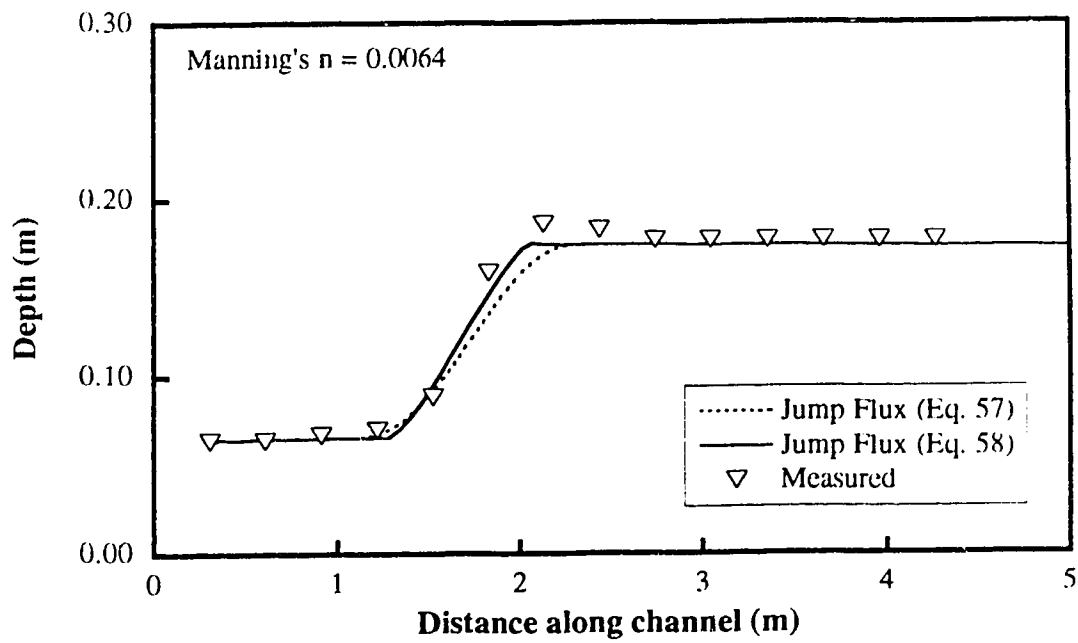
FIG. 4.2. Surface Profiles for F = 2.30
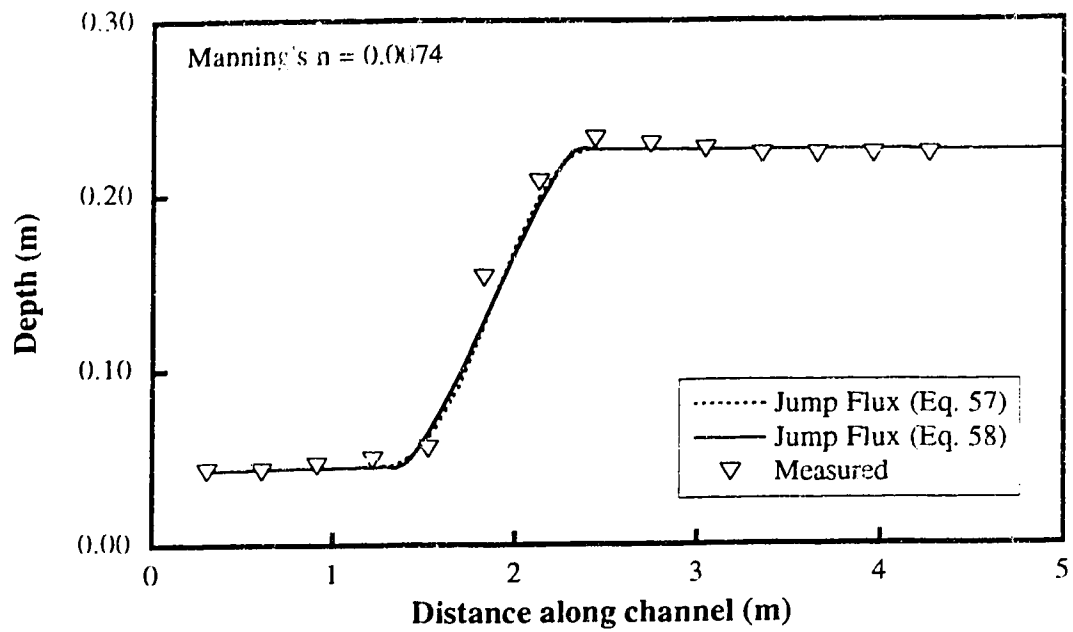
FIG. 4.3. Surface Profiles for F = 4.23
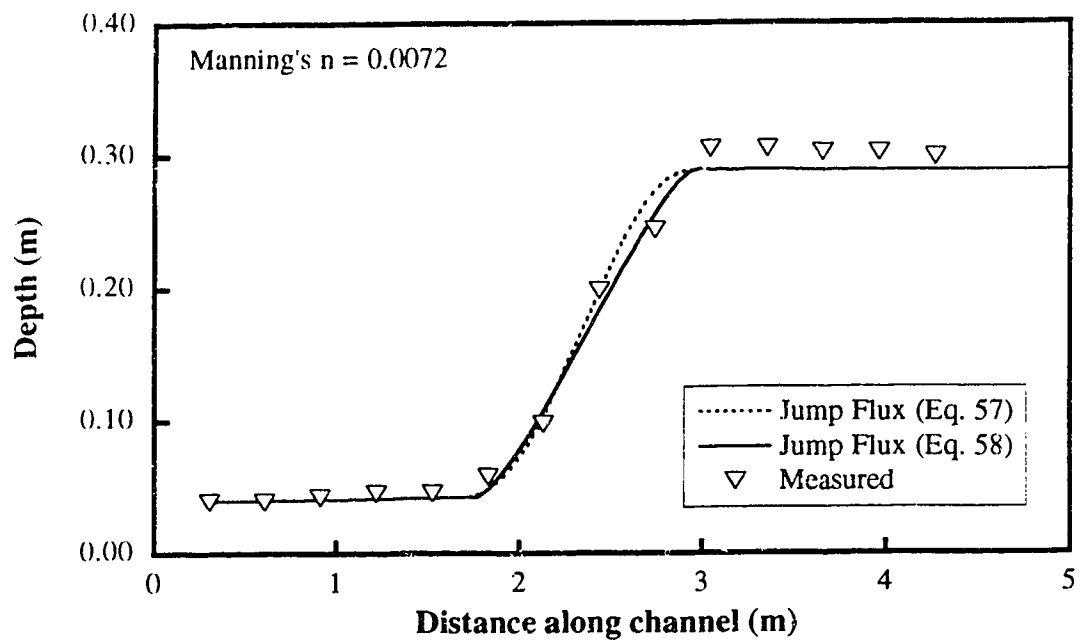
FIG. 4.4. Surface Profiles for F = 5.74

86
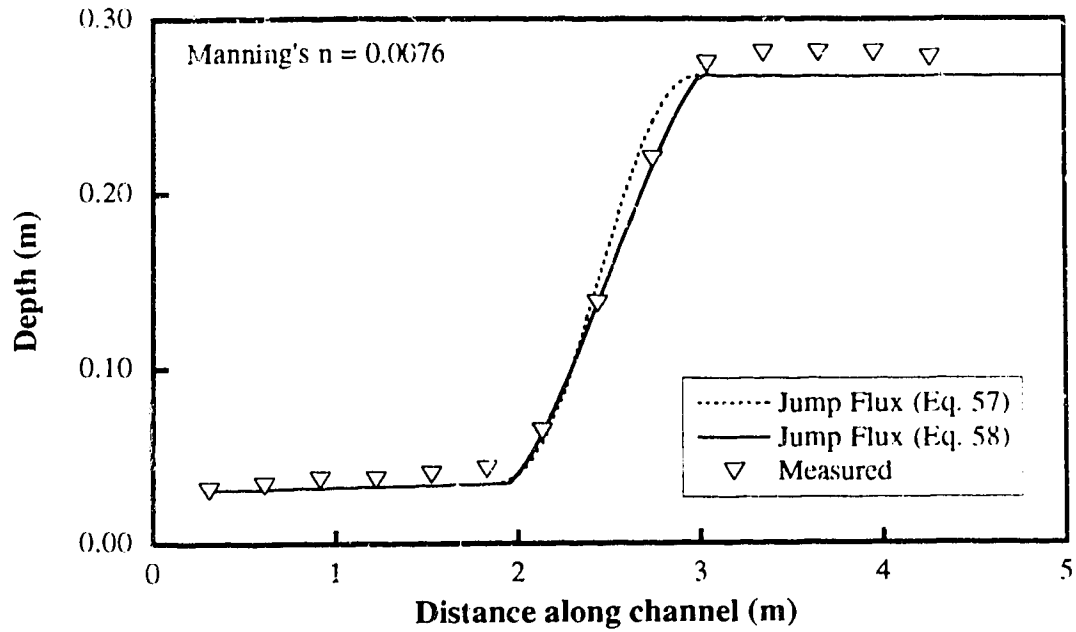
FIG. 4.5. Surface Profiles for F = 7.0
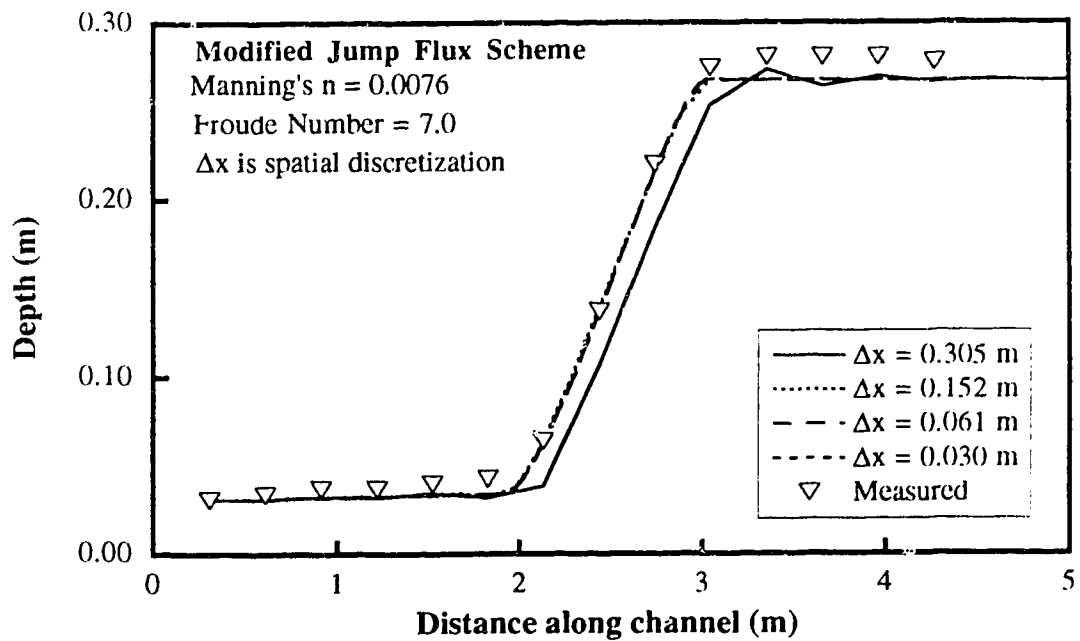
FIG. 4.6. Variation of Spatial Discretization (CDG Scheme)
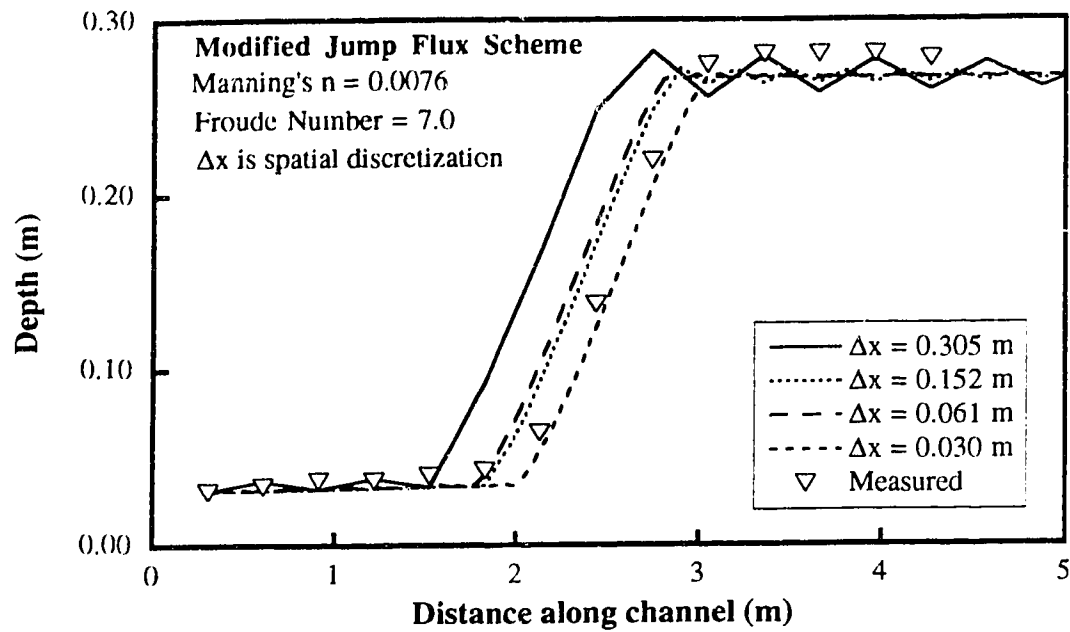
FIG. 4.7. Variation of Spatial Discretization (B-G Scheme)
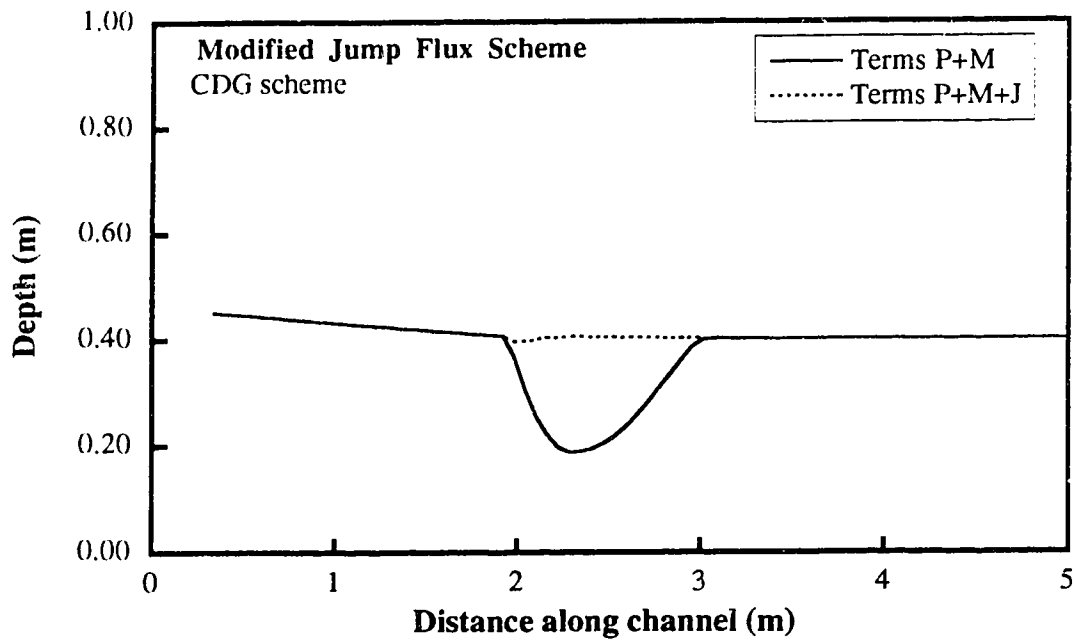
FIG. 4.8. Longitudinal Momentum Balance (F = 7.0)

Chapter 5

Summary and Conclusions

In this study the vertically averaged and moment (VAM) equations, which assume a linear longitudinal velocity distribution and quadratic pressure and vertical velocity distributions, were investigated for modeling rapidly varied open channel flows. These equations, by incorporating higher degree of vertical detail, provide a better representation of the flow when compared to the St. Venant and Boussinesq equations. The vertical details incorporated allow for utilizing near bed velocity for the bed shear stress and a turbulence closure model for evaluating turbulent stresses. Also, these equations have the advantages of depth averaged models and can easily be extended to account for lateral variations.

The VAM and VA (similar to the Boussinesq equations) equations were solved numerically using a hybrid Petrov-Galerkin and Bubnov-Galerkin finite element

scheme, while the modified St. Venant equations were modeled using the Petrov-Galerkin finite element scheme.

As a first application, the VAM equations were applied to flow over curved beds and the results were compared to the vertically averaged (VA) equations as well as to the measured data. Three tests for flow over curved beds consisting of flow from a horizontal to a steep slope (up to 60 degree) with a circular transition, flow over symmetric and asymmetric bed profiles and flow over an idealized flip-bucket spillway were conducted. In each case the simulated results from VAM and VA equations of bed pressure and water surface profile were compared with the measured data. The VAM equations showed excellent agreement with the measured data for both water surface and bed pressure profiles. The VA equations started to deviate from the measured data for large flows and bed and water surface curvatures. The satisfactory performance of the VAM equations may be attributed to a higher degree of vertical detail incorporated into the model.

Next, the VAM equations were applied to model rectangular free overfalls with smooth and rough beds and to sharp crested weirs with sloping upstream face. To model the free jet downstream of the overfall or weir, the VAM equations were used to determine the lower nappe profile of the free jet while the bed pressure was forced to atmospheric. At the boundary of the free jet and fixed bed, internal boundary conditions of zero bed pressure and fixed bed elevation were specified.

For rectangular free overfalls with smooth and rough beds, the simulated results, both for water surface elevation upstream of the overfall and the free jet trajectory, were in excellent agreement with the measured results. For a smooth horizontal rectangular free overfalls, the computed vertical velocity and pressure distributions at the brink and upstream of the overfall were compared with the measured data. The computed results for vertical velocity, although slightly lower,

90

were generally in good agreement with the measured data. The computed pressure distributions upstream of the brink agreed well with the measured data, while at the brink the maximum pressure was modeled accurately but the measured pressure distribution could not be modeled accurately by the assumed quadratic pressure distribution. The computed longitudinal velocity profiles, although crude, agreed well with a two-dimensional potential model.

For weirs with upstream slope of 4:1 and 2:1, the VAM equations performed satisfactorily in modeling the flow. However, for weirs with upstream slope of 45 degree, although the free jet trajectory was modeled accurately, the water surface profiles upstream of the weir showed numerical instability for larger weir heights. This numerical instability was believed to be the combined effects of flow rate, internal boundary conditions and larger weir height.

Finally, a new method to simulate hydraulic jumps using the depth averaged St. Venant equations was developed. Using the moment of longitudinal momentum equation for estimating the vertical distribution of longitudinal velocity and a simplified algebraic stress closure model for turbulent normal and shear stresses, a new term known as the jump momentum flux was added to the St. Venant equations. A single constant, of physically reasonable magnitude, was sufficient to model accurately both the position and length of the jump for Froude numbers of 2.3 to 7.0. However, the jump flux term does not eliminate the need for a dissipative mechanism in the numerical model. For the modified St. Venant equations, using the Characteristic Dissipative Galerkin finite element scheme, the jump length was found to be independent of the spatial discretization. As the jump flux term becomes active only in the presence of the jump and is negligible elsewhere, it can be used for shock capturing, moving surges and jumps on slopes.

The present study demonstrates the successful application of the VAM equations for rapidly varied open channel flow and provides an alternative in terms of depth averaged modeling. A natural extension of the present model would be to incorporate a turbulent closure model and apply these equations to moving surges and other expanding flows. The present model could be used for movable beds, where the ability to predict non-uniform bed shear stress may be of vital importance. Also, for fish habitats studies, the present model can be used for the prediction of approximate near bed velocity. Finally, the present one-dimensional equations could further be developed to take into account the lateral variations.

Appendix A

Model Development

The vertically averaged and moment (VAM) equations are modeled using a hybrid Petrov-Galerkin and Bubnov-Galerkin scheme. In this section, details of the numerical model applied are presented. The modeled VAM equations are:

$$\frac{\partial h}{\partial t} + \frac{\partial q}{\partial x} = 0 \quad\text{...(A.1)}$$

$$\frac{\partial q}{\partial t} + \frac{\partial}{\partial x}\left[\frac{q^2}{h} + \frac{gh^2}{2} + \frac{hu_1^2}{3} + \frac{hp_1}{2\rho} + \frac{2hp_2}{3\rho} - \frac{h\bar{\bar{\sigma}}_x}{\rho}\right] + gh\frac{\partial z_b}{\partial x} + \frac{p_1}{\rho}\frac{\partial z_b}{\partial x} + \frac{\tau_b}{\rho} = 0 \quad\text{............(A.2)}$$

$$\frac{\partial u_1}{\partial t} + \frac{\partial}{\partial x}\left(\frac{qu_1}{h}\right) - \frac{1}{2\rho}\left(\frac{\partial p_1}{\partial x} - \frac{p_1}{h}\frac{\partial h}{\partial x}\right) + \frac{4\hat{p}_2}{h\rho}\frac{\partial \bar{z}}{\partial x} - \frac{6}{h\rho}\left(\frac{\tau_b}{2} + \bar{\sigma}_x\frac{\partial \bar{z}}{\partial x} - \bar{\tau}_{xz}\right) = 0 \quad\text{............(A.3)}$$

93

$$w_b = \left(\frac{q}{h} - u_1\right)\frac{\partial z_b}{\partial x} \dotfill (A.4)$$

$$w_h = \frac{\partial h}{\partial t} + \left(\frac{q}{h} + u_1\right)\frac{\partial(z_b + h)}{\partial x} \dotfill (A.5)$$

$$\frac{1}{4}\frac{\partial h^2}{\partial t} + q\frac{\partial \bar{z}}{\partial x} + \frac{1}{6}\frac{\partial h^2 u_1}{\partial x} - h\overline{w} = 0 \dotfill (A.6)$$

$$\frac{\partial h\overline{w}}{\partial t} + \frac{\partial q\overline{w}}{\partial x} - \frac{1}{6}\frac{\partial}{\partial x}\left[hu_1(w_b - w_h)\right] - \frac{1}{\rho}\frac{\partial h\overline{\tau}_{zx}}{\partial x} + \frac{\tau_b}{\rho}\frac{\partial z_b}{\partial x} - \frac{p_1}{\rho} = 0 \dotfill (A.7)$$

$$\frac{\overline{w}}{4}\frac{\partial h^2}{\partial t} - \frac{\partial}{\partial t}\left[\frac{h^2}{12}(w_b - w_h)\right] + \left[q\overline{w} - \frac{hu_1}{6}(w_b - w_h)\right]\frac{\partial \bar{z}}{\partial x} - \frac{\partial}{\partial x}\left[\frac{hq}{12}(w_b - w_h)\right]$$

$$+ \frac{\partial}{\partial x}\left[\frac{h^2 u_1}{10}\left(\overline{w} + \frac{w_b}{3} + \frac{w_h}{3}\right)\right] - h\overline{w'^2} - \frac{h}{\rho}\left(\overline{\tau}_{xz}\frac{\partial \bar{z}}{\partial x} - \overline{\sigma}_z\right) - \frac{h\tau_b}{2\rho}\frac{\partial z_b}{\partial x} - \frac{2}{3\rho}hp_2 = 0 \dotfill (A.8)$$

where

$$\bar{z} = z_b + \frac{h}{2} \dotfill (A.9)$$

$$\frac{\tau_b}{\rho} = \frac{q^2}{h^2 C_*^2} \dotfill (A.10)$$

$$\overline{w'^2} = \overline{w}^2 + \frac{w_b^2}{12} + \frac{w_h^2}{12} - \frac{w_b w_h}{6} + \frac{1}{20}\left(2\overline{w} - w_b - w_h\right)^2 \dotfill (A.11)$$

94

The above equations are obtained using the following assumed longitudinal velocity, vertical velocity and pressure distributions

$$u \approx u_0 + u_1(2\eta - 1) \dotfill \text{(A.12)}$$

$$w \approx w_b(1 - \eta) + w_2 4\eta(1 - \eta) + w_h\eta \dotfill \text{(A.13)}$$

$$p \approx (\rho g h + p_1)(1 - \eta) + p_2 4\eta(1 - \eta) \dotfill \text{(A.14)}$$

The above particular choice of a linear longitudinal velocity distribution and quadratic vertical velocity and pressure distributions result in a system of equations, where moment of continuity, longitudinal momentum and vertical momentum equations can be used respectively for evaluation of averaged vertical velocity, longitudinal velocity at the surface in excess of the mean and mid-depth pressure in excess of the average pressure at the bed and surface. All the parameters of the above distributions are perturbations to the assumed distributions for the St. Venant and Boussinesq equations. Thus the above system of equations can easily be reduced to the St. Venant or Boussinesq equations by forcing the appropriate perturbations to zero and eliminating the corresponding equations.

The first eight equations represent a closed system, where (A.1) to (A.8) are used to respectively evaluate h, q, u_1, w_b, w_h, $\overline{w}$, p_1, and p_2. The vector Φ, $(\Phi_l, l = 1,8)$, represents the above eight variables, where $\Phi_1 = h$ and $\Phi_8 = p_2$.

The above system of equations, following the method described in Celia and Gray (1992), is found to be parabolic. However, the last five equations are mostly reactive type of equations, that is, the dependent variable being evaluated from each of these equations do not involve the temporal or spatial derivative of that variable. Also,

preliminary test conducted with the Bubnov-Galerkin finite element scheme showed that some form of artificial dissipative mechanism was needed for solving these equations without spurious oscillations. Thus, the first three equations are used to find an equivalent Characteristic Dissipative Galerkin (CDG) finite element scheme introduced by Hicks and Steffler (1992) for solving the St. Venant equations. This scheme has the advantage of providing selective artificial dissipation for shock capturing and modeling both progressive and regressive waves accurately.

Neglecting w_b, w_h, $\overline{w}$, p_1, and p_2, and considering only the conservative term (A.1) to (A.3) can be written as:

$$\frac{\partial h}{\partial t} + \frac{\partial h u_0}{\partial x} = 0 \quad\text{...(A.15)}$$

$$\frac{\partial h u_0}{\partial t} + \frac{\partial}{\partial x}\left[h u_0^2 + \frac{g h^2}{2} + \frac{h u_1^2}{3} \right] = 0 \quad\text{..(A.16)}$$

$$\frac{\partial u_1}{\partial t} + \frac{\partial u_0 u_1}{\partial x} = 0 \quad\text{...(A.17)}$$

where $u_0 = q / h$. The advection matrix for the above set of equations can be written as:

$$\mathbf{A} = \begin{bmatrix} 0 & 1 & 0 \\ -u_0 + u_1^2 + gh & 2u_0 & \frac{2}{3}hu_1 \\ -\frac{u_0 u_1}{h} & \frac{u_1}{h} & u_0 \end{bmatrix} \quad\text{...(A.18)}$$

where bold letters represent vectors and matrices. For the above advection matrix, the eigen values and eigen vectors in column are:

$$\Lambda = \begin{bmatrix} u_0 + c & 0 & 0 \\ 0 & u_0 - c & 0 \\ 0 & 0 & u_0 \end{bmatrix} \quad\quad\quad\quad\quad\quad\quad\quad\quad\quad\quad (A.19)$$

$$M = \begin{bmatrix} 1 & 1 & 1 \\ u_0 + c & u_0 - c & u_0 \\ \dfrac{u_1}{h} & \dfrac{u_1}{h} & \dfrac{2u_1^2 - 3c^2}{2hu_1} \end{bmatrix} \quad\quad\quad\quad\quad\quad\quad (A.20)$$

where $c = \sqrt{u_1^2 + gh}$. The advection matrix can also be written as

$$[A] = [M][\Lambda][M]^{-1} \quad\quad\quad\quad\quad\quad\quad\quad\quad\quad\quad\quad (A.21)$$

The upwinding matrix, as described by Hicks and Steffler (1992), is given by

$$W = [M] \begin{bmatrix} \dfrac{u_0 + c}{|u_0 + c|} & 0 & 0 \\ 0 & \dfrac{u_0 - c}{|u_0 - c|} & 0 \\ 0 & 0 & \dfrac{u_0}{|u_0|} \end{bmatrix} [M]^{-1} \quad\quad\quad\quad\quad (A.22)$$

The elements of the upwinding matrix are:

$$W_{11} = \frac{1}{3c^2}\left[-\left(u_1^2 - \frac{3}{2}c^2 \right)(\lambda_1 + \lambda_2) - \frac{3}{2}u_0 c(\lambda_1 - \lambda_2) + 2u_1^2 \lambda_3 \right] \quad\quad (A.23)$$

$$W_{12} = \frac{1}{2c}(\lambda_1 - \lambda_2) \quad\quad\quad\quad\quad\quad\quad\quad\quad\quad\quad\quad (A.24)$$

$$W_{13} = \frac{hu_1}{3c^2}\left(\lambda_1 + \lambda_2 - 2\lambda_3\right) \quad \text{...(A.25)}$$

$$W_{21} = \frac{1}{3c^3}\left[\left(u_0^2 - c^2\right)\left(u_1^2 - \frac{3}{2}c^2\right)\left(\lambda_1 - \lambda_2\right)\right]$$

$$+ \frac{u_0 u_1^2}{3c^3}\left[-\left(u_0 + c\right)\lambda_1 + \left(u_0 - c\right)\lambda_2 + 2c\lambda_3\right] \quad \text{...................................(A.26)}$$

$$W_{22} = \frac{1}{2c}\left[\left(u_0 + c\right)\lambda_1 - \left(u_0 - c\right)\lambda_2\right] \quad \text{...(A.27)}$$

$$W_{23} = \frac{hu_1}{3c^2}\left[\left(u_0 + c\right)\lambda_1 + \left(u_0 - c\right)\lambda_2 - 2u_0\lambda_3\right] \quad \text{..(A.28)}$$

$$W_{31} = \frac{u_1}{3hc^2}\left[-\left(u_1^2 - \frac{3}{2}c^2\right)\left(\lambda_1 + \lambda_2 - 2\lambda_3\right) - \frac{3}{2}u_0 c\left(\lambda_1 - \lambda_2\right)\right] \quad \text{..............................(A.29)}$$

$$W_{32} = \frac{u_1}{2hc}\left(\lambda_1 - \lambda_2\right) \quad \text{...(A.30)}$$

$$W_{33} = \frac{u_1^2}{3c^2}\left(\lambda_1 + \lambda_2 - 2\lambda_3\right) + \lambda_3 \quad \text{..(A.31)}$$

where λ_1, λ_2 and λ_3 are given by:

$$\lambda_1 = \frac{u_0 + c}{\left|u_0 + c\right|} \quad \text{..(A.32)}$$

$$\lambda_2 = \frac{u_0 - c}{\left|u_0 - c\right|} \quad \text{..(A.33)}$$

$$\lambda_3 = \frac{u_0}{|u_0|} \quad\text{..(A.34)}$$

Setting u_1 to zero in the advection matrix leads to an approximate upwinding matrix which is given by

$$W_{11} = \frac{1}{2}(\lambda_1 + \lambda_2) - \frac{u_0}{2c}(\lambda_1 - \lambda_2) \quad\text{...(A.35)}$$

$$W_{12} = \frac{1}{2c}(\lambda_1 - \lambda_2) \quad\text{..(A.36)}$$

$$W_{21} = -\frac{1}{2c}\left(u_0^2 - c^2\right)(\lambda_1 - \lambda_2) \quad\text{..(A.37)}$$

$$W_{22} = \frac{1}{2c}\left[(u_0 + c)\lambda_1 - (u_0 - c)\lambda_2\right] \quad\text{..............................(A.38)}$$

$$W_{33} = \lambda_3 \quad\text{...(A.39)}$$

where $c = \sqrt{gh}$, and the rest of the elements of the approximate upwinding matrix are zero. For the VAM equations, the first three equations are solved using the CDG scheme with both the approximate and the full upwinding matrix, while the rest of the equations are modeled using Bubnov-Galerkin scheme.

The application of the CDG scheme to the first three equations produce the following equations:

$$\int_0^L \left[f_i \frac{\partial \hat{h}}{\partial t} - \frac{df_i}{dx}\hat{q} + \frac{\omega\Delta x}{2}\frac{df_i}{dx}\left(\begin{array}{l} \hat{W}_{11}\dfrac{\partial \hat{h}}{\partial t} + \hat{W}_{12}\dfrac{\partial \hat{q}}{\partial t} + \hat{W}_{13}\dfrac{\partial \hat{u}_1}{\partial t} \\[2mm] +\hat{W}_{11}\hat{E}_1 + \hat{W}_{12}\hat{E}_2 + \hat{W}_{13}\hat{E}_3 \end{array}\right)\right]dx + \left[f_i\hat{q}\right]_0^L = 0 \quad\text{............(A.40)}$$

$$\int_0^L \left[\begin{array}{l} f_i\dfrac{\partial \hat{q}}{\partial t} - \dfrac{df_i}{dx}\left(\dfrac{\hat{q}^2}{\hat{h}} + \dfrac{g\hat{h}^2}{2} + \dfrac{\hat{h}\hat{u}_1^2}{3} + \dfrac{\hat{h}\hat{p}_1}{2\rho} + \dfrac{2\hat{h}\hat{p}_2}{3\rho} - \dfrac{\hat{h}\hat{\sigma}_x}{\rho}\right) + f_i\left(g\hat{h}\dfrac{\partial z_b}{\partial x} + \dfrac{\hat{p}_1}{\rho}\dfrac{\partial z_b}{\partial x} + \dfrac{\hat{\tau}_b}{\rho}\right) \\[3mm] +\dfrac{\omega\Delta x}{2}\dfrac{df_i}{dx}\left(\hat{W}_{21}\dfrac{\partial \hat{h}}{\partial t} + \hat{W}_{22}\dfrac{\partial \hat{q}}{\partial t} + \hat{W}_{23}\dfrac{\partial \hat{u}_1}{\partial t} + \hat{W}_{21}\hat{E}_1 + \hat{W}_{22}\hat{E}_2 + \hat{W}_{23}\hat{E}_3\right) \end{array}\right]dx$$

$$+\left[f_i\left(\frac{\hat{q}^2}{\hat{h}} + \frac{g\hat{h}^2}{2} + \frac{\hat{h}\hat{u}_1^2}{3} + \frac{\hat{h}\hat{p}_1}{2\rho} + \frac{2\hat{h}\hat{p}_2}{3\rho} - \frac{\hat{h}\hat{\sigma}_x}{\rho}\right)\right]_0^L = 0 \quad\text{..............................(A.41)}$$

$$\int_0^L \left[\begin{array}{l} f_i\dfrac{\partial \hat{u}_1}{\partial t} - \dfrac{df_i}{dx}\left(\dfrac{\hat{q}\hat{u}_1}{\hat{h}}\right) + f_i\left\{-\dfrac{1}{2\rho}\left(\dfrac{\partial \hat{p}_1}{\partial x} - \dfrac{\hat{p}_1}{\hat{h}}\dfrac{\partial \hat{h}}{\partial x}\right) + \dfrac{4\hat{p}_2}{\hat{h}\rho}\dfrac{\partial \hat{z}}{\partial x} - \dfrac{6}{\hat{h}\rho}\left(\dfrac{\hat{\tau}_b}{2} + \hat{\sigma}_x\dfrac{\partial \hat{z}}{\partial x} - \hat{\tau}_{xz}\right)\right\} \\[3mm] +\dfrac{\omega\Delta x}{2}\dfrac{df_i}{dx}\left(\hat{W}_{31}\dfrac{\partial \hat{h}}{\partial t} + \hat{W}_{32}\dfrac{\partial \hat{q}}{\partial t} + \hat{W}_{33}\dfrac{\partial \hat{u}_1}{\partial t} + \hat{W}_{31}\hat{E}_1 + \hat{W}_{32}\hat{E}_2 + \hat{W}_{33}\hat{E}_3\right) \end{array}\right]dx$$

$$+\left[f_i\left(\frac{\hat{q}\hat{u}_1}{\hat{h}}\right)\right]_0^L = 0 \quad\text{..(A.42)}$$

while application of the Bubnov-Galerkin scheme to the rest of the equations results in the equations below:

$$\int_0^L f_i\left[\hat{w}_b - \left(\frac{\hat{q}}{\hat{h}} - \hat{u}_1\right)\frac{\partial z_b}{\partial x}\right]dx = 0 \quad\text{..(A.43)}$$

$$\int_0^L f_i\left[\hat{w}_h - \frac{\partial \hat{h}}{\partial t} - \left(\frac{\hat{q}}{\hat{h}} + \hat{u}_1\right)\frac{\partial\left(z_b + \hat{h}\right)}{\partial x}\right]dx = 0 \quad\text{..(A.44)}$$

$$\int_0^L f_i\left[\frac{1}{4}\frac{\partial \hat{h}^2}{\partial t} + \hat{q}\frac{\partial \hat{\bar{z}}}{\partial x} + \frac{1}{6}\frac{\partial \hat{h}^2\hat{u}_1}{\partial x} - \hat{h}\hat{\bar{w}}\right]dx = 0 \quad\text{..(A.45)}$$

$$\int_0^L\left[f_i\left\{\frac{\partial \hat{h}\hat{\bar{w}}}{\partial t} + \frac{\partial \hat{q}\hat{\bar{w}}}{\partial x} - \frac{1}{6}\frac{\partial}{\partial x}\left[\hat{h}\hat{u}_1(\hat{w}_b - \hat{w}_h)\right] + \frac{\hat{\tau}_b}{\rho}\frac{\partial z_b}{\partial x} - \frac{\hat{p}_1}{\rho}\right\} + \frac{df_i}{dx}\left(\frac{\hat{h}\hat{\tau}_{zx}}{\rho}\right)\right]dx$$

$$-\left[f_i\left(\frac{\hat{h}\hat{\tau}_{zx}}{\rho}\right)\right]_0^L = 0 \quad\text{..(A.46)}$$

$$\int_0^L f_i\left[\begin{array}{l}\dfrac{\hat{\bar{w}}}{4}\dfrac{\partial \hat{h}^2}{\partial t} - \dfrac{\partial}{\partial t}\left\{\dfrac{\hat{h}^2}{12}(\hat{w}_b - \hat{w}_h)\right\} + \left\{\hat{q}\hat{\bar{w}} - \dfrac{\hat{h}\hat{u}_1}{6}(\hat{w}_b - \hat{w}_h)\right\}\dfrac{\partial \hat{\bar{z}}}{\partial x} \\[3mm] -\dfrac{\partial}{\partial x}\left\{\dfrac{\hat{h}\hat{q}}{12}(\hat{w}_b - \hat{w}_h)\right\} + \dfrac{\partial}{\partial x}\left\{\dfrac{\hat{h}^2\hat{u}_1}{10}\left(\hat{\bar{w}} + \dfrac{\hat{w}_b}{3} + \dfrac{\hat{w}_h}{3}\right)\right\} - \hat{h}\overline{\hat{w}^2} \\[3mm] -\dfrac{\hat{h}}{\rho}\left(\hat{\bar{\tau}}_{xz}\dfrac{\partial \hat{\bar{z}}}{\partial x} - \hat{\bar{\sigma}}_z\right) - \dfrac{\hat{h}\hat{\tau}_b}{2\rho}\dfrac{\partial z_b}{\partial x} - \dfrac{2}{3\rho}\hat{h}\hat{p}_2\end{array}\right]dx = 0 \quad\text{..................(A.47)}$$

where f_i is a part of the test function, Δx is the spatial discretization, and L represents the length of domain. The new variables (with hat) are defined as follows

$$\hat{\Phi} = \Phi_j f_j \quad\text{..(A.48)}$$

where f_j are the basis functions and Φ_j are the nodal values of the unknowns. $\hat{E}_1$, $\hat{E}_2$ and $\hat{E}_3$ represent respectively the left hand side of (A.1), (A.2) and (A.3), in terms of the new variables, without the temporal derivatives.

In the present study the internal turbulent stresses are neglected and will not be considered from this point onward. The above equations, (A.37) to (A.44) are split into two parts, one containing the temporal derivatives only and the other containing the rest of the equation. The temporal derivative part, wherein the time derivatives are discretized using finite difference scheme, are respectively given by:

$$S_1 = \int_e \left[\begin{array}{l} \left[\left\{ f_i + \theta\alpha\hat{W}_{11}^{n+1} + (1-\theta)\alpha\hat{W}_{11}^n \right\}\left(\hat{h}^{n+1} - \hat{h}^n\right) \right] \\ +\left\{ \theta\alpha\hat{W}_{12}^{n+1} + (1-\theta)\alpha\hat{W}_{12}^n \right\}\left(\hat{q}^{n+1} - \hat{q}^n\right) \\ +\left\{ \theta\alpha\hat{W}_{13}^{n+1} + (1-\theta)\alpha\hat{W}_{13}^n \right\}\left(\hat{u}_1^{n+1} - \hat{u}_1^n\right) \end{array} \right] dx \quad\text{............(A.49)}$$

$$S_2 = \int_e \left[\begin{array}{l} \left[\left\{ \theta\alpha\hat{W}_{21}^{n+1} + (1-\theta)\alpha\hat{W}_{21}^n \right\}\left(\hat{h}^{n+1} - \hat{h}^n\right) \right] \\ +\left\{ f_i + \theta\alpha\hat{W}_{22}^{n+1} + (1-\theta)\alpha\hat{W}_{22}^n \right\}\left(\hat{q}^{n+1} - \hat{q}^n\right) \\ +\left\{ \theta\alpha\hat{W}_{23}^{n+1} + (1-\theta)\alpha\hat{W}_{23}^n \right\}\left(\hat{u}_1^{n+1} - \hat{u}_1^n\right) \end{array} \right] dx \quad\text{............(A.50)}$$

$$S_3 = \int_e \left[\begin{array}{l} \left[\left\{ \theta\alpha\hat{W}_{31}^{n+1} + (1-\theta)\alpha\hat{W}_{31}^n \right\}\left(\hat{h}^{n+1} - \hat{h}^n\right) \right] \\ +\left\{ \theta\alpha\hat{W}_{32}^{n+1} + (1-\theta)\alpha\hat{W}_{32}^n \right\}\left(\hat{q}^{n+1} - \hat{q}^n\right) \\ +\left\{ f_i + \theta\alpha\hat{W}_{33}^{n+1} + (1-\theta)\alpha\hat{W}_{33}^n \right\}\left(\hat{u}_1^{n+1} - \hat{u}_1^n\right) \end{array} \right] dx \quad\text{............(A.51)}$$

$$S_4 = 0 \quad\text{...(A.52)}$$

$$S_5 = \int_e \left[-f_i \left(\hat{h}^{n+1} - \hat{h}^n \right) \right] dx \quad \text{...(A.53)}$$

$$S_6 = \int_e \left[\frac{1}{4} f_i \left(\hat{h}^{2\,n+1} - \hat{h}^{2\,n} \right) \right] dx \quad \text{...(A.54)}$$

$$S_7 = \int_e \left[f_i \left(\hat{h}^{n+1} \widehat{\bar{w}}^{n+1} - \hat{h}^n \widehat{\bar{w}}^n \right) \right] dx \quad \text{...(A.55)}$$

$$S_8 = \int_e f_i \left[\begin{array}{c} \frac{1}{4} \left\{ \theta \widehat{\bar{w}}^{n+1} + (1-\theta) \widehat{\bar{w}}^n \right\} \left(\hat{h}^{2\,n+1} - \hat{h}^{2\,n} \right) \\ -\frac{1}{12} \left\{ \hat{h}^{2\,n+1} \left(\hat{w}_b^{n+1} - \hat{w}_h^{n+1} \right) - \hat{h}^{2\,n} \left(\hat{w}_b^n - \hat{w}_h^n \right) \right\} \end{array} \right] dx \quad \text{.............................(A.56)}$$

where $S_I (I = 1,8)$ represents a $N_e \times 1$ vector, N_e being the number of nodes per element, θ is the implicitness factor, in the above integrals e implies integration over an element and α is given by

$$\alpha = \omega \frac{\Delta x}{2} \frac{df_i}{dx} \quad \text{...(A.57)}$$

where ω is the upwinding parameter. Hicks and Steffler (1990), through the stability analysis found that the CDG-1D scheme is relatively insensitive to the value of upwinding parameter and recommended a value from 0.25 to 0.5.

The part of (A.37) to (A.44) without temporal derivatives are given by:

$$K_1 = \int_e \left[\hat{F}_1 + \alpha \left(\hat{W}_{11} \hat{E}_1 + \hat{W}_{12} \hat{E}_2 + \hat{W}_{13} \hat{E}_3 \right) \right] dx \quad \text{..(A.58)}$$

103

$$\mathbf{K}_2 = \int_e \left[\hat{F}_2 + \alpha \left(\hat{W}_{21}\hat{E}_1 + \hat{W}_{22}\hat{E}_2 + \hat{W}_{23}\hat{E}_3 \right) \right] dx \quad\text{(A.59)}$$

$$\mathbf{K}_3 = \int_e \left[\hat{F}_3 + \alpha \left(\hat{W}_{31}\hat{E}_1 + \hat{W}_{32}\hat{E}_2 + \hat{W}_{33}\hat{E}_3 \right) \right] dx \quad\text{(A.60)}$$

$$\mathbf{K}_4 = \int_e \hat{F}_4 \, dx \quad\text{(A.61)}$$

$$\mathbf{K}_5 = \int_e \hat{F}_5 \, dx \quad\text{(A.62)}$$

$$\mathbf{K}_6 = \int_e \hat{F}_6 \, dx \quad\text{(A.63)}$$

$$\mathbf{K}_7 = \int_e \hat{F}_7 \, dx \quad\text{(A.64)}$$

$$\mathbf{K}_8 = \int_e \hat{F}_8 \, dx \quad\text{(A.65)}$$

where $\mathbf{K}_l (l = 1,8)$ represents a $N_e \times 1$ vector and $\hat{F}_1$ to $\hat{F}_8$ are given by:

$$\hat{F}_1 = -\frac{df_i}{dx}\hat{q} \quad\text{(A.66)}$$

$$\hat{F}_2 = -\frac{df_i}{dx}\left(\frac{\hat{q}^2}{\hat{h}} + \frac{g\hat{h}^2}{2} + \frac{\hat{h}\hat{u}_1^2}{3} + \frac{\hat{h}\hat{p}_1}{2\rho} + \frac{2\hat{h}\hat{p}_2}{3\rho} \right) + f_i\left(g\hat{h}\frac{\partial z_b}{\partial x} + \frac{\hat{p}_1}{\rho}\frac{\partial z_b}{\partial x} + \frac{\hat{q}^2}{\hat{h}^2\hat{C}_*^2} \right) \quad\text{(A.67)}$$

$$\hat{F}_3 = -\frac{df_i}{dx}\left(\frac{\hat{q}\hat{u}_1}{\hat{h}} \right) + f_i\left[-\frac{1}{2\rho}\left(\frac{\partial \hat{p}_1}{\partial x} - \frac{\hat{p}_1}{\hat{h}}\frac{\partial \hat{h}}{\partial x} \right) + \frac{4\hat{p}_2}{\hat{h}\rho}\frac{\partial \hat{z}}{\partial x} - \frac{3\hat{q}^2}{\hat{h}^3\hat{C}_*^2} \right] \quad\text{(A.68)}$$

104

$$\hat{F}_4 = f_i \left[\hat{w}_h - \left(\frac{\hat{q}}{\hat{h}} - \hat{u}_1 \right) \frac{\partial z_b}{\partial x} \right] \quad \text{(A.69)}$$

$$\hat{F}_5 = f_i \left[\hat{w}_h - \left(\frac{\hat{q}}{\hat{h}} + \hat{u}_1 \right) \frac{\partial \left(z_b + \hat{h} \right)}{\partial x} \right] \quad \text{(A.70)}$$

$$\hat{F}_6 = f_i \left[\hat{q} \frac{\partial \hat{\bar{z}}}{\partial x} + \frac{\hat{h}^2}{6} \frac{\partial \hat{u}_1}{\partial x} + \frac{\hat{h}\hat{u}_1}{3} \frac{\partial \hat{h}}{\partial x} - \hat{h}\hat{\bar{w}} \right] \quad \text{(A.71)}$$

$$\hat{F}_7 = f_i \left[\begin{array}{l} \hat{\bar{w}} \dfrac{\partial \hat{q}}{\partial x} + \hat{q} \dfrac{\partial \hat{\bar{w}}}{\partial x} - \dfrac{1}{6} \left(\hat{w}_b - \hat{w}_h \right) \left(\hat{u}_1 \dfrac{\partial \hat{h}}{\partial x} + \hat{h} \dfrac{\partial \hat{u}_1}{\partial x} \right) \\[3mm] - \dfrac{\hat{h}\hat{u}_1}{6} \dfrac{\partial \left(\hat{w}_b - \hat{w}_h \right)}{\partial x} + \dfrac{\hat{q}^2}{\hat{h}^2 \hat{C}_*^2} \dfrac{\partial z_b}{\partial x} - \dfrac{\hat{p}_1}{\rho} \end{array} \right] \quad \text{(A.72)}$$

$$\hat{F}_8 = f_i \left[\begin{array}{l} \left\{ \hat{q}\hat{\bar{w}} - \dfrac{\hat{h}\hat{u}_1}{6} \left(\hat{w}_b - \hat{w}_h \right) \right\} \dfrac{\partial \hat{\bar{z}}}{\partial x} - \dfrac{\hat{h}\hat{q}}{12} \dfrac{\partial \left(\hat{w}_b - \hat{w}_h \right)}{\partial x} - \dfrac{\left(\hat{w}_b - \hat{w}_h \right)}{12} \left(\hat{q} \dfrac{\partial \hat{h}}{\partial x} + \hat{h} \dfrac{\partial \hat{q}}{\partial x} \right) \\[3mm] + \dfrac{\hat{h}^2 \hat{u}_1}{10} \dfrac{\partial}{\partial x} \left(\hat{\bar{w}} + \dfrac{\hat{w}_b}{3} + \dfrac{\hat{w}_h}{3} \right) + \dfrac{1}{10} \left(\hat{\bar{w}} + \dfrac{\hat{w}_b}{3} + \dfrac{\hat{w}_h}{3} \right) \left(\hat{h}^2 \dfrac{\partial \hat{u}_1}{\partial x} + 2\hat{h}\hat{u}_1 \dfrac{\partial \hat{h}}{\partial x} \right) \\[3mm] - \hat{h}\overline{\hat{w}^2} - \dfrac{\hat{q}^2}{2\hat{h}\hat{C}_*^2} \dfrac{\partial z_b}{\partial x} - \dfrac{2}{3\rho} \hat{h}\hat{p}_2 \end{array} \right] \quad \text{....(A.73)}$$

The general form of the residuals, with Δt being the temporal discretization, are as follows

$$\mathbf{R}_l = \mathbf{S}_l + \theta \Delta t \mathbf{K}_l^{n+1} + (1 - \theta) \Delta t \mathbf{K}_l^n \text{ (for } l = 1,8) \quad \text{(A.74)}$$

105

which represents the finite element equivalent of (A.1) to (A.8). Each of the element of $\mathbf{R}_I$ represent a $N_e \times 1$ vector. For the integration over an element, the indices i and j take on a value from 1 to N_e.

To evaluate an analytical Jacobian, (A.46)-(A.53) and (A.55)-(A.62) are differentiated with respect to each of the unknowns. For the upwinding matrix the differentiation of each element with respect to each of the unknowns is as follows:

$$\hat{W}_{11} = \frac{1}{3\hat{c}^2}\left[-\hat{u}_1^2\hat{\lambda}_6 + \frac{3}{2}\hat{c}^2\hat{\lambda}_4 - \frac{3}{2}\frac{\hat{q}}{h}\hat{c}\hat{\lambda}_5\right] \quad\text{(A.75)}$$

$$\hat{W}_{11,1} = \left[-\frac{g}{\hat{c}^2}\hat{W}_{11} + \frac{1}{3\hat{c}^2}\left\{\frac{3}{2}g\hat{\lambda}_4 - \frac{3}{4}\frac{g}{\hat{c}}\frac{\hat{q}}{h}\hat{\lambda}_5 + \frac{3}{2}\frac{\hat{q}}{h^2}\hat{c}\hat{\lambda}_5\right\}\right]f_j \quad\text{(A.76)}$$

$$\hat{W}_{11,2} = \frac{1}{3\hat{c}^2}\left[-\frac{3}{2}\frac{1}{h}\hat{c}\hat{\lambda}_5\right]f_j \quad\text{(A.77)}$$

$$\hat{W}_{11,3} = \left[-\frac{2\hat{u}_1}{\hat{c}^2}\hat{W}_{11} + \frac{1}{3\hat{c}^2}\left(-2\hat{u}_1\hat{\lambda}_6\right)\right]f_j \quad\text{(A.78)}$$

$$\hat{W}_{12} = \frac{1}{2\hat{c}}\left(\hat{\lambda}_5\right) \quad\text{(A.79)}$$

$$\hat{W}_{12,1} = \left[-\frac{g}{2\hat{c}^2}\hat{W}_{12}\right]f_j \quad\text{(A.80)}$$

$$\hat{W}_{12,3} = \left[-\frac{\hat{u}_1}{\hat{c}^2}\hat{W}_{12}\right]f_j \quad\text{(A.81)}$$

$$\hat{W}_{13} = \frac{h\hat{u}_1}{3\hat{c}^2}\hat{\lambda}_6 \quad\text{(A.82)}$$

$$\hat{W}_{13,1} = \left[-\frac{g}{\hat{c}^2} \hat{W}_{13} + \frac{\hat{u}_1}{3\hat{c}^2} \hat{\lambda}_6 \right] f_j \dotfill (A.83)$$

$$\hat{W}_{13,3} = \left[-\frac{2\hat{u}_1}{\hat{c}^2} \hat{W}_{13} + \frac{\hat{h}}{3\hat{c}^2} \hat{\lambda}_6 \right] f_j \dotfill (A.84)$$

$$\hat{W}_{21} = \frac{1}{3\hat{c}^3} \left[\left(\frac{\hat{q}^2}{\hat{h}^2} - \hat{c}^2 \right) \left(\hat{u}_1^2 - \frac{3}{2}\hat{c}^2 \right) \hat{\lambda}_5 + \frac{\hat{q}}{\hat{h}} \hat{u}_1^2 \left(-\frac{\hat{q}}{\hat{h}} \hat{\lambda}_5 - \hat{c}\hat{\lambda}_6 \right) \right] \dotfill (A.85)$$

$$\hat{W}_{21,1} = \left[-\frac{3g}{2\hat{c}^2} \hat{W}_{21} + \frac{1}{3\hat{c}^3} \left\{ \begin{array}{l} \left(-\frac{2\hat{q}^2}{\hat{h}^3} - g \right) \left(\hat{u}_1^2 - \frac{3}{2}\hat{c}^2 \right) \hat{\lambda}_5 + \left(\frac{\hat{q}^2}{\hat{h}^2} - \hat{c}^2 \right) \left(-\frac{3g}{2} \right) \hat{\lambda}_5 \\ -\frac{\hat{q}}{\hat{h}^2} \hat{u}_1^2 \left(-\frac{\hat{q}}{\hat{h}} \hat{\lambda}_5 - \hat{c}\hat{\lambda}_6 \right) + \frac{\hat{q}}{\hat{h}} \hat{u}_1^2 \left(\frac{\hat{q}}{\hat{h}^2} \hat{\lambda}_5 - \frac{g}{2\hat{c}} \hat{\lambda}_6 \right) \end{array} \right\} \right] f_j \,..(A.86)$$

$$\hat{W}_{21,2} = \frac{1}{3\hat{c}^3} \left[\frac{2\hat{q}}{\hat{h}^2} \left(\hat{u}_1^2 - \frac{3}{2}\hat{c}^2 \right) \hat{\lambda}_5 + \frac{\hat{u}_1^2}{\hat{h}^2} \left(-\frac{\hat{q}}{\hat{h}} \hat{\lambda}_5 - \hat{c}\hat{\lambda}_6 \right) + \frac{\hat{q}}{\hat{h}} \hat{u}_1^2 \left(-\frac{1}{\hat{h}^2} \hat{\lambda}_5 \right) \right] f_j \dotfill (A.87)$$

$$\hat{W}_{21,3} = \left[-\frac{3\hat{u}_1}{\hat{c}^2} \hat{W}_{21} + \frac{1}{3\hat{c}^3} \left\{ \begin{array}{l} (-2\hat{u}_1) \left(\hat{u}_1^2 - \frac{3}{2}\hat{c}^2 \right) \hat{\lambda}_5 + \left(\frac{\hat{q}^2}{\hat{h}^2} - \hat{c}^2 \right) (-\hat{u}_1) \hat{\lambda}_5 \\ +\frac{2\hat{q}}{\hat{h}} \hat{u}_1 \left(-\frac{\hat{q}}{\hat{h}} \hat{\lambda}_5 - \hat{c}\hat{\lambda}_6 \right) + \frac{\hat{q}}{\hat{h}} \hat{u}_1^2 \left(-\frac{\hat{u}_1}{\hat{c}} \hat{\lambda}_6 \right) \end{array} \right\} \right] f_j \dotfill (A.88)$$

$$\hat{W}_{22} = \frac{1}{2\hat{c}} \left[\frac{\hat{q}}{\hat{h}} \hat{\lambda}_5 + \hat{c}\hat{\lambda}_4 \right] \dotfill (A.89)$$

$$\hat{W}_{22,1} = \left[-\frac{g}{2\hat{c}^2} \hat{W}_{22} + \frac{1}{2\hat{c}} \left(-\frac{\hat{q}}{\hat{h}^2} \hat{\lambda}_5 + \frac{g}{2\hat{c}} \hat{\lambda}_4 \right) \right] f_j \dotfill (A.90)$$

$$\hat{W}_{22,2} = \frac{1}{2\hat{c}} \left[\frac{1}{\hat{h}} \hat{\lambda}_5 \right] f_j \dotfill (A.91)$$

$$\hat{W}_{22,3} = \left[-\frac{\hat{u}_1}{\hat{c}^2}\hat{W}_{22} + \frac{1}{2\hat{c}}\left(\frac{\hat{u}_1}{\hat{c}}\hat{\lambda}_4 \right) \right] f_j \quad\text{...(A.92)}$$

$$\hat{W}_{23} = \frac{\hat{h}\hat{u}_1}{3\hat{c}^2}\left[\frac{\hat{q}}{\hat{h}}\hat{\lambda}_6 + \hat{c}\hat{\lambda}_5 \right] \quad\text{...(A.93)}$$

$$\hat{W}_{23,1} = \left[-\frac{g}{\hat{c}^2}\hat{W}_{23} + \frac{\hat{u}_1}{3\hat{c}^2}\left(\hat{c}\hat{\lambda}_5 + \hat{h}\frac{g}{2\hat{c}}\hat{\lambda}_5 \right) \right] f_j \quad\text{..............................(A.94)}$$

$$\hat{W}_{23,2} = \frac{\hat{h}\hat{u}_1}{3\hat{c}^2}\left[\frac{1}{\hat{h}}\hat{\lambda}_6 \right] f_j \quad\text{...(A.95)}$$

$$\hat{W}_{23,3} = \left[-\frac{2\hat{u}_1}{\hat{c}^2}\hat{W}_{23} + \frac{\hat{h}}{3\hat{c}^2}\left(\frac{\hat{q}}{\hat{h}}\hat{\lambda}_6 + \hat{c}\hat{\lambda}_5 \right) + \frac{\hat{h}\hat{u}_1}{3\hat{c}^2}\left(\frac{\hat{u}_1}{\hat{c}}\hat{\lambda}_5 \right) \right] f_j \quad\text{.............(A.96)}$$

$$\hat{W}_{31} = \frac{\hat{u}_1}{3\hat{h}\hat{c}^2}\left[-\left(\hat{u}_1^2 - \frac{3}{2}\hat{c}^2 \right)\hat{\lambda}_6 - \frac{3}{2}\frac{\hat{q}}{\hat{h}}\hat{c}\hat{\lambda}_5 \right] \quad\text{..(A.97)}$$

$$\hat{W}_{31,1} = \left[-\left(\frac{g}{\hat{c}^2} + \frac{1}{\hat{h}} \right)\hat{W}_{31} + \frac{\hat{u}_1}{3\hat{h}\hat{c}^2}\left\{ \left(\frac{3}{2}g \right)\hat{\lambda}_6 - \frac{3}{2}\hat{\lambda}_5\left(-\frac{\hat{q}}{\hat{h}^2}\hat{c} + \frac{\hat{q}}{2\hat{h}\hat{c}}g \right) \right\} \right] f_j \quad\text{..................(A.98)}$$

$$\hat{W}_{31,2} = \frac{\hat{u}_1}{3\hat{h}\hat{c}^2}\left[-\frac{3}{2\hat{h}}\hat{c}\hat{\lambda}_5 \right] f_j \quad\text{...(A.99)}$$

$$\hat{W}_{31,3} = \left[-\left(\frac{2\hat{u}_1}{\hat{c}^2} - \frac{1}{\hat{u}_1} \right)\hat{W}_{31} + \frac{\hat{u}_1}{3\hat{h}\hat{c}^2}\left\{ (\hat{u}_1)\hat{\lambda}_6 - \frac{3}{2}\frac{\hat{q}}{\hat{h}}\frac{\hat{u}_1}{\hat{c}}\hat{\lambda}_5 \right\} \right] f_j \quad\text{.............................(A.100)}$$

$$\hat{W}_{32} = \frac{\hat{u}_1}{2\hat{h}\hat{c}}\hat{\lambda}_5 \quad\text{...(A.101)}$$

$$\hat{W}_{32,1} = \left[-\frac{\hat{u}_1}{2}\hat{\lambda}_5\left(\frac{g}{2\hat{h}\hat{c}^3} + \frac{1}{2\hat{h}^2\hat{c}} \right) \right] f_j \quad\text{...(A.102)}$$

$$\hat{W}_{32,3} = \left[\frac{1}{2\hat{h}} \hat{\lambda}_5 \left(\frac{1}{\hat{c}} - \frac{\hat{u}_1^2}{\hat{c}^3} \right) \right] f_j \dotfill \text{(A.103)}$$

$$\hat{W}_{33} = \frac{\hat{u}_1^2}{3\hat{c}^2} \hat{\lambda}_6 + \hat{\lambda}_3 \dotfill \text{(A.104)}$$

$$\hat{W}_{33,1} = \left[-\frac{\hat{u}_1^2}{3\hat{c}^4} g \hat{\lambda}_6 \right] f_j \dotfill \text{(A.105)}$$

$$\hat{W}_{33,2} = \left[\frac{2\hat{u}_1}{3\hat{c}^2} \hat{\lambda}_6 - \frac{2\hat{u}_1^3}{3\hat{c}^4} \hat{\lambda}_6 \right] f_j \dotfill \text{(A.106)}$$

where

$$\hat{\lambda}_4 = \hat{\lambda}_1 + \hat{\lambda}_2 \dotfill \text{(A.107)}$$

$$\hat{\lambda}_5 = \hat{\lambda}_1 - \hat{\lambda}_2 \dotfill \text{(A.108)}$$

$$\hat{\lambda}_6 = \hat{\lambda}_1 + \hat{\lambda}_2 - 2\hat{\lambda}_3 \dotfill \text{(A.109)}$$

$\hat{W}_{11}$ is the first element of the upwinding matrix, $\hat{W}_{11,1}$ represents a derivative with respect to nodal values of h and $\hat{W}_{11,8}$ represents a derivative with respect to nodal values of p_2, which in this case is zero and is not reported. The equations for $\hat{E}_1$ to $\hat{E}_3$ and their derivatives with respect to each of the unknown are:

$$\hat{E}_1 = \frac{\partial \hat{q}}{\partial x} \dotfill \text{(A.110)}$$

$$\hat{E}_{1,2} = \frac{df_j}{dx} \dotfill (A.111)$$

$$\hat{E}_2 = \left(-\frac{\hat{q}^2}{\hat{h}^2} + g\hat{h} + \frac{\hat{u}_1^2}{3} + \frac{\hat{p}_1}{2\rho} + \frac{2\hat{p}_2}{3\rho}\right)\frac{\partial \hat{h}}{\partial x} + \frac{2\hat{q}}{\hat{h}}\frac{\partial \hat{q}}{\partial x} + \frac{2\hat{h}\hat{u}_1}{3}\frac{\partial \hat{u}_1}{\partial x} + \frac{\hat{h}}{2\rho}\frac{\partial \hat{p}_1}{\partial x}$$

$$+ \frac{2\hat{h}}{3\rho}\frac{\partial \hat{p}_2}{\partial x} + g\hat{h}\frac{\partial z_b}{\partial x} + \frac{\hat{p}_1}{\rho}\frac{\partial z_b}{\partial x} + \frac{\hat{q}^2}{\hat{h}^2\hat{C}_*^2} \dotfill (A.112)$$

$$\hat{E}_{2,1} = \left(\begin{matrix}-\frac{\hat{q}^2}{\hat{h}^2} + g\hat{h} + \frac{\hat{u}_1^2}{3} \\ +\frac{\hat{p}_1}{2\rho} + \frac{2\hat{p}_2}{3\rho}\end{matrix}\right)\frac{df_j}{dx} + \left\{\begin{matrix}\left(\frac{2\hat{q}^2}{\hat{h}^3} + g\right)\frac{\partial \hat{h}}{\partial x} - \frac{2\hat{q}}{\hat{h}^2}\frac{\partial \hat{q}}{\partial x} + \frac{2\hat{u}_1}{3}\frac{\partial \hat{u}_1}{\partial x} \\ +\frac{1}{2\rho}\frac{\partial \hat{p}_1}{\partial x} + \frac{2}{3\rho}\frac{\partial \hat{p}_2}{\partial x} + g\frac{\partial z_b}{\partial x} - \frac{2\hat{q}^2}{\hat{h}^3\hat{C}_*^2}\end{matrix}\right\}f_j \dotfill (A.113)$$

$$\hat{E}_{2,2} = \left(-\frac{2\hat{q}}{\hat{h}^2}\frac{\partial \hat{h}}{\partial x} + \frac{2}{\hat{h}}\frac{\partial \hat{q}}{\partial x} + \frac{2\hat{q}}{\hat{h}^2\hat{C}_*^2}\right)f_j + \frac{2\hat{q}}{\hat{h}}\frac{df_j}{dx} \dotfill (A.114)$$

$$\hat{E}_{2,3} = \left(\frac{2\hat{u}_1}{3}\frac{\partial \hat{h}}{\partial x} + \frac{2\hat{h}}{3}\frac{\partial \hat{u}_1}{\partial x}\right)f_j + \frac{2\hat{h}\hat{u}_1}{3}\frac{df_j}{dx} \dotfill (A.115)$$

$$\hat{E}_{2,7} = \left(\frac{1}{2\rho}\frac{\partial \hat{h}}{\partial x} + \frac{1}{\rho}\frac{\partial z_b}{\partial x}\right)f_j + \frac{\hat{h}}{2\rho}\frac{df_j}{dx} \dotfill (A.116)$$

$$\hat{E}_{2,8} = \frac{2}{3\rho}\frac{\partial \hat{h}}{\partial x}f_j + \frac{2\hat{h}}{3\rho}\frac{df_j}{dx} \dotfill (A.117)$$

$$\hat{E}_3 = \frac{\hat{q}}{\hat{h}}\frac{\partial \hat{u}_1}{\partial x} + \frac{\hat{u}_1}{\hat{h}}\frac{\partial \hat{q}}{\partial x} - \frac{\hat{q}\hat{u}_1}{\hat{h}^2}\frac{\partial \hat{h}}{\partial x} - \frac{1}{2\rho}\left(\frac{\partial \hat{p}_1}{\partial x} - \frac{\hat{p}_1}{\hat{h}}\frac{\partial \hat{h}}{\partial x}\right) + \frac{4\hat{p}_2}{\hat{h}\rho}\frac{\partial \hat{z}}{\partial x} - \frac{3\hat{q}^2}{\hat{h}^3\hat{C}_*^2} \dotfill (A.118)$$

$$\hat{E}_{3,1} = \left(-\frac{\hat{q}\hat{u}_1}{\hat{h}^2} + \frac{\hat{p}_1}{2\rho\hat{h}} + \frac{2\hat{p}_2}{\hat{h}\rho}\right)\frac{df_j}{dx} + \left(\begin{array}{c} -\dfrac{\hat{q}}{\hat{h}^2}\dfrac{\partial\hat{u}_1}{\partial x} - \dfrac{\hat{u}_1}{\hat{h}^2}\dfrac{\partial\hat{q}}{\partial x} + \dfrac{2\hat{q}\hat{u}_1}{\hat{h}^3}\dfrac{\partial\hat{h}}{\partial x} \\[2mm] -\dfrac{\hat{p}_1}{2\rho\hat{h}^2}\dfrac{\partial\hat{h}}{\partial x} - \dfrac{4\hat{p}_2}{\hat{h}^2\rho}\dfrac{\partial\hat{z}}{\partial x} + \dfrac{9\hat{q}^2}{\hat{h}^4\hat{C}_*^2} \end{array}\right)f_j \quad\text{.................}(\text{A.119})$$

$$\hat{E}_{3,2} = \left(\frac{1}{\hat{h}}\frac{\partial\hat{u}_1}{\partial x} - \frac{\hat{u}_1}{\hat{h}^2}\frac{\partial\hat{h}}{\partial x} - \frac{6\hat{q}}{\hat{h}^3\hat{C}_*^2}\right)f_j + \frac{\hat{u}_1}{\hat{h}}\frac{df_j}{dx} \quad\text{..}(\text{A.120})$$

$$\hat{E}_{3,3} = \frac{\hat{q}}{\hat{h}}\frac{df_j}{dx} + \left(\frac{1}{\hat{h}}\frac{\partial\hat{q}}{\partial x} - \frac{\hat{q}}{\hat{h}^2}\frac{\partial\hat{h}}{\partial x}\right)f_j \quad\text{...}(\text{A.121})$$

$$\hat{E}_{3,7} = -\frac{1}{2\rho}\left(\frac{df_j}{dx} - \frac{1}{\hat{h}}\frac{\partial\hat{h}}{\partial x}f_j\right) \quad\text{...}(\text{A.122})$$

$$\hat{E}_{3,8} = \frac{4}{\hat{h}\rho}\frac{\partial\hat{z}}{\partial x}f_j \quad\text{..}(\text{A.123})$$

Next, the derivatives of S_1 to S_8 and $\hat{F}_1$ to $\hat{F}_2$ with respect to the nodal values of each of the unknown are presented:

$$S_{1,1} = \int_e \left[\begin{array}{l} \left\{f_i + \theta\alpha\hat{W}_{11}^{n+1} + (1-\theta)\alpha\hat{W}_{11}^n\right\}f_j + \theta\alpha\hat{W}_{11,1}^{n+1}\left(\hat{h}^{n+1} - \hat{h}^n\right) \\[2mm] +\theta\alpha\hat{W}_{12,1}^{n+1}\left(\hat{q}^{n+1} - \hat{q}^n\right) + \theta\alpha\hat{W}_{13,1}^{n+1}\left(\hat{u}_1^{n+1} - \hat{u}_1^n\right) \end{array}\right]dx \quad\text{...............}(\text{A.124})$$

$$S_{1,2} = \int_e \left[\begin{array}{l} \theta\alpha\hat{W}_{11,2}^{n+1}\left(\hat{h}^{n+1} - \hat{h}^n\right) + \left\{\theta\alpha\hat{W}_{12}^{n+1} + (1-\theta)\alpha\hat{W}_{12}^n\right\}f_j \\[2mm] +\theta\alpha\hat{W}_{12,2}^{n+1}\left(\hat{q}^{n+1} - \hat{q}^n\right) + \theta\alpha\hat{W}_{13,2}^{n+1}\left(\hat{u}_1^{n+1} - \hat{u}_1^n\right) \end{array}\right]dx \quad\text{...............}(\text{A.125})$$

111

$$S_{1,3} = \int_e \left[\begin{array}{l} \theta\alpha \hat{W}_{11,3}^{n+1}\left(\hat{h}^{n+1} - \hat{h}^n\right) + \theta\alpha \hat{W}_{12,3}^{n+1}\left(\hat{q}^{n+1} - \hat{q}^n\right) \\ + \left\{\theta\alpha \hat{W}_{13}^{n+1} + (1-\theta)\alpha \hat{W}_{13}^n\right\}f_j + \theta\alpha \hat{W}_{13,3}^{n+1}\left(\hat{u}_1^{n+1} - \hat{u}_1^n\right) \end{array} \right] dx \dots\dots\dots\dots (A.126)$$

$$S_{2,1} = \int_e \left[\begin{array}{l} \left\{\theta\alpha \hat{W}_{21}^{n+1} + (1-\theta)\alpha \hat{W}_{21}^n\right\}f_j + \theta\alpha \hat{W}_{21,1}^{n+1}\left(\hat{h}^{n+1} - \hat{h}^n\right) \\ + \theta\alpha \hat{W}_{22,1}^{n+1}\left(\hat{q}^{n+1} - \hat{q}^n\right) + \theta\alpha \hat{W}_{23,1}^{n+1}\left(\hat{u}_1^{n+1} - \hat{u}_1^n\right) \end{array} \right] dx \dots\dots\dots\dots (A.127)$$

$$S_{2,2} = \int_e \left[\begin{array}{l} \theta\alpha \hat{W}_{21,2}^{n+1}\left(\hat{h}^{n+1} - \hat{h}^n\right) + \left\{f_i + \theta\alpha \hat{W}_{22}^{n+1} + (1-\theta)\alpha \hat{W}_{22}^n\right\}f_j \\ + \theta\alpha \hat{W}_{22,2}^{n+1}\left(\hat{q}^{n+1} - \hat{q}^n\right) + \theta\alpha \hat{W}_{23,2}^{n+1}\left(\hat{u}_1^{n+1} - \hat{u}_1^n\right) \end{array} \right] dx \dots\dots\dots (A.128)$$

$$S_{2,3} = \int_e \left[\begin{array}{l} \theta\alpha \hat{W}_{21,3}^{n+1}\left(\hat{h}^{n+1} - \hat{h}^n\right) + \theta\alpha \hat{W}_{22,3}^{n+1}\left(\hat{q}^{n+1} - \hat{q}^n\right) \\ + \left\{\theta\alpha \hat{W}_{23}^{n+1} + (1-\theta)\alpha \hat{W}_{23}^n\right\}f_j + \theta\alpha \hat{W}_{23,3}^{n+1}\left(\hat{u}_1^{n+1} - \hat{u}_1^n\right) \end{array} \right] dx \dots\dots\dots\dots (A.129)$$

$$S_{3,1} = \int_e \left[\begin{array}{l} \left\{\theta\alpha \hat{W}_{31}^{n+1} + (1-\theta)\alpha \hat{W}_{31}^n\right\}f_j + \theta\alpha \hat{W}_{31,1}^{n+1}\left(\hat{h}^{n+1} - \hat{h}^n\right) \\ + \theta\alpha \hat{W}_{32,1}^{n+1}\left(\hat{q}^{n+1} - \hat{q}^n\right) + \theta\alpha \hat{W}_{33,1}^{n+1}\left(\hat{u}_1^{n+1} - \hat{u}_1^n\right) \end{array} \right] dx \dots\dots\dots\dots (A.130)$$

$$S_{3,2} = \int_e \left[\begin{array}{l} \theta\alpha \hat{W}_{31,2}^{n+1}\left(\hat{h}^{n+1} - \hat{h}^n\right) + \left\{\theta\alpha \hat{W}_{32}^{n+1} + (1-\theta)\alpha \hat{W}_{32}^n\right\}f_j \\ + \theta\alpha \hat{W}_{32,2}^{n+1}\left(\hat{q}^{n+1} - \hat{q}^n\right) + \theta\alpha \hat{W}_{33,2}^{n+1}\left(\hat{u}_1^{n+1} - \hat{u}_1^n\right) \end{array} \right] dx \dots\dots\dots\dots (A.131)$$

$$S_{3,3} = \int_e \left[\begin{array}{l} \theta\alpha \hat{W}_{31,3}^{n+1}\left(\hat{h}^{n+1} - \hat{h}^n\right) + \theta\alpha \hat{W}_{32,3}^{n+1}\left(\hat{q}^{n+1} - \hat{q}^n\right) \\ + \left\{f_i + \theta\alpha \hat{W}_{33}^{n+1} + (1-\theta)\alpha \hat{W}_{33}^n\right\}f_j + \theta\alpha \hat{W}_{33,3}^{n+1}\left(\hat{u}_1^{n+1} - \hat{u}_1^n\right) \end{array} \right] dx \dots\dots\dots (A.132)$$

$$S_{5,1} = \int_e \left[-f_i f_j \right] dx \dots\dots\dots\dots\dots\dots\dots\dots\dots\dots\dots\dots\dots (A.133)$$

$$\mathbf{S}_{6,1} = \int_e \left[\frac{1}{2} \hat{h}^{n+1} f_i f_j \right] dx \quad \text{...(A.134)}$$

$$\mathbf{S}_{7,1} = \int_e \left[\hat{\overline{w}}^{n+1} f_i f_j \right] dx \quad \text{...(A.135)}$$

$$\mathbf{S}_{7,6} = \int_e \left[\hat{h}^{n+1} f_i f_j \right] dx \quad \text{...(A.136)}$$

$$\mathbf{S}_{8,1} = \int_e f_i \left[\frac{1}{2} \left\{ \theta \hat{\overline{w}}^{n+1} + (1-\theta) \hat{\overline{w}}^n \right\} \hat{h}^{n+1} f_j - \frac{1}{6} \left(\hat{w}_b^{n+1} - \hat{w}_h^{n+1} \right) \hat{h}^{n+1} f_j \right] dx \quad \text{.............(A.137)}$$

$$\mathbf{S}_{8,4} = \int_e f_i \left[-\frac{1}{12} \hat{h}^{2\,n+1} f_j \right] dx \quad \text{...(A.138)}$$

$$\mathbf{S}_{8,5} = \int_e f_i \left[\frac{1}{12} \hat{h}^{2\,n+1} f_j \right] dx \quad \text{...(A.139)}$$

$$\mathbf{S}_{8,6} = \int_e f_i \left[\frac{\theta}{4} \left(\hat{h}^{2\,n+1} - \hat{h}^{2\,n} \right) f_j \right] dx \quad \text{...(A.140)}$$

$$\hat{F}_{1,2} = -\frac{df_i}{dx} f_j \quad \text{...(A.141)}$$

$$\hat{F}_{2,1} = -\frac{df_i}{dx} f_j \left(-\frac{\hat{q}^2}{\hat{h}^2} + g\hat{h} + \frac{\hat{u}_1^2}{3} + \frac{\hat{p}_1}{2\rho} + \frac{2\hat{p}_2}{3\rho} \right) + f_i f_j \left(g\frac{\partial z_b}{\partial x} - \frac{2\hat{q}^2}{\hat{h}^3 \hat{C}_*^2} \right) \quad \text{....................(A.142)}$$

$$\hat{F}_{2,2} = -\frac{df_i}{dx} f_j \left(\frac{2\hat{q}}{\hat{h}} \right) + f_i f_j \left(\frac{2\hat{q}}{\hat{h}^2 \hat{C}_*^2} \right) \quad \text{...(A.143)}$$

113

$$\hat{F}_{2,3} = -\frac{df_i}{dx} f_j \left(\frac{2\hat{h}\hat{u}_1}{3} \right) \dots\dots\dots\dots\dots\dots\dots\dots\dots\dots\dots\dots\dots\dots\dots\text{(A.144)}$$

$$\hat{F}_{2,7} = -\frac{df_i}{dx} f_j \left(\frac{\hat{h}}{2\rho} \right) + f_i f_j \left(\frac{1}{\rho} \frac{\partial z_b}{\partial x} \right) \dots\dots\dots\dots\dots\dots\dots\dots\text{(A.145)}$$

$$\hat{F}_{2,8} = -\frac{df_i}{dx} f_j \left(\frac{2\hat{h}}{3\rho} \right) \dots\dots\dots\dots\dots\dots\dots\dots\dots\dots\dots\dots\dots\dots\text{(A.146)}$$

$$\hat{F}_{3,1} = -\frac{df_i}{dx} f_j \left(-\frac{\hat{q}\hat{u}_1}{\hat{h}^2} \right) + f_i \begin{bmatrix} -\frac{1}{2\rho} \left(\frac{\hat{p}_1}{\hat{h}^2} \frac{\partial \hat{h}}{\partial x} f_j - \frac{\hat{p}_1}{\hat{h}} \frac{df_j}{dx} \right) \\ -\frac{4\hat{p}_2}{\hat{h}^2\rho} \frac{\partial \hat{\bar{z}}}{\partial x} f_j + \frac{2\hat{p}_2}{\hat{h}\rho} \frac{df_j}{dx} + \frac{9\hat{q}^2}{\hat{h}^4\hat{C}_*^2} f_j \end{bmatrix} \dots\text{(A.147)}$$

$$\hat{F}_{3,2} = -\frac{df_i}{dx} f_j \left(\frac{\hat{u}_1}{\hat{h}} \right) + f_i f_j \left(-\frac{6\hat{q}}{\hat{h}^3\hat{C}_*^2} \right) \dots\dots\dots\dots\dots\dots\dots\text{(A.148)}$$

$$\hat{F}_{3,3} = -\frac{df_i}{dx} f_j \left(\frac{\hat{q}}{\hat{h}} \right) \dots\dots\dots\dots\dots\dots\dots\dots\dots\dots\dots\dots\dots\dots\text{(A.149)}$$

$$\hat{F}_{3,7} = f_i \left[-\frac{1}{2\rho} \left(\frac{df_j}{dx} - \frac{1}{\hat{h}} \frac{\partial \hat{h}}{\partial x} f_j \right) \right] \dots\dots\dots\dots\dots\dots\dots\dots\text{(A.150)}$$

$$\hat{F}_{3,8} = f_i f_j \left(\frac{4}{\hat{h}\rho} \frac{\partial \hat{\bar{z}}}{\partial x} \right) \dots\dots\dots\dots\dots\dots\dots\dots\dots\dots\dots\dots\dots\text{(A.151)}$$

$$\hat{F}_{4,1} = f_i f_j \left(\frac{\hat{q}}{\hat{h}^2} \frac{\partial z_b}{\partial x} \right) \dots\dots\dots\dots\dots\dots\dots\dots\dots\dots\dots\dots\dots\dots\text{(A.152)}$$

$$\hat{F}_{4,2} = f_i f_j \left(-\frac{1}{\hat{h}} \frac{\partial z_b}{\partial x} \right) \dots\dots\dots\dots\dots\dots\dots\dots\dots\dots\dots\dots\dots\dots\text{(A.153)}$$

$$\hat{F}_{4,3} = f_i f_j \left(\frac{\partial z_b}{\partial x} \right) \quad \dotfill \text{(A.154)}$$

$$\hat{F}_{4,4} = f_i f_j \quad \dotfill \text{(A.155)}$$

$$\hat{F}_{5,1} = f_i \left[-\left(\frac{\hat{q}}{\hat{h}} + \hat{u}_1 \right) \frac{df_j}{dx} + \frac{\hat{q}}{\hat{h}^2} \frac{\partial \left(z_b + \hat{h} \right)}{\partial x} f_j \right] \quad \dotfill \text{(A.156)}$$

$$\hat{F}_{5,2} = f_i f_j \left[-\frac{1}{\hat{h}} \frac{\partial \left(z_b + \hat{h} \right)}{\partial x} \right] \quad \dotfill \text{(A.157)}$$

$$\hat{F}_{5,3} = f_i f_j \left[-\frac{\partial \left(z_b + \hat{h} \right)}{\partial x} \right] \quad \dotfill \text{(A.158)}$$

$$\hat{F}_{5,5} = f_i f_j \quad \dotfill \text{(A.159)}$$

$$\hat{F}_{6,1} = f_i \left[\frac{\hat{q}}{2} \frac{df_j}{dx} + \frac{\hat{h}}{3} \frac{\partial \hat{u}_1}{\partial x} f_j + \frac{\hat{u}_1}{3} \left(\frac{\partial \hat{h}}{\partial x} f_j + \hat{h} \frac{df_j}{dx} \right) - \hat{\bar{w}} f_j \right] \quad \dotfill \text{(A.160)}$$

$$\hat{F}_{6,2} = f_i f_j \left(\frac{\partial \hat{\bar{z}}}{\partial x} \right) \quad \dotfill \text{(A.161)}$$

$$\hat{F}_{6,3} = f_i \left[\frac{\hat{h}^2}{6} \frac{df_j}{dx} + \frac{\hat{h}}{3} \frac{\partial \hat{h}}{\partial x} f_j \right] \quad \dotfill \text{(A.162)}$$

$$\hat{F}_{6,6} = f_i f_j \left(-\hat{h} \right) \quad \dotfill \text{(A.163)}$$

$$\hat{F}_{7,1} = f_i\left[-\frac{1}{6}(\hat{w}_b - \hat{w}_h)\left(\hat{u}_1\frac{df_j}{dx} + \frac{\partial\hat{u}_1}{\partial x}f_j\right) - \frac{\hat{u}_1}{6}\frac{\partial(\hat{w}_b - \hat{w}_h)}{\partial x}f_j - \frac{2\hat{q}^2}{\hat{h}^3\hat{C}_*^2}\frac{\partial z_b}{\partial x}f_j\right] \quad\text{......(A.164)}$$

$$\hat{F}_{7,2} = f_i\left(\hat{\overline{w}}\frac{df_j}{dx} + \frac{\partial\hat{\overline{w}}}{\partial x}f_j + \frac{2\hat{q}}{\hat{h}^2\hat{C}_*^2}\frac{\partial z_b}{\partial x}f_j\right) \quad\text{...(A.165)}$$

$$\hat{F}_{7,3} = f_i\left[-\frac{1}{6}(\hat{w}_b - \hat{w}_h)\left(\frac{\partial\hat{h}}{\partial x}f_j + \hat{h}\frac{df_j}{dx}\right) - \frac{\hat{h}}{6}\frac{\partial(\hat{w}_b - \hat{w}_h)}{\partial x}f_j\right] \quad\text{.....................(A.166)}$$

$$\hat{F}_{7,4} = f_i\left[-\frac{1}{6}\left(\hat{u}_1\frac{\partial\hat{h}}{\partial x} + \hat{h}\frac{\partial\hat{u}_1}{\partial x}\right)f_j - \frac{\hat{h}\hat{u}_1}{6}\frac{df_j}{dx}\right] \quad\text{.................................(A.167)}$$

$$\hat{F}_{7,5} = f_i\left[\frac{1}{6}\left(\hat{u}_1\frac{\partial\hat{h}}{\partial x} + \hat{h}\frac{\partial\hat{u}_1}{\partial x}\right)f_j + \frac{\hat{h}\hat{u}_1}{6}\frac{df_j}{dx}\right] \quad\text{...................................(A.168)}$$

$$\hat{F}_{7,6} = f_i\left(\frac{\partial\hat{q}}{\partial x}f_j + \hat{q}\frac{df_j}{dx}\right) \quad\text{..(A.169)}$$

$$\hat{F}_{7,7} = f_i f_j\left(-\frac{1}{\rho}\right) \quad\text{..(A.170)}$$

$$\hat{F}_{8,1} = f_i\begin{bmatrix}\frac{1}{2}\left\{\hat{q}\hat{\overline{w}} - \frac{\hat{h}\hat{u}_1}{6}(\hat{w}_b - \hat{w}_h)\right\}\frac{df_j}{dx} - \frac{\hat{q}}{12}\frac{\partial(\hat{w}_b - \hat{w}_h)}{\partial x}f_j \\[2ex] -\frac{(\hat{w}_b - \hat{w}_h)}{12}\left(\hat{q}\frac{df_j}{dx} + \frac{\partial\hat{q}}{\partial x}f_j\right) + \frac{\hat{h}\hat{u}_1}{5}\frac{\partial}{\partial x}\left(\hat{\overline{w}} + \frac{\hat{w}_b}{3} + \frac{\hat{w}_h}{3}\right)f_j \\[2ex] +\frac{1}{10}\left(\hat{\overline{w}} + \frac{\hat{w}_b}{3} + \frac{\hat{w}_h}{3}\right)\left(\hat{h}\frac{\partial\hat{u}_1}{\partial x}f_j + 2\hat{u}_1\frac{\partial\hat{h}}{\partial x}f_j + 2\hat{h}\hat{u}_1\frac{df_j}{dx}\right) \\[2ex] -\overline{\hat{w}^2}f_j + \frac{\hat{q}^2}{2\hat{h}^2\hat{C}_*^2}\frac{\partial z_b}{\partial x}f_j - \frac{2}{3\rho}\hat{p}_2 f_j\end{bmatrix} \quad\text{..................(A.171)}$$

$$\hat{F}_{8,2} = f_i\left[\left(\hat{\bar{w}}\frac{\partial\hat{\bar{z}}}{\partial x} - \frac{\hat{h}}{12}\frac{\partial(\hat{w}_b - \hat{w}_h)}{\partial x} - \frac{\hat{q}}{\hat{h}\hat{C}_*^2}\frac{\partial z_h}{\partial x}\right)f_j - \frac{(\hat{w}_b - \hat{w}_h)}{12}\left(\frac{\partial\hat{h}}{\partial x}f_j + \hat{h}\frac{df_j}{dx}\right)\right]\dots\text{(A.172)}$$

$$\hat{F}_{8,3} = f_i\begin{bmatrix}-\dfrac{\hat{h}}{6}(\hat{w}_b - \hat{w}_h)\dfrac{\partial\hat{\bar{z}}}{\partial x}f_j + \dfrac{\hat{h}^2}{10}\dfrac{\partial}{\partial x}\left(\hat{\bar{w}} + \dfrac{\hat{w}_b}{3} + \dfrac{\hat{w}_h}{3}\right)f_j \\[2mm] +\dfrac{1}{10}\left(\hat{\bar{w}} + \dfrac{\hat{w}_b}{3} + \dfrac{\hat{w}_h}{3}\right)\left(\hat{h}^2\dfrac{df_j}{dx} + 2\hat{h}\dfrac{\partial\hat{h}}{\partial x}f_j\right)\end{bmatrix}\dots\dots\text{(A.173)}$$

$$\hat{F}_{8,4} = f_i\begin{bmatrix}-\dfrac{\hat{h}\hat{u}_1}{6}\dfrac{\partial\hat{\bar{z}}}{\partial x}f_j - \left(\hat{q}\dfrac{\partial\hat{h}}{\partial x} + \hat{h}\dfrac{\partial\hat{q}}{\partial x}\right)f_j + \dfrac{1}{30}\left(\hat{h}^2\dfrac{\partial\hat{u}_1}{\partial x} + 2\hat{h}\hat{u}_1\dfrac{\partial\hat{h}}{\partial x}\right)f_j \\[2mm] -\dfrac{\hat{h}\hat{q}}{12}\dfrac{df_j}{dx} + \dfrac{\hat{h}^2\hat{u}_1}{30}\dfrac{df_j}{dx} - \hat{h}\left\{\dfrac{\hat{w}_b}{6} - \dfrac{\hat{w}_h}{6} - \dfrac{1}{10}\left(2\hat{\bar{w}} - \hat{w}_b - \hat{w}_h\right)\right\}f_j\end{bmatrix}\dots\text{(A.174)}$$

$$\hat{F}_{8,5} = f_i\begin{bmatrix}\dfrac{\hat{h}\hat{u}_1}{6}\dfrac{\partial\hat{\bar{z}}}{\partial x}f_j + \left(\hat{q}\dfrac{\partial\hat{h}}{\partial x} + \hat{h}\dfrac{\partial\hat{q}}{\partial x}\right)f_j + \dfrac{1}{30}\left(\hat{h}^2\dfrac{\partial\hat{u}_1}{\partial x} + 2\hat{h}\hat{u}_1\dfrac{\partial\hat{h}}{\partial x}\right)f_j \\[2mm] +\dfrac{\hat{h}\hat{q}}{12}\dfrac{df_j}{dx} + \dfrac{\hat{h}^2\hat{u}_1}{30}\dfrac{df_j}{dx} - \hat{h}\left\{\dfrac{\hat{w}_h}{6} - \dfrac{\hat{w}_b}{6} - \dfrac{1}{10}\left(2\hat{\bar{w}} - \hat{w}_b - \hat{w}_h\right)\right\}f_j\end{bmatrix}\dots\text{(A.175)}$$

$$\hat{F}_{8,6} = f_i\begin{bmatrix}\hat{q}\dfrac{\partial\hat{\bar{z}}}{\partial x}f_j + \dfrac{\hat{h}^2\hat{u}_1}{10}\dfrac{df_j}{dx} + \dfrac{1}{10}\left(\hat{h}^2\dfrac{\partial\hat{u}_1}{\partial x} + 2\hat{h}\hat{u}_1\dfrac{\partial\hat{h}}{\partial x}\right)f_j \\[2mm] -\hat{h}\left\{2\hat{\bar{w}} + \dfrac{1}{5}\left(2\hat{\bar{w}} - \hat{w}_b - \hat{w}_h\right)\right\}f_j\end{bmatrix}\dots\dots\text{(A.176)}$$

$$\hat{F}_{8,8} = f_i f_j\left(-\frac{2}{3\rho}\hat{h}\right)\dots\dots\text{(A.177)}$$

The derivatives of $\mathbf{K}_1$ to $\mathbf{K}_8$ can now be written as follows:

$$\mathbf{K}_{1,l} = \int_e\left[\hat{F}_{1,l} + \alpha\begin{pmatrix}\hat{W}_{11}\hat{E}_{1,l} + \hat{W}_{12}\hat{E}_{2,l} + \hat{W}_{13}\hat{E}_{3,l} \\ +\hat{W}_{11,l}\hat{E}_1 + \hat{W}_{12,l}\hat{E}_2 + \hat{W}_{13,l}\hat{E}_3\end{pmatrix}\right]dx\dots\dots\text{(A.178)}$$

117

$$K_{2,l} = \int_e \left[\hat{F}_{2,l} + \alpha \begin{pmatrix} \hat{W}_{21}\hat{E}_{1,l} + \hat{W}_{22}\hat{E}_{2,l} + \hat{W}_{23}\hat{E}_{3,l} \\ +\hat{W}_{21,l}\hat{E}_1 + \hat{W}_{22,l}\hat{E}_2 + \hat{W}_{23,l}\hat{E}_3 \end{pmatrix} \right] dx \quad\text{................(A.179)}$$

$$K_{3,l} = \int_e \left[\hat{F}_{3,l} + \alpha \begin{pmatrix} \hat{W}_{31}\hat{E}_{1,l} + \hat{W}_{32}\hat{E}_{2,l} + \hat{W}_{33}\hat{E}_{3,l} \\ +\hat{W}_{31,l}\hat{E}_1 + \hat{W}_{32,l}\hat{E}_2 + \hat{W}_{33,l}\hat{E}_3 \end{pmatrix} \right] dx \quad\text{................(A.180)}$$

$$K_{4,l} = \int_e \hat{F}_{4,l} dx \quad\text{......................................(A.181)}$$

$$K_{5,l} = \int_e \hat{F}_{5,l} dx \quad\text{......................................(A.182)}$$

$$K_{6,l} = \int_e \hat{F}_{6,l} dx \quad\text{......................................(A.183)}$$

$$K_{7,l} = \int_e \hat{F}_{7,l} dx \quad\text{......................................(A.184)}$$

$$K_{8,l} = \int_e \hat{F}_{8,l} dx \quad\text{......................................(A.185)}$$

for $l = 1,8$, the above equations give derivative with respect to each of the eight unknowns, where $S_{r,s}$ and $K_{r,s}$ (for $r,s = 1,8$), represent $N_e \times N_e$ matrices. The Jacobian for an element is given by

$$J_e = \left[S_{r,s} + \theta \Delta t K_{r,s}^{n+1} \right] \quad\text{......................................(A.186)}$$

The above Jacobian represents a 8×8 matrix, where each element of the matrix is itself a $N_e \times N_e$ matrix. The element Jacobian matrices and residual vectors are

118

assembled into a global re.:dual vector and matrix, the left out boundary terms in (A.37) to (A.39) are included and the system of equations is solved using Newton-Raphson iterative technique.

This appendix outlines briefly the development of CDG-1D and Buhnov-Galerkin finite element schemes as applied to the VAM equations. Hicks and Steffler (1990), documented in detail the development of both the CDG-1D and Buhnov-Galerkin schemes for solving the St. Venant equations. The above authors also performed in depth analysis for the stability, accuracy and convergence criteria of the above schemes.

The tests conducted in this study, although steady, are solved as unsteady problems. The following procedure is adopted for arriving at the final steady state solution:

1. Identify the initial and boundary conditions.

2. Select spatial and time discretizations. Usually the spatial discretization is an order of magnitude lower than the flow depth and the time discretization is such that the Courant number is less than six.

3. To advance the solution to next time level, the Newton-Raphson iterative technique is used to solve the resulting non-linear set of algebraic equations. The convergence criteria is assessed using (2.17) and a tolerance of 10^{-6}.

4. The convergence to the final steady state solution is also assessed by (2.17) with a tolerance of 10^{-6}. In this case the difference between the variable is taken at the two consecutive time levels.

5. During the solution the time step is geometrically increased as soon as the difference between the variables at two consecutive time levels falls below 10^{-2}.

References

Celia, M. A., and Gray, W. G. (1992). "Numerical Methods for Differential Equations." Prentice-Hall, Englewood Cliffs, New Jersey.

Hicks, F. E., and Steffler, P. M. (1990). "Finite Element Modeling of Open Channel Flow." Technical Report, WRE 90-6, University of Alberta.

Hicks, F. E., and Steffler, P. M. (1992). "Characteristic Dissipative Galerkin Scheme for Open-Channel Flow." J. Hydr. Engrg., ASCE, 118(2), 337-352.